Temperature Compensation and Performance Enhancement Techniques for Lamé Mode MEMS Resonators

By

Amir Reza KOLAHDOUZ MOGHADDAM

MANUSCRIPT-BASED THESIS PRESENTED TO ÉCOLE DE TECHNOLOGIE SUPÉRIEURE IN PARTIAL FULFILLMENT FOR A MASTER'S DEGREE WITH THESIS IN ELECTRICAL ENGINEERING M.A.Sc.

MONTREAL, 22, DECEMBER, 2022

ÉCOLE DE TECHNOLOGIE SUPÉRIEURE
UNIVERSITÉ DU QUÉBEC

BOARD OF EXAMINERS

THIS THESIS HAS BEEN EVALUATED

BY THE FOLLOWING BOARD OF EXAMINERS

M. Frédéric Nabki, Thesis supervisor
Department of Electrical Engineering, École de technologie supérieure

M. Michael Ménard, Chair, Board of Examiners
Department of Electrical Engineering, École de technologie supérieure

M. Ricardo Izquierdo, Member of the Jury
Department of Electrical Engineering, École de technologie supérieure

THIS THESIS WAS PRESENTED AND DEFENDED

IN THE PRESENCE OF A BOARD OF EXAMINERS AND THE PUBLIC

ON 7, DECEMBER, 2022

AT ÉCOLE DE TECHNOLOGIE SUPÉRIEURE

ACKNOWLEDGEMENTS

Compensation de la température et amélioration des performances des résonateurs MEMS de type Lamé

Amir Reza KOLAHDOUZ MOGHADDAM

RÉSUMÉ

L'importance des résonateurs micro-usinés ne cesse de croître à mesure qu'ils s'imposent dans un large éventail d'applications, des dispositifs portables aux applications plus complexes telles que les communications sans fil et les applications aérospatiales. En raison de cette demande accrue, les universitaires et l'industrie développent des oscillateurs plus performants et plus stables tout en se concentrant sur la réduction des coûts.

Bien que de nombreuses architectures de résonateurs et de circuits électriques pour piloter les résonateurs ont été étudiés depuis de nombreuses années, le problème de la production d'un résonateur entièrement compensé qui fonctionne indépendamment de la température ambiante reste non résolu.

Ce travail présente un modèle analytique pour prédire la performance de résonateurs de type Lamé avec différents degrés de rotation, et géométries. L'adaptabilité du modèle analytique proposé a été démontrée, et la polyvalence du modèle a été validée expérimentalement en fabriquant plusieurs variantes de résonateurs et en analysant leurs réponses en fréquence et leur comportement en température.

Ensuite, un nouveau résonateur électrostatique en mode Lamé utilisant un actuateur thermique en forme de chevron est proposé, celui-ci permet de diminuer les pertes d'insertion réduisant ainsi la résistance parasitaire et surmontant une des limitation du processus de micro-fabrication. Il est démontré que la combinaison des éléments chauffants et du résonateur dans une petite zone peut permettre une stabilité de la fréquence en fonction de la température.

Mots-clés: Résonateurs MEMS, micro-usinage en masse, caractérisation du comportement résonant, coefficient de température de fréquence, résonateur compensé en température, fermeture d'entrefer, électrode mobile, résistance motionnelle

Temperature Compensation and Performance Enhancement Techniques for Lamé Mode MEMS Resonators

Amir Reza KOLAHDOUZ MOGHADDAM

ABSTRACT

The importance of micromachined resonators continues to grow as they become increasingly prevalent in a wide range of applications, from wearable devices to more complex applications such as wireless communication and aerospace. As a result of this increased demand, academics and industry are developing oscillators with higher performance and stability while focusing on cost reduction.

Although numerous resonator architectures and electrical circuits to drive the resonator have been studied for many years, the problem of producing a fully compensated resonator that operates independently of ambient temperature remains unsolved.

This work presents an analytical model for predicting the performance of a Lamé resonator with varying rotation angles, and different structure varieties are proposed. The adaptability of the proposed analytical model is demonstrated, and the model's versatility is experimentally validated by fabricating multiple resonator variants and analyzing their frequency responses and temperature behavior.

Afterward, a novel Lamé mode electrostatic resonator employing a chevron-shaped thermal actuator is proposed, which decreases the transducer gap resulting in a reduced motional resistance and overcoming the micro-fabrication process limitation in the minimum spacing of the structural silicon layer. It is shown that combining the heaters and the resonator in a small area may result in frequency stability over temperature by applying the ovenization concept utilized in oscillators.

Keywords: MEMS resonators, Bulk micromachining, Resonant behavior characterization, Temperature coefficient of frequency, Temperature-compensated resonator, Gap closing, Movable electrode, Motional resistance

TABLE OF CONTENTS

LIST OF TABLES

LIST OF FIGURES

Page

LIST OF ABBREVIATIONS

AlGaN   Aluminium Gallium Nitride

AlN   Aluminum Nitride

BAW   Bulk Acoustic Wave resonator

BVD   Butterworth-Van Dyke

CMOS   Complementary Metal Oxide Semiconductor

ETS   École de Technologie Supérieure

FEM   Finite Element Modelling

GSG   Ground-Signal-Ground

GaN   Gallium Nitride

HEMT   High Electron Mobility Transistors

HF   Hydrofluoric

IC   Integrated Circuit

IoT   Internet of things

LaCIME   (french, Laboratoire de Communications et d'Intégration de la MicroÉlectronique)

MEMS   Microelectromechanical Systems

OCXO   Oven Controlled Crystal Oscillators

PCB   Printed Circuit Board

PID   Proportional–Integral–Derivative

PLL   Phase-locked Loop

PPM	Parts per Million
Q-Factor	Quality Factor
SEM	Scanning Electron Microscope
SOI	Silicon On Insulator
SiBAR	Silicon Bulk Acoustic Resonators
SiLOx	Silicon Oxide
SiO^2	Silicon Dioxide
TCF	Temperature Coefficient of Frequency
TCXO	Temperature Compensated Crystal Oscillator
TIA	Transimpedance Amplifier
VCO	Voltage Controlled Oscillator
VNA	Vector Network Analyzer

LIST OF SYMBOLS AND UNITS OF MEASUREMENTS

α	Thermal expansion coefficient
β	Filling factor
ε	Strain
ν	Poisson's ratio
ρ	Material density
σ	Stress
Ω	Ohm
ω	Resonant frequency (radians per second)
$°C$	Celsius
c	Stiffness
c_{eq}	Equivalent stiffness
E	Young's modulus
f	Frequency
f_0	Resonant Frequency (Hz)
F	Farad
g	Gram
h	Height
H	Henry
Hz	Hertz

k	Fitting factor
kc	Spring constant
L	Length
L_{eff}	Effective Length
m	Mass
Pa	Pascal
Q	Quality Factor
R	Resistivity
T	Temperature
V	Voltage
W	Watt

INTRODUCTION

Motivation

Micro-Electro-Mechanical Systems (MEMS) is a revolutionary technology for combining electrical and mechanical principles on a micro-scale. Mechanical structures have been used since the dawn of time, and building them on a single substrate with electrical components allows for the integration of many sensors and actuators' applications such as resonators, gas detectors, gyroscopes, accelerometers, ultrasound devices, and many other applications. MEMS manufacturing enables us to use the same substrate for electrical components such as transistors, significantly reducing cost and space, as shown in figure 0.1.
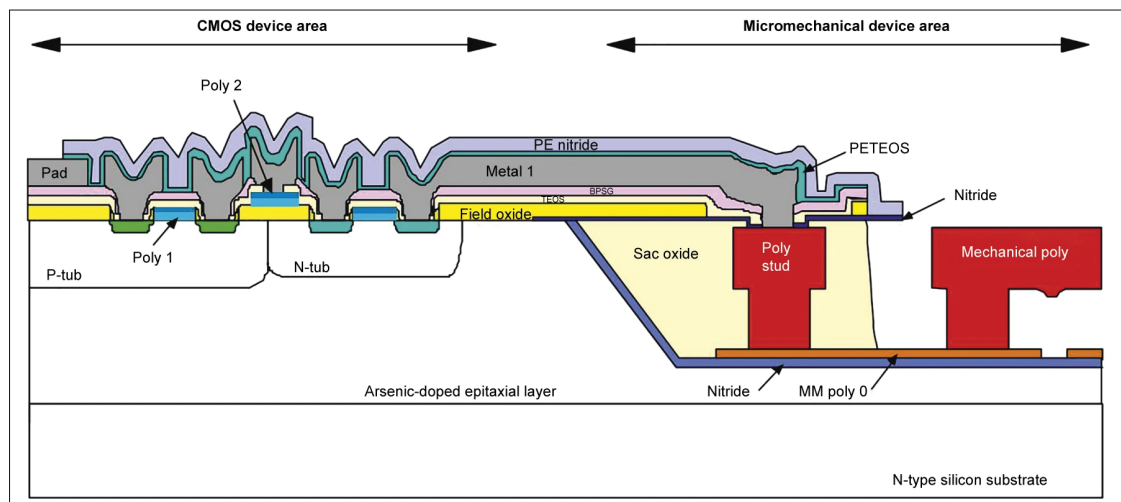
Figure 0.1   [A cross-sectional schematic of a substrate with CMOS and MEMS integrated technology
Taken from Smith *et al.* (1995)

Resonators are critical components in the development of reference oscillators, which has drawn scholarly interest, and now this interest has gone widespread in the electronics industry and represents a multi-billion-dollar market. Figure 0.2 shows the number of publications in the Scopus database from 1992 to 2022. In 2008, the total MEMS market was valued at about $4

billion (Lam (2008)). In 2018, just the MEMS oscillator market was valued at $3.4 billion, and it is expected to reach $6.5 billion by 2025 (TheExpressWire (2022)). SiTime, one of the earliest companies in MEMS-based oscillators, announced $70.3 million in net revenue in the first quarter of 2022, a 97.7% increase over the same period last year (Chadwick, Sievers & Perry (2022)).
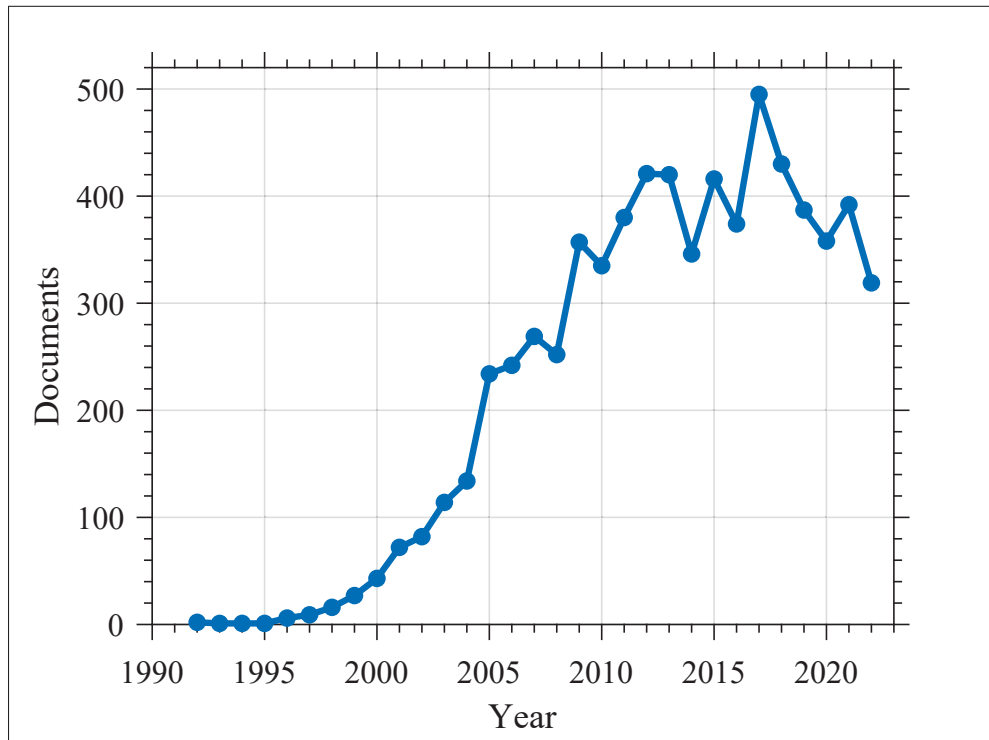
Figure 0.2   Quantity of publications in the field of MEMS resonator
presented in the Scopus database
Inspired from Sco

The market is rapidly increasing due to driving motivations like the Internet of Things (IoT), high-frequency wireless communication, and wearable devices. The modern need for accurate timing and high-performance oscillators, such as high-quality factor (Q), high-frequency stability, low power consumption, and small footprint, are making MEMS oscillators an important solution in the market.

Background

Since the dawn of time, humankind has placed a high value on timekeeping. Its significance as a crucial part of human life developed as the requirement for cooperation among members of expanding communities grew. Timing dates back to the ancient world when a sundial used a gnomon to cast a shadow on a set of hourly markings (Marrison (1948)). With the advancement of human civilization, precise timing has become increasingly vital. The acoustic resonator shaped as a tuning fork represents the early stages of modern timing resonators.

The development of crystallography led to the development of quartz crystals, which provided a new method for accurately measuring time. In 1921, Walter Guyton Cady constructed the first quartz crystal oscillator (Nicolson (1940)). Quartz crystal oscillators were developed for high-stability frequency references in applications such as broadcast stations, time-keeping applications, digital integrated circuits, etc. Quartz is piezoelectric, simplifying stimulation and decreasing frequency variation due to a single crystal structure. Furthermore, the Quartz resonant frequency is quite stable with temperature, making them a prominent component in oscillator manufacturing. The key benefits of Quartz crystal oscillators are their quality factor, frequency stability, and phase noise performance. However, the large size and difficulties of integrating with well-developed manufacturing techniques have sparked interest in developing a suitable alternative.

Over the past two decades, MEMS resonators have proven to be an excellent contender to replace traditional quartz resonators in timing applications. The MEMS resonators are smaller than crystal-based resonators and may be manufactured with a silicon substrate using photolithography. Utilizing a silicon substrate permits the manufacturer to combine the MEMS device and electrical circuit onto the same wafer or within a highly compact package.

The MEMS resonators concept was published based on the tuning fork filter by O'connor (1960) in 1960. The incorporation of a high-quality beam resonator into silicon integrated circuits was proposed by Nathanson, Newell, Wickstrom & Davis (1967) in 1967; nonetheless, microfabrication technology has always been a vital factor in MEMS development. As Petersen (1997) eloquently explains, the evolution of the fabrication technique facilitated MEMS construction on silicon in 1984. Due to the rapid pace of manufacturing advancement, the MEMS resonator became a formidable competitor for quartz crystals, and its quality factor surpassed that of the best quartz-based oscillators on the market.

The MEMS resonator vision went beyond academia, and Discera was one of the first firms in 2001 to develop the concept of timing and clock oscillators using a proprietary MEMS. The commercialization of silicon resonators drew more attention in the years that followed when a research group at Stanford University founded a startup company, SiTime, in 2004. SiTime released their Elite platform of Super-TCXOs (temperature-compensated crystal oscillators) in 2016, and they now have a significant market share in 5G communication and aerospace timing applications (Electronic Products (2017)). Surprisingly, SiTime remains the dominant company having pioneered MEMS-based oscillators and worthy competitors have had difficulty surpassing their technological advances.

Today, the market has recognized MEMS resonators as an acceptable replacement for Quartz crystals. Abracon, Microchip, and Ecliptek are only a few examples of competitors in the oscillator industry whose previous technologies have been replaced by MEMS-based oscillators. The electronic market anticipates that the performance and cost of oscillators in this class will continue to improve.

Research Problem

In the past two decades, MEMS oscillators have gained interest due to their high-quality factor, small aspect ratio, and integration with CMOS circuits. These advantages make the MEMS resonator prominent over traditional quartz crystals; however, the temperature variation can affect the resonator performance in high-accuracy applications like 5G communication and satellites. Therefore, to adapt the MEMS resonators to today's application, frequency stability over the temperature must be enhanced.

Today's commercial silicon MEMS resonators rely on active temperature compensation: temperature is sensed extremely accurately adjacent to the resonator, and frequency error is adjusted in the frequency synthesis block using phase-locked-loop (PLL) techniques (Lee, Partridge & Assaderaghi (2012)). However, this method increases cost and power consumption while deteriorating the oscillator's noise performance.

The passive temperature compensation method has the benefit of requiring no energy at the expense of a Quality factor (Q) reduction. This quality factor degradation can be tolerated in a very high-Q resonator such as a Lamé resonator. The MEMS manufacture and process adjustments are expensive; therefore, the iterations required to attain an acceptable resonator can be prohibitively expensive. The missing element is a reliable model that can forecast the resonator's behavior following various passive temperature compensation strategies to shorten the process exploration period and time to market.

In addition to improving the temperature stability, the resonator's performance must be strengthened. The micro-fabrication process limitation on the minimum spacing of the structural silicon layer (i.e., 2 μm) can substantially affect the resonator transducer. This electrostatic gap must be shrunk to lower the motional resistance and reduce resonator insertion loss.

Research Objectives

The primary objective of this thesis is to study potential methods for reducing the silicon resonator's temperature dependency and manufacturing the resonators using commercial fabrication techniques. In addition, the silicon resonator is modeled analytically, and the temperature coefficient of frequency (TCF) of bulk micromachined silicon Lamé resonators are extensively investigated.

The particular objectives are:

- Develop a general model for bulk micromachined silicon Lamé resonators representing the resonant frequency and the temperature coefficient of frequency (TCF) in different temperature variation treatment techniques;
- Design and fabricate the proposed resonators variants to empirically validate the modeling and compare the measurement results with the model output;
- Extensively test and measure the proposed MEMS resonator and provide potential solutions to enhance the measurement results and reduce undesired side effects; and
- Increase the resonator transduction by reducing the electrostatic resonator gap and create a Lamé resonator that can be temperature compensated.

These findings offer recommendations for MEMS Lamé resonators with enhanced temperature stability and modeling insight into the various temperature compensation methods. Moreover, the provided model enables the prediction of the resonant frequency and TCF behavior utilising various compensating approaches.

Contributions

The main contribution of this work is the analytical modeling and investigation of possible passive and active techniques to reduce Lamé resonators' temperature sensitivity and enhance

resonator performance. These resonators and compensation techniques are implemented in PiezoMUMPs fabrication technology. The contributions of this thesis to overcoming the issues mentioned above can be classified as follows:

1. **Developing an analytical model to predict the resonant frequency and the TCF:**

   This work has developed an analytical model to predict the resonant frequency and TCF for various passive compensating techniques. This model was created for the Lamé resonator, although the theory can be applied to any in-plane resonator.

2. **Manufacturing sixteen device variants in PiezoMUMPs technology to empirically validate the proposed model:**

   These proposed Lamé resonators are manufactured in four design categories and orientations, totaling sixteen device versions. It is also demonstrated that the devices' resonant frequency and frequency-temperature dependence can be predicted using an analytical model derived from the measurements once elastic parameters have been collected.

3. **Reduce the electrostatic gap in the Lamé resonator by utilizing chevron-shaped thermal actuators:**

   The proposed Lamé mode electrostatic resonator employs a novel thermal transducer gap reduction method to minimize the motional resistance and circumvent the micro-fabrication process limitation regarding the minimum spacing of the structural silicon layer.

4. **Leveraging chevron-shaped thermal actuators to act as a micro-oven:**

The heater is intended to raise the temperature above the chevron and, as a result, reduce the electrostatic gap caused by thermal expansion. In addition, this power can be used to increase the resonator's temperature regardless of the ambient temperature and this can thus enable a self-heated structure that can be made resilient to ambiant temperature variations.

Thesis Outline

This is a manuscript-based thesis. Thus, chapters 2 and 3 each provide a journal article. The structure of the thesis is as follows:

Chapter 1 reviews the literature on silicon as a material in MEMS manufacturing and its temperature dependence. The advantages and drawbacks of passive and active techniques for decreasing the temperature dependence of silicon-based resonators are discussed.

Chapter 2 investigates the temperature dependence modeling and thermal sensitivity reduction of bulk micromachined silicon MEMS Lamé resonators. An overview of the state of the art of temperature dependency reduction of MEMS resonators is presented, as well as the frequency behavior of MEMS Lamé resonators and the analytical modeling of the resonator's temperature-sensitive features. The experimental results show the characterization of the proposed Lamé resonators' performance. This includes the characterization of the devices under temperature variations. Moreover, the elastic coefficients for the proposed analytic model were measured experimentally and used to validate the proposed model.

Chapter 3 presents a capacitive bulk mode resonator functioning in Lamé mode, in which the motional resistance and temperature stability are improved by using a chevron-shaped thermal

actuator to decrease its transducer gaps. The integrated thermal actuators can act as heaters, raising the temperature of the suspended square structure to provide a path to compensate for variations in ambient temperature.

The summary and conclusion of this thesis are provided in the last chapter, along with suggestions for further study and improvements.

An appendix is provided at the end of the thesis that details the method to calibrate the thermal camera used to report the temperature results in this work.

CHAPTER 1

LITERATURE REVIEW

This chapter will investigate the most prevalent techniques for temperature compensation of bulk mode resonators and compare their benefits and limitations. Additionally, the PiezoMUMPS manufacturing process will be discussed in detail. This review focuses primarily on the bulk mode Lamé resonator with electrostatic actuation.

1.1   Lamé Mode Resonator

The MEMS resonator that is the focus of this thesis is made of a suspended micro-scale square plate intended to be excited to vibrate within a particular lateral antisymmetric mode within the manufacturing plane: the Lamé mode. This mode is characterized by the opposing two sides of the square expanding, while the opposite sides on the other two orthogonal sides shrink. Figure 1.1 shows the Lamé mode for a square plate.
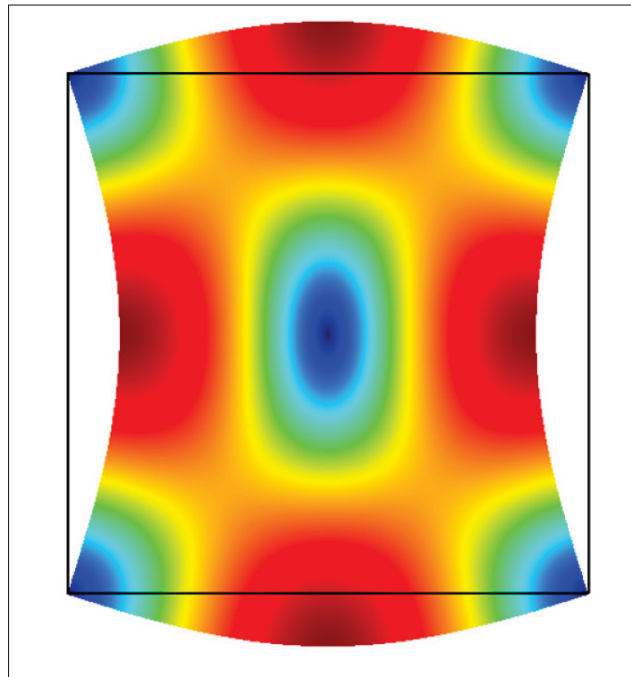
Figure 1.1   Lamé mode shape of a square plate resonator
Taken from Abdolvand *et al.* (2016)

1.2   Silicon as a Resonator Material

Single-crystalline silicon is a crucial material in the microelectronics industry. Silicon's outstanding mechanical qualities, including low loss and excellent mechanical/chemical stability, make it an appealing material option. It is anticipated that silicon-based resonators will become ubiquitous in a variety of applications due to their suitability for low-cost batch production using methods similar to those employed in complementary metal oxide semiconductor (CMOS) technologies. The silicon elastic properties employed in a lumped element model determine the resonator's behavior. The elasticity of single-crystal silicon is anisotropic, which means that the behavior of the crystal depends on its orientation. The silicon elastic matrix can be presented as a fourth-order tensor given by:

$$
C = \begin{bmatrix}
c_{11} & c_{12} & c_{12} & 0 & 0 & 0 \\
c_{12} & c_{11} & c_{12} & 0 & 0 & 0 \\
c_{12} & c_{12} & c_{11} & 0 & 0 & 0 \\
0 & 0 & 0 & c_{44} & 0 & 0 \\
0 & 0 & 0 & 0 & c_{44} & 0 \\
0 & 0 & 0 & 0 & 0 & c_{44}
\end{bmatrix},
\tag{1.1}
$$

where c_{11}, c_{12}, and c_{44} are three independent elastic constants in the cubic crystal system, which can be determined from a set of data collected from measured resonant frequencies.

The resonant frequency for a square Lamé resonator can be evaluated as follows:

$$
f = \frac{1}{2\pi}\sqrt{\frac{k_c}{m}} = \frac{1}{L_{eff}}\sqrt{\frac{c_{eq}}{\rho}} = \sqrt{\frac{h\, c_{eq}}{2m}},
\tag{1.2}
$$

where k_c, m, L_{eff}, c_{eq}, ρ and m are the spring constant, resonator mass, characteristic resonator length (i.e., $\sqrt{2}L$), equivalent material stiffness, material density and mass, respectively.

1.3   Silicon Behavior in Temperature Variation

A resonator's frequency should be as immune to temperature fluctuations as feasible. However, silicon, the preferred material for MEMS resonator manufacturing, is sensitive to temperature. The MEMS resonators experience ± 50 ppm/°C frequency variation, while the traditional quartz crystal in AT-cut keeps this variation in a ± 10 ppm/°C range. This unwanted effect must be reduced so that systems requiring very accurate frequency responses, such as timing oscillators and electromechanical filters, can function. In commercial products, compensation is typically accomplished through active circuit-level compensation techniques and passive compensation based on heavy doping and the addition of a layer to the resonator structure with an opposite stiffness variation with temperature.

The frequency shift caused by temperature variations can be calculated using equation 1.2 and a first derivative with regard to temperature:

$$\frac{\partial f}{\partial T} = \frac{1}{\sqrt{2m}} \left(\frac{\partial \sqrt{h\, c_{eq}}}{\partial T} \right) = \frac{1}{\sqrt{8mh\, c_{eq}}} \left(c_{eq} \frac{\partial h}{\partial T} + h \frac{\partial c_{eq}}{\partial T} \right), \tag{1.3}$$

where T is the absolute temperature. The temperature coefficient of frequency (TCF) is the rate of shift of frequency versus temperature from a resonator center frequency. Therefore, by dividing equation 1.3 by the reference frequency, the TCF result in:

$$\begin{aligned}
TCF &= \frac{1}{f_0} \frac{\partial f}{\partial T} = \frac{1}{f_0 \sqrt{8mh\, c_{eq}}} \left(c_{eq} \frac{\partial h}{\partial T} + h \frac{\partial c_{eq}}{\partial T} \right) \\
&= \sqrt{\frac{2m}{8mh^2\, c_{eq}^2}} \left(c_{eq} \frac{\partial h}{\partial T} + h \frac{\partial c_{eq}}{\partial T} \right) \\
&= \frac{1}{2hc_{eq}} \left(c_{eq} \frac{\partial h}{\partial T} + h \frac{\partial c_{eq}}{\partial T} \right) \\
&= \frac{\alpha}{2} + \frac{1}{2c_{eq}} \frac{\partial c_{eq}}{\partial T} \\
&= \frac{\alpha}{2} + \frac{1}{2} TC_{c_{eq}},
\end{aligned} \tag{1.4}$$

where α is the thermal expansion coefficient, $TC_{c_{eq}}$ is the temperature coefficient of equivalent stiffness, and f_0 is the resonant frequency at the reference temperature. Also, the resonant frequency can be written as a polynomial regarding the temperature coefficient of frequency for each order:

$$f(T) = f_0 \left[1 + TCF_1 \times \Delta T + TCF_2 \times \Delta T^2 \right], \tag{1.5}$$

where the ΔT is the temperature difference between the final resonator temperature and the reference temperature, TCF_1 and TCF_2 are the first and second order temperature coefficients.

Figure 1.2 illustrates the TCF in different mode shapes and orientations. The Lamé resonator has the highest TCF_1 (at a maximum of +22 ppm/°C); hence, the resonator must be temperature compensated.
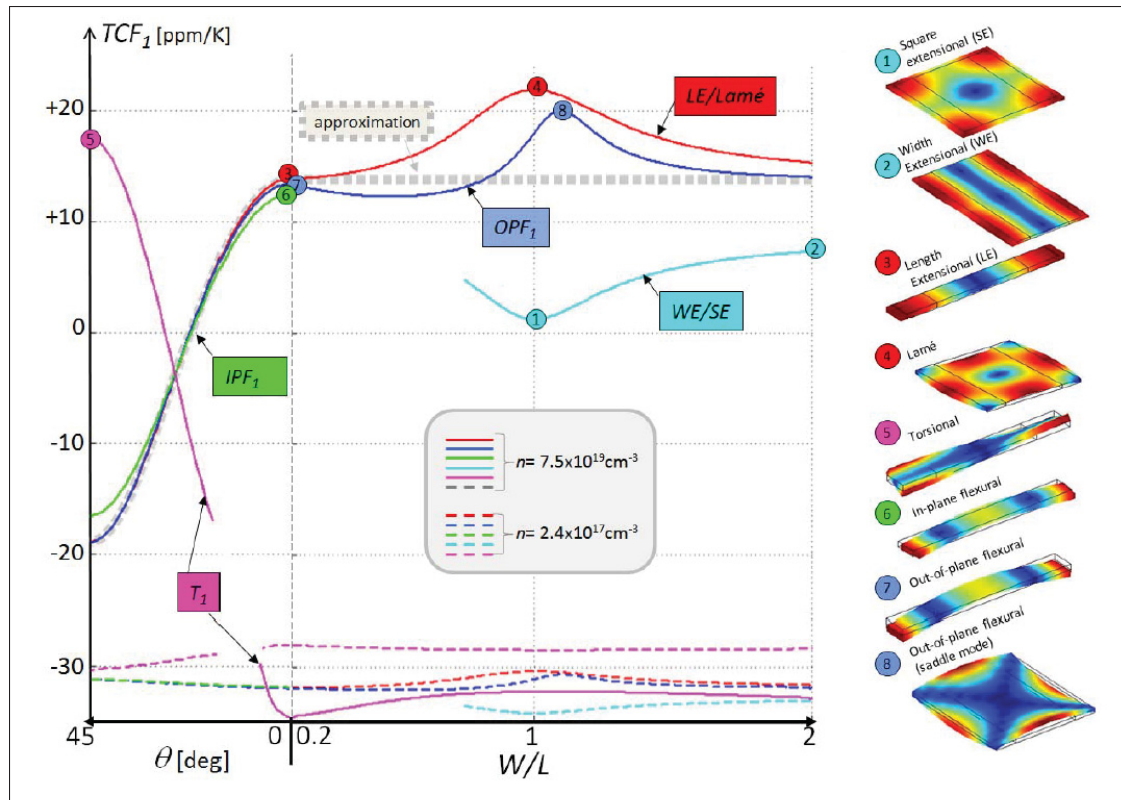
Figure 1.2   The temperature coefficient of frequency in different resonant mode shapes. The doping level of silicon is shown in two levels, and the resonators' orientation is varied from 0 to 45 degrees
Taken from Jaakkola *et al.* (2015)

Generally, to achieve a temperature-compensated resonator, several approaches have been proposed, which can be categorized into passive and active types:

1.3.1   Passive Temperature Compensation

The passive methods (i.e., material or mechanical compensation) include modification in silicon doping, heavy doping the silicon, altering the silicon crystal orientation, addition of layer with opposite TCF polarity, and structure modification like adding an array of holes over the resonator structure or adding pillars in the structure. These approaches do not consume power and may be included in the manufacturing process; nevertheless, the side effect is a quality factor degradation

and no control over the resonant frequency with an active feedback loop. It will be explained in detail how these approaches function to lessen TCF:

1.3.1.1　Silicon Doping

Silicon doping is often used to decrease the influence of temperature on the resonant frequency. Temperature compensation of silicon resonators on a silicon substrate began with p-type doping, but n-type doping soon became a viable option. Silicon is considered an anisotropic material whose elastic behavior is heavily connected to the structural crystal orientation; hence, determining the correct value of Young's modulus (E) for a silicon crystal may be challenging. The Young's modulus of silicon may vary from 130 to 188 Gpa depending on the structure's orientation, and Poisson's ratio can range from 0.048 to 0.40.

The crystal orientation of the silicon in the wafer influences the crystalline properties of the wafer [13]. The wafer orientation is matched with the layout editor's XY coordinate system in a computer-based MEMS manufacturing process. This implies that the structure is aligned to the XY axes on a (100) silicon wafer in a conventional MEMS manufacturer.

Single crystal silicon is a linear material; hence, the relationship between stress and strain of the material inside a continuous elastic material is analogous to Hooke's Law for small strains ($\left| \frac{T - T_0}{T} \right| \ll 1$) Sähn (1972):

$$\sigma_{ij} = C_{ijkl} \left[\varepsilon_{kl} - \alpha_{kl} \left(T - T_0 \right) \right], \qquad i, j, k, l = 1, 2, 3 \tag{1.6}$$

where σ_{ij} is the second-ranked stress tensor, C_{ijkl} is the fourth-ranked tensor stiffness (elasticity tensor), ε_{kl} is the second-ranked strain tensor, α_{kl} is the thermal expansion coefficient, T is the absolute temperature, and T_0 is the ambient temperature when the structure is not deformed, respectively. Cubic symmetry and shear equivalence would produce a tensor of the fourth rank with just three independent components. The tensor matrix can then be expressed as the following 6 × 6 matrices:

$$
\begin{bmatrix} \sigma_1 \\ \sigma_2 \\ \sigma_3 \\ \sigma_4 \\ \sigma_5 \\ \sigma_6 \end{bmatrix} = \begin{bmatrix} c_{11} & c_{12} & c_{12} & 0 & 0 & 0 \\ c_{12} & c_{11} & c_{12} & 0 & 0 & 0 \\ c_{12} & c_{12} & c_{11} & 0 & 0 & 0 \\ 0 & 0 & 0 & c_{44} & 0 & 0 \\ 0 & 0 & 0 & 0 & c_{44} & 0 \\ 0 & 0 & 0 & 0 & 0 & c_{44} \end{bmatrix} \begin{bmatrix} \epsilon_1 \\ \epsilon_2 \\ \epsilon_3 \\ \epsilon_4 \\ \epsilon_5 \\ \epsilon_6 \end{bmatrix}, \tag{1.7}
$$

$$
\begin{bmatrix} \epsilon_1 \\ \epsilon_2 \\ \epsilon_3 \\ \epsilon_4 \\ \epsilon_5 \\ \epsilon_6 \end{bmatrix} = \begin{bmatrix} s_{11} & s_{12} & s_{12} & 0 & 0 & 0 \\ s_{12} & S_{11} & s_{12} & 0 & 0 & 0 \\ s_{12} & s_{12} & s_{11} & 0 & 0 & 0 \\ 0 & 0 & 0 & s_{44} & 0 & 0 \\ 0 & 0 & 0 & 0 & s_{44} & 0 \\ 0 & 0 & 0 & 0 & 0 & s_{44} \end{bmatrix} \begin{bmatrix} \sigma_1 \\ \sigma_2 \\ \sigma_3 \\ \sigma_4 \\ \sigma_5 \\ \sigma_6 \end{bmatrix} \tag{1.8}
$$

where s_{11}, s_{12} and s_{44} represents the corresponding values in the compliance tensor. The relationship between stress and strain for any arbitrary direction may be computed by aligning the matrix axes with the direction of the studied structure. It can be seen that with measurements of acoustic wave propagation in the solid, it is possible to determine the constant elastic properties. This approach requires straightforward sample preparation. In addition, it is essential to note that this approach offers a high degree of precision since it measures a travel time interval. This measuring technique is explained in detail in [10] and its citations.

18
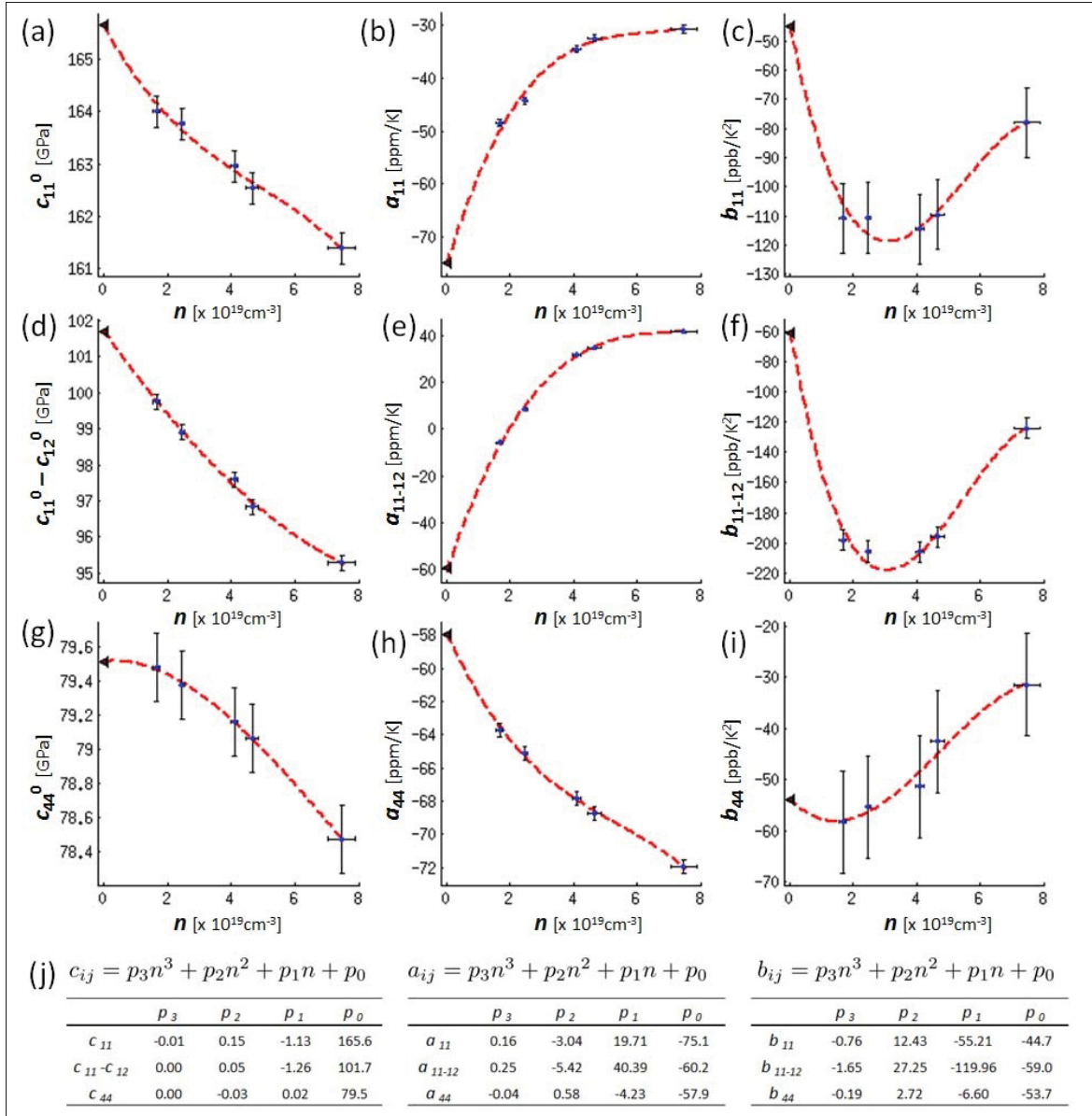
Figure 1.3   Polynomial approximations of the coefficients a_{ij}, b_{ij} and c_{ij}
Taken from Jaakkola *et al.* (2015)

During the transmission of an acoustic wave through a solid material, the periodicity of the atomic lattice is frequently perturbed by alternating compressional and dilational stresses (Samarao & Ayazi (2012)). Such a disruption of atomic periodicity immediately affects the electronic band structure of a semiconductor like silicon. According to the principle of energy conservation, such a temperature-dependent rise in electronic energy emerges as a commensurate

fall in the system's elastic energy. As a result, with rising temperature, a gradual decrease in Young's modulus (E) of the resonant silicon microstructure and, consequently, its resonant frequency is observed. Jaakkola *et al.* (2015) has studied the temperature dependence of the elastic constants at various doping levels. As demonstrated in figure 1.3, the second-order temperature coefficient b_{11-12} accounts for the majority of the contribution to the remaining (non-zero) second-order coefficient TCF_2, with a decreasing value found for $n > 4 \times 10^{19} cm^{-3}$. All other temperature constants, including those in figure 1.3 a_{ij}^0, b_{ij}^0, and c_{ij}^0, are assumed to stay constant with respect to their values at $n_{max} = 7.5 \times 10^{19}\ cm^{-3}$. Under these presumptions, computations for the LE/Lamé mode were carried out (Jaakkola *et al.* (2015)), this time expanding the doping level to $n = 13 \times 10^{19}\ cm^{-3}$ and the results are presented in figure 1.4.

Doping the silicon seems to be a straightforward approach for minimizing the temperature's effect on the resonator's oscillation frequency by a considerable amount. This strategy is intended to lessen the effect of the resonator's stiffness coefficients. These coefficients, represented by equations 1.7 and 1.8), are dependent on doping and account for the fluctuation in the temperature coefficient of the Young's modulus. In addition, according to Samarao & Ayazi (2012), heavy doping damages the silicon crystal, lowering the quality factor. The type of doping has a significant impact on resonator temperature compensation. It is worth noting that N-type degenerate doping may attain positive TCF, but P-type degenerate doping seems to be restricted to a -1.5 ppm/°C TCF decrease (Hajjam, Rahafrooz & Pourkamali (2010)).

20
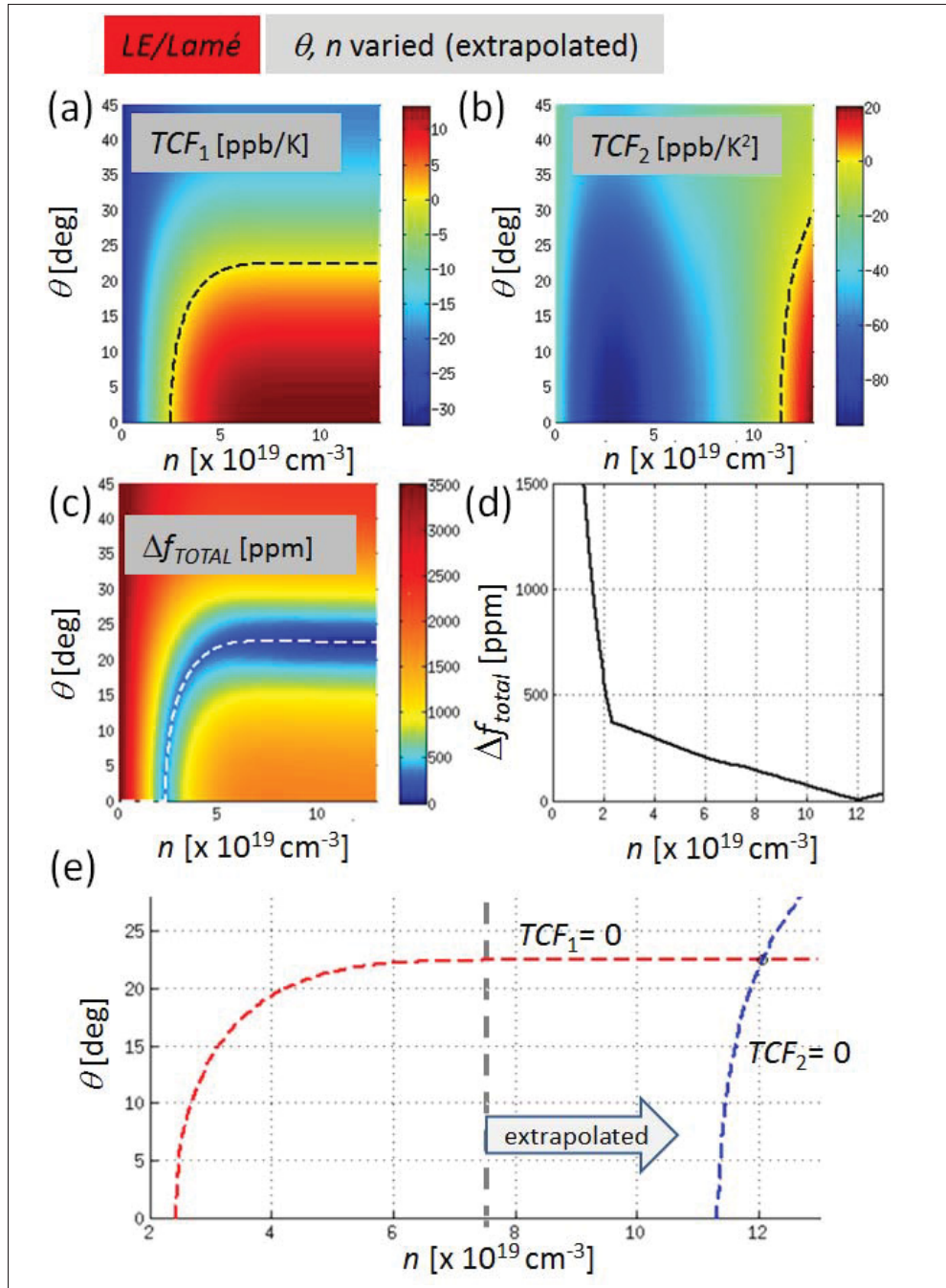
Figure 1.4   Temperature behavior extrapolated for the LE/Lamé when
orientation and doping n are varied
Taken from Jaakkola *et al.* (2015)

1.3.1.2   Silicon Orientation

Before we can characterize the influence of silicon orientation on resonant frequency and resonator temperature behavior, we must determine the crystal planes and axes. Miller indices define Crystallographic planes and orientations, and three XYZ integers represent system coordination (figure 1.5). A bar depicts the negative direction.
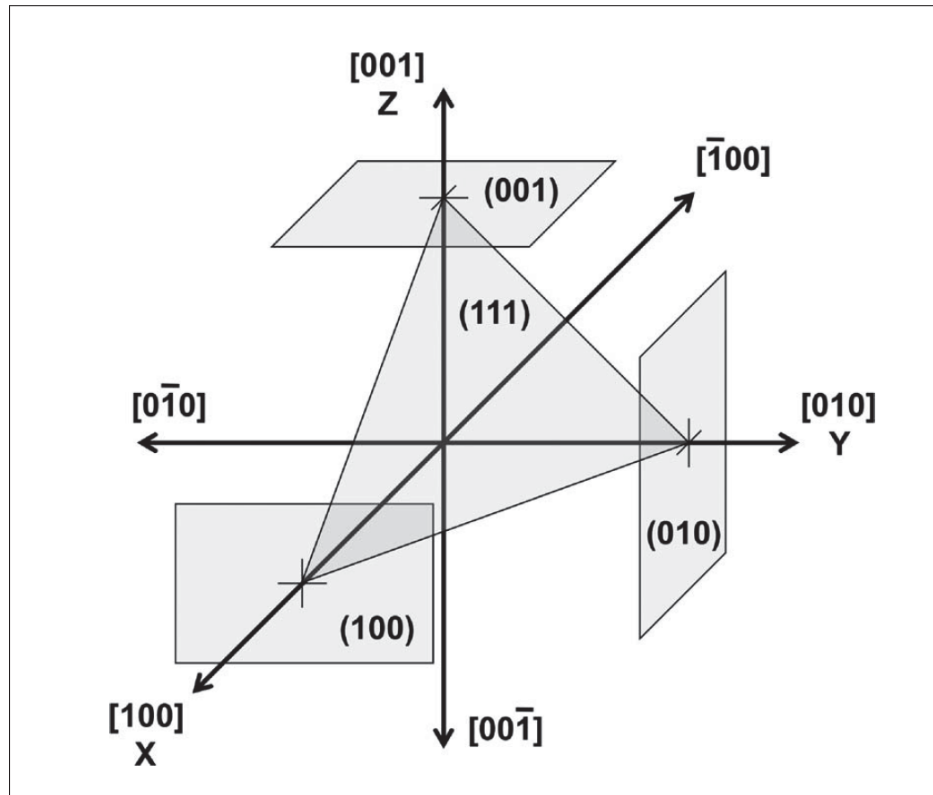
Figure 1.5   Miller guides lines in a cubic crystal. Silicon's
principal planes along the XYZ axis are described. Conventionally,
the directions [100], [010], and [001] are the XYZ Cartesian axes
Taken from Hopcroft (2010)

Quantum theory may be used to compute the elasticity values of a crystal since the elastic modulus represents the strain derivative of the crystal's free energy (Hall (1967); Keyes (2010)). Nonetheless, Hopcroft (2010) states that the computation is complex and incorporates several derived constants and approximations, so these conclusions should be regarded as a reliable

suggestion rather than a law. As mentioned in section 1.3.1.1, the optimum technique for measuring the elastic constants is to use acoustic wave propagation measurement in the solid, which involves relatively simple sample preparation and can be carried out with high precision due to the measurement of a time interval. The elastic constants values are given in table 1.1 which is extracted from Hall (1967).

Table 1.1   Elastic constants of Silicon at 298K
Taken from Hall (1967)

Material	c_{11} (GPa)	c_{12} (GPa)	c_{44} (GPa)	s_{11} (pPa)	s_{12} pPa)	s_{44} (pPa)
silicon	165.6	63.9	79.5	7.68	-2.14	12.6

In arbitrary directions, the values for Young's modulus and Poisson's ratio can be obtained by using the 0-degree rotation presented in table 1.1 concerning the crystal lattice. Figure 1.6 depicts the Young's modulus and Poisson's ratio variation as a function of silicon orientation in the (100) plane.
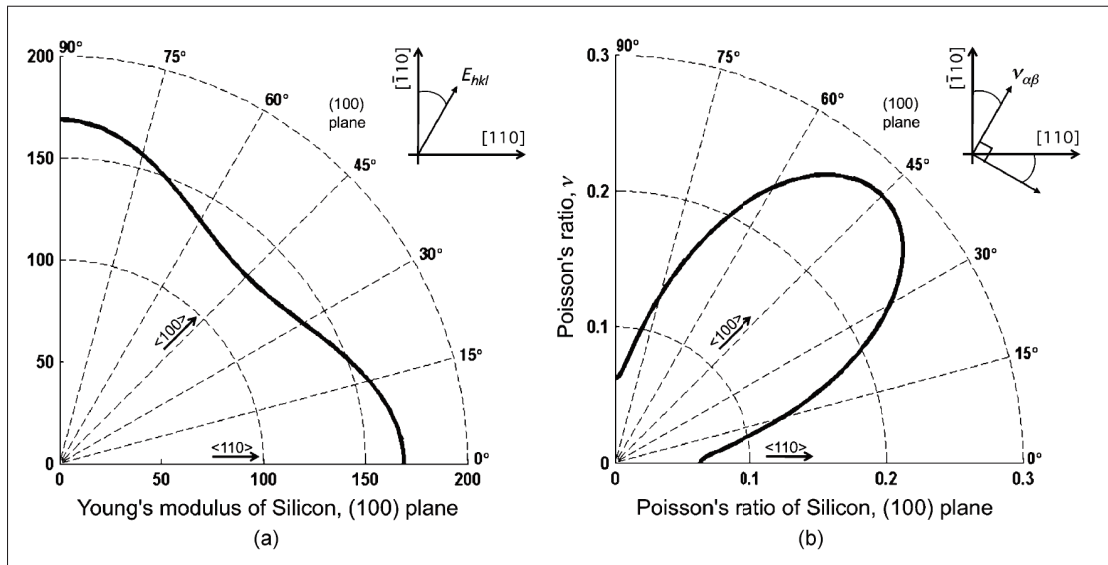
Figure 1.6   The circular plot of Young's modulus and Poisson's ratio versus orientation in silicon
Taken from Hopcroft (2010)

The silicon orientation significantly affects the resonant frequency since the elastic constants are orientation dependant. Jaakkola, Prunnila, Pensala, Dekker & Pekko (2014b) investigates the frequency drift and elastic constants as the silicon orientation changes. In a Lamé resonator with [100], only c_{44} contributes to the resonant frequency, however when [110] is considered, the resonant frequency is proportional to (c_{11}-c_{12}). The resonant frequency and frequency drift as a function of resonator orientation are shown in figure 1.7.

Figure 1.2 demonstrates that the Lamé resonator has the largest TCF compared to other mode shapes. Therefore, treatment is essential to lessen the temperature dependence of a resonator with this mode shape. In addition, the resonant frequency is excessively orientation-dependent; the TCF may shift from about +13 to -18 when the resonator is rotated between 0 to 45 degrees. This results in the possibility of locating the proper rotation to achieve zero TCF resonator. Notably, these findings pertain to a specific fabrication technique, including the doping level; hence, a complete examination is required for all other fabrication procedures.

		$f(c_{11}, c_{12}, c_{44})$	$\frac{1}{f}\frac{\partial f}{\partial c_{11}}$	$\frac{1}{f}\frac{\partial f}{\partial c_{12}}$	$\frac{1}{f}\frac{\partial f}{\partial c_{44}}$
				[ppm / MPa]	
Lamé 0°		$\frac{1}{\sqrt{2}L}\sqrt{\frac{c_{44}}{\rho}}$	0	0	6.33
LE 0°		-	1.77	-0.80	3.33
LE 11.25°		-	2.30	-1.37	2.72
LE 22.5°		-	3.37	-2.53	1.46
LE 33.75°		-	4.27	-3.50	0.40
LE 45°		-	4.61	-3.87	0
Lamé 45°		$\frac{1}{\sqrt{2}L}\sqrt{\frac{(c_{11}-c_{12})/2}{\rho}}$	5.10	-5.10	0

(a)

(b)
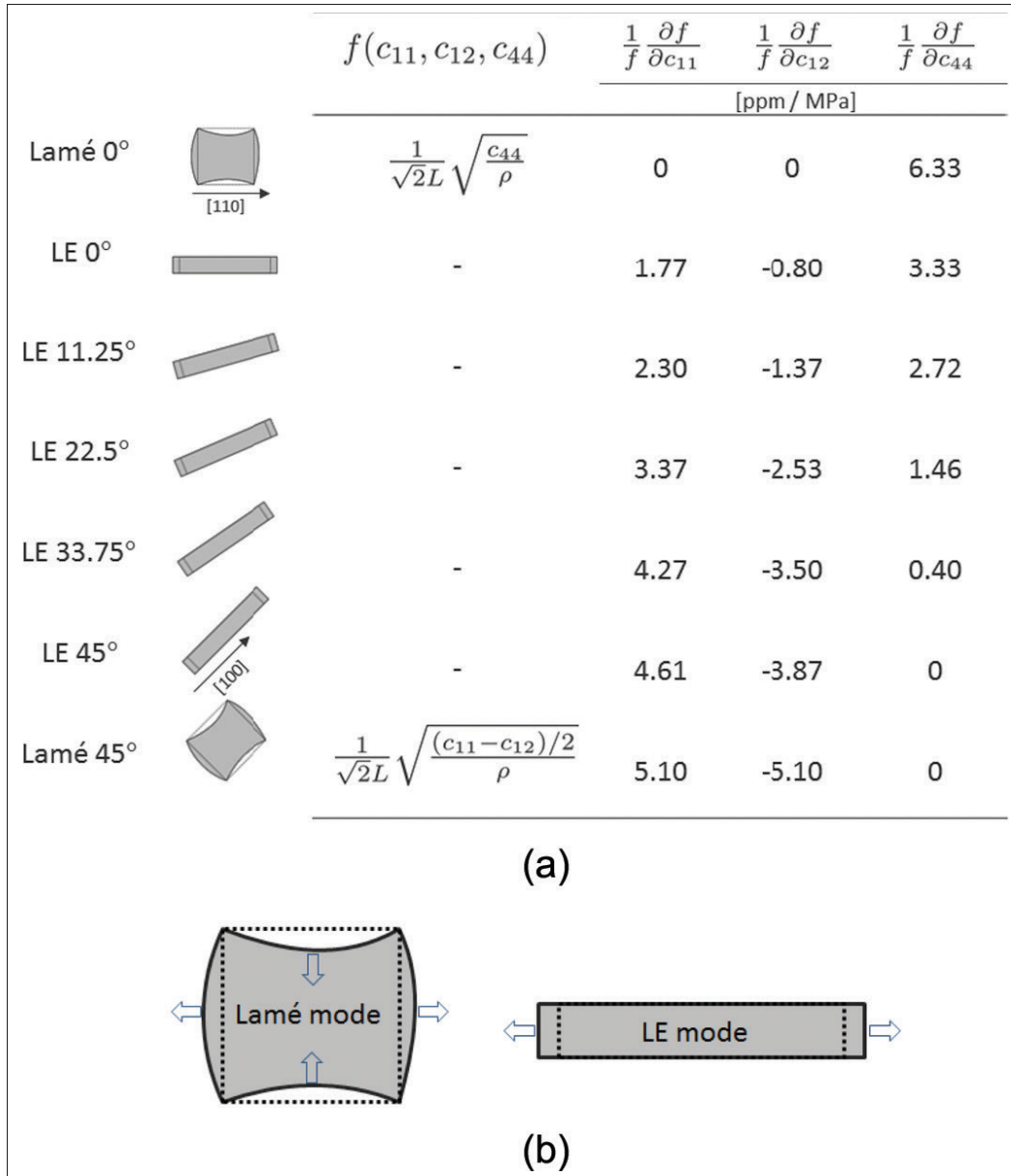
Figure 1.7 (**a**) The elastic constants c_{11}, c_{12}, and c_{44} were studied for seven resonant modes where the alignment is varied from [110] to [100]. The values are extracted from the finite element modeling (FEM) approach for silicon with $(c_{11}, c_{12}, c_{44}) = (163, 25, 79)$ GPa in 0-degree rotation. (**b**) The mode shapes of Lamé/LE resonators
Taken from Jaakkola *et al.* (2014b)

1.3.1.3 Adding a Layer onto the Resonator Surface

In order to compensate for the temperature dependence of silicon-based resonators, one of the approaches for controlling the TCF is to add a layer on the surface of the resonator with a notably high stiffness. The deposition of one or more layers of materials with varying TCFs on the resonator may alter the resonator's temperature characteristics. For example, Melamud, Kim, Chandorkar, Hopcroft, Agarwal, Jha & Kenny (2007) presents a passive compensating approach using silicon dioxide (SiO_2). SiO_2 has a positive TCF in regards to the structural material (mainly silicon in the MEMS fabrication). This strategy may result in a second-order (parabolic) relationship between temperature and frequency. In addition, Thakar, Wu, Figueroa & Rais-Zadeh (2014) have developed a combined technique of temperature compensation based on multiple materials with varying TCF ranges to provide a broad temperature stability range.

The resonant frequency of a multilayer material composed of a silicon layer and a deposited SiO_2 layer can be determined as follows:

$$f_{total}^2 = \frac{m_{Si}}{m_{total}} f_{Si}^2 + \frac{m_{SiO_2}}{m_{total}} f_{SiO_2}^2 \qquad (1.9)$$

where f_{Si}^2 and $f_{SiO_2}^2$ are the silicon and SiO_2 eigenfrequencies for the Lamé resonator, respectively, m indicates the mass for each material. Taking the dimensions of a square Lamé resonator into consideration, this equation may be rewritten as (Melamud, Chandorkar, Bongsang Kim, Hyung Kyu Lee, Salvia, Bahl, Hopcroft & Kenny (2009)):

$$f_{total}^2 = \frac{\rho_{Si} h_{Si} f_{Si}^2 + \rho_{SiO_2} h_{SiO_2} f_{SiO_2}^2}{\rho_{Si} h_{Si} + \rho_{SiO_2} h_{SiO_2}}. \qquad (1.10)$$

The resonant frequency shift caused by the cantilever's thermal expansion is negligible. The observed variation in resonant frequency is assumed to be caused by the temperature dependency of the elastic properties of silicon with deposited silicon dioxide. Moreover, Amorphous

SiO$_2$ measurements indicate that the Young's modulus of SiO$_2$ has a positive TCF (Sandberg, Svendsen, Mølhave & Boisen (2005)) and it can be calculated as follow:

$$TCF = \frac{TCF_{SiO_2} + r(TCF_{Si})}{1 + r} \tag{1.11}$$

where

$$r = \frac{m_{Si}}{m_{SiO_2}} \frac{f_{Si}^2}{f_{SiO_2}^2}. \tag{1.12}$$

In order to achieve a zero-TCF resonator, the numerator of equation 1.11) must be zero. Therefore, it possible to calculate the amount of deposited SiO$_2$ for a resonator to fully compensate it for temperature. Figure 1.8 depicts the frequency–temperature relationship of [110]-oriented double-ended tuning forks (DETFs) with different flexural ratios r.
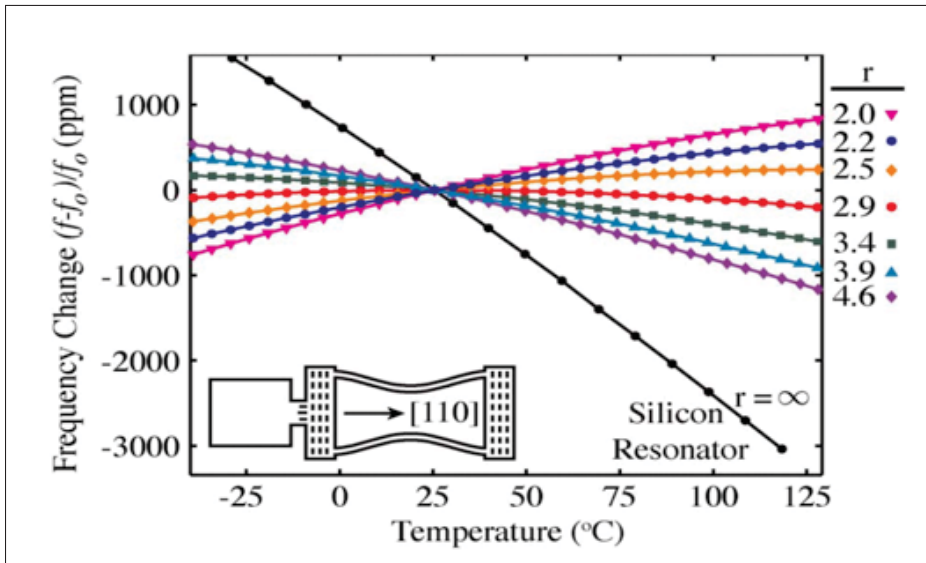
Figure 1.8   Measurements of frequency–temperature in
[110]-oriented composite DETF resonators. Solid lines are added
as a quadratic fit to data.The results are shown with various r ratios
and compared to a single silicon resonator material
Taken from Melamud *et al.* (2009)

Silicon is not the only material being researched for depositing a SiO_2 passivation layer. Ansari & Rais-Zadeh (2014) presents a GaN bulk acoustic wave resonator with fundamental thickness-mode resonance at 2.18 GHz. On the resonator stack, 400 nm of SiO_2 is placed on lowering the resonator TCF as depicted in figure 1.9. The SiO_2 layer also functions as a surface passivation layer for AlGaN/GaN HEMTs (high electron mobility transistors), hence enhancing voltage breakdown, frequency-dependent current leakage, and surface entrapment (Green, Chu, Chumbes, Smart, Shealy & Eastman (2000)).
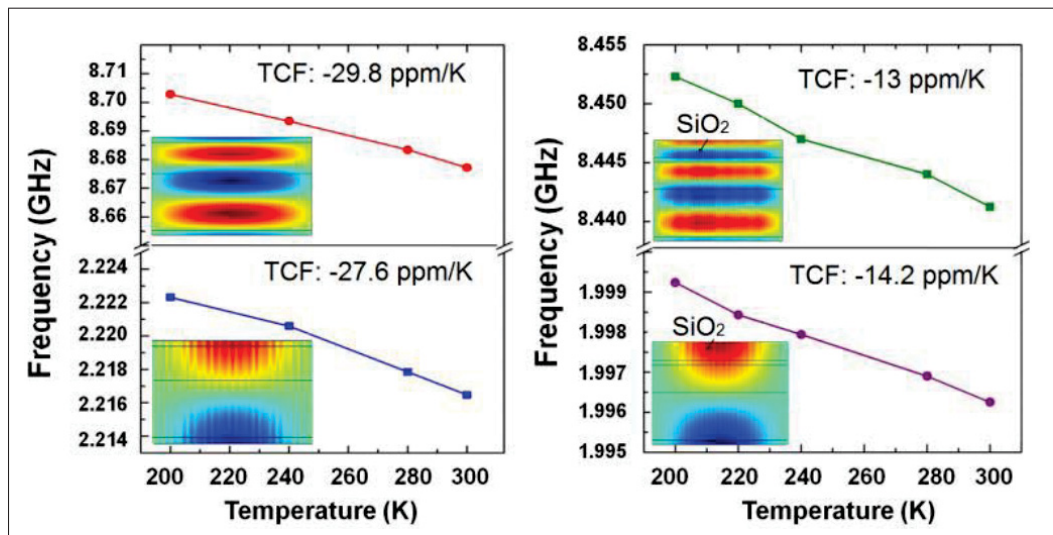
Figure 1.9   Trends in temperature comparison between two devices with and without a SiO_2 layer. Note that the stress profile at SiO_2 relies on the extent of temperature adjustment
Taken from Ansari & Rais-Zadeh (2014)

The TCF value of the GaN BAW resonator is lowered from approximately -30 ppm/K to -13 ppm/K, while the k_t^2 and Q of the device's fundamental thickness resonance are improved.

1.3.1.4   Resonators with an Array of Holes

Etch holes are introduced to facilitate and accelerate the HF (Hydrofluoric) etching for the buried oxide layer underneath the structural silicon device layer that represents the resonator structure. Civet, Casset, Carpentier, Icard, Bustos, Leverd, Mercier & Basrour (2011) has advocated the

use of holes for accurate frequency adjustment and Tu & Lee (2012b) has shown that designing holes into the resonator's structure may greatly reduce its Q where the extent of Q drop varied according to the location and distribution of the etch holes.

Despite reducing the Q, these holes may considerably enhance the TCF, enabling us to achieve a temperature-compensated resonator. Luschi, Iannaccone & Pieri (2017) has proposed a method for the temperature compensation of MEMS Lamé resonators based on the combined influence of doping concentration and hole geometry on the equivalent temperature coefficients of silicon. It is claimed that there are allegedly two conceivable conditions in which the first-order temperature coefficient of the resonant frequency becomes zero. The resonant frequency for a Lamé resonator equipped with holes is formulated as (Luschi & Pieri (2016)):

$$f = \frac{1}{L}\sqrt{\frac{E\left[1+(1-\beta)\beta^{k-1}\right]}{4(2-\beta)\rho\left[1+\beta^{k-1}(1-\beta)^2+\beta\left(1+\beta^{k-1}(1-\beta)\right)\nu\right]}}, \tag{1.13}$$

where E is Young's modulus, ν is Poisson's ratio, β is filling factor and k is a fitting parameter that can be obtained from a finite element methods (FEM) simulation. The general formulation of the Young's module and Poisson's ratio are given by (Brantley (1973)):

$$\frac{1}{E_{hkl}} = s_{11} - 2\left((s_{11} - s_{12}) - \frac{1}{2}s_{44}\right)\left(l_x^2 l_y^2 + l_y^2 l_z^2 + l_x^2 l_z^2\right), \tag{1.14}$$

$$\nu = -\frac{s_{12} + \left(s_{11} - s_{12} - \frac{1}{2}s_{44}\right)\left(l_x^2 m_x^2 + l_y^2 m_y^2 + l_z^2 m_z^2\right)}{s_{11} - 2\left(s_{11} - s_{12} - \frac{1}{2}s_{44}\right)\left(l_x^2 l_y^2 + l_y^2 l_z^2 + l_x^2 l_z^2\right)}, \tag{1.15}$$

where l_x, l_y, l_z, m_x, m_y and m_z are the direction cosines of the angle between the propagation direction and the desired axis. s_{11}, s_{12} and s_{44} represents the corresponding values in the compliance tensor. The relation between stiffness and compliance tensor in a cubic crystal can be expressed as NYE (1987):

$$s_{11} = \frac{c_{11} + c_{12}}{(c_{11} - c_{12})(c_{11} + 2c_{12})},$$

$$s_{12} = \frac{-c_{12}}{(c_{11} - c_{12})(c_{11} + 2c_{12})}, \tag{1.16}$$

$$s_{44} = \frac{1}{c_{44}}.$$

Consequently, the TCF for Lamé resonators with an array of holes within the structure can be calculated by carrying the derivative of (1.13) concerning the temperature such that (Luschi *et al.* (2017)):

$$TCF = \frac{1}{2L}\frac{\partial L}{\partial T} + \frac{1}{2E_p}\frac{\partial E_p}{\partial T}$$
$$- \frac{1}{2}\left[\frac{\beta + \beta^k(1 - \beta)}{1 + \beta^{k-1}(1 - \beta)^2 + \left[\beta + \beta^k(1 - \beta)\right]\nu_p}\right]\frac{\partial \nu_p}{\partial T}. \tag{1.17}$$

As shown by Equation (1.17), the TCF may be changed based on the filling factor.

1.3.1.5   Pillars in the Resonator Structure

A composite Si/SiO$_2$ structure may boost the relative contribution of SiO$_2$ in TCF$_1$, and the compensatory SiO$_2$ can be included in the main body of the silicon resonant structure. This method involves etching a matrix of SiO2 pillars in a desired pattern onto the resonator. Tabrizian, Casinovi & Ayazi (2010) has investigated a matrix of evenly distributed silicon dioxide pillars implanted inside the silicon substrate to create a homogeneous composite silicon oxide platform (SilOx) with almost ideal temperature-compensated stiffness.
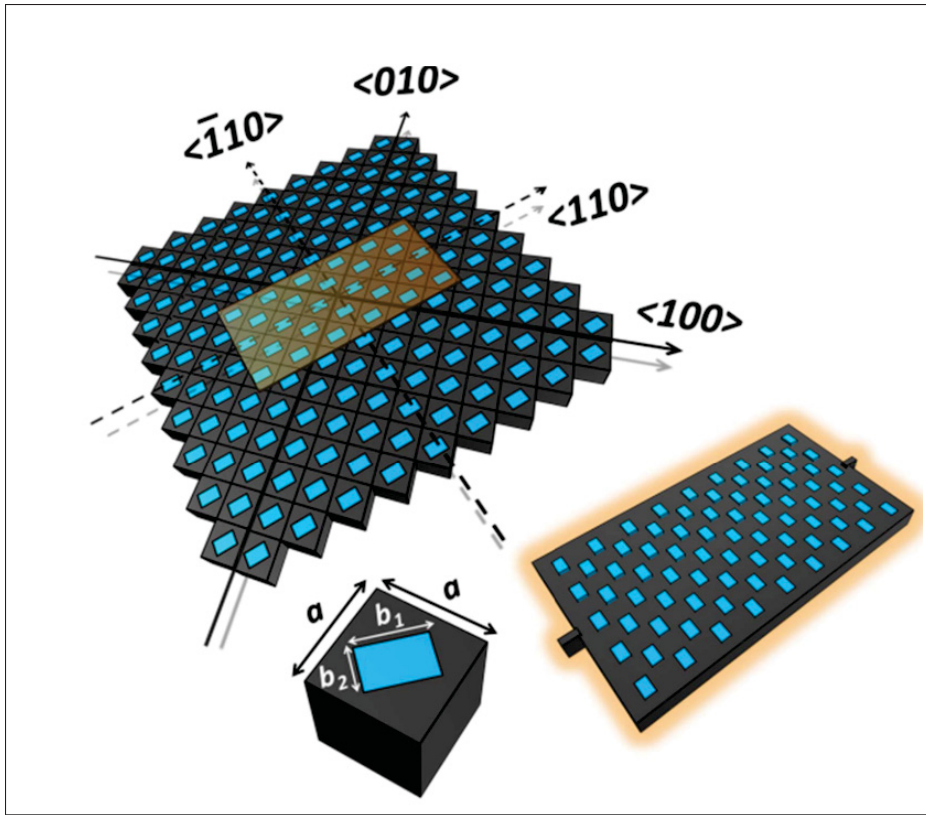
Figure 1.10   The resonator structure with rectangular SilOx holes,
where a and $b_{1,2}$ are the lateral dimensions of the SilOx unit and
SiOx pillar, respectively
Taken from Tabrizian *et al.* (2013)

The additional SiO_2 may be implanted in series with silicon in the direction of the acoustic waves traveling in-plane. Consequently, a fully temperature-compensated resonator with a high TCF_1 can be made using a small quantity of SiO_2 Tabrizian *et al.* (2013). Figure 1.10 depicts a rectangular SilOx resonator aligned in the <100> crystallographic direction of silicon. Figure 1.11 shows scanning electron microscope (SEM) pictures of a constructed SilOx resonator with the Aluminium Nitride (AlN) piezoelectric transduction mechanism. The SiO_2 pillars are visible due to the purposely over-etching of the resonator's silicon body.
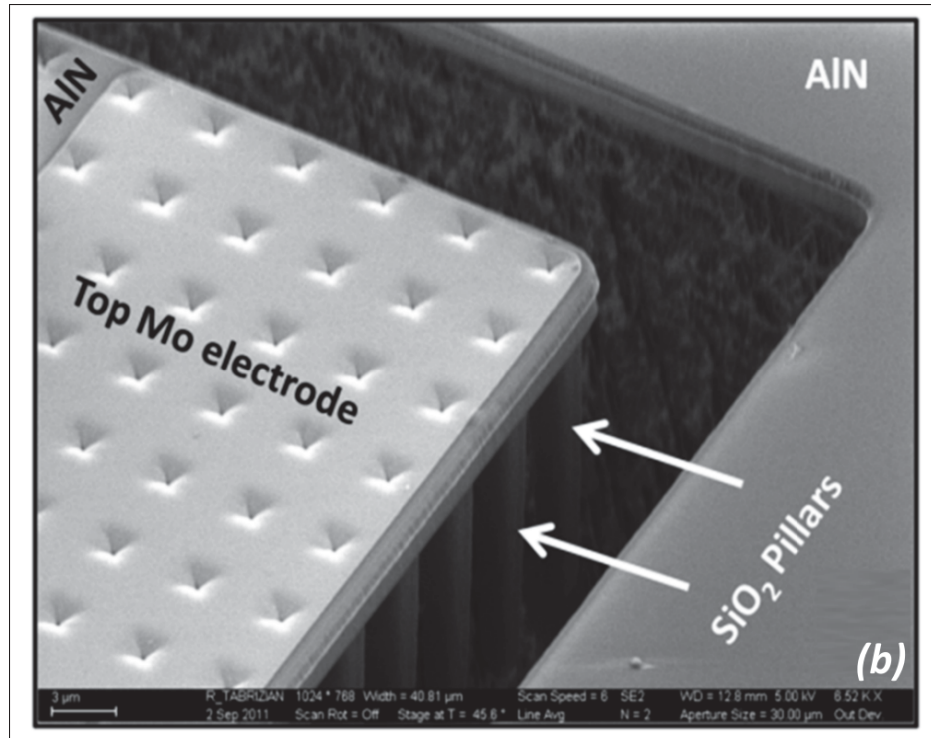
Figure 1.11   SiO$_2$ pillars extruding from the resonator sidewall
Taken from Tabrizian *et al.* (2013)

Tabrizian *et al.* (2013) reported a burn-in time of roughly ten days with a frequency stability of over 7.1 ppm; following the burn-in period, the frequency stability is steady within the range of ±1.2 ppm. This strategy for implementing resonators on SilOx platforms did not result in any Q or insertion loss deterioration when compared to silicon single-crystal structures. However, this fabrication technique is relatively complex and may not be amenable to a low-cost implementation.

1.3.2   Active Temperature Compensation

Active compensation approaches are often more effective than passive compensation techniques in achieving temperature stability, however they come expense of a higher power consumption and a larger area occupancy. Active temperature compensation techniques, such as adjusting the DC bias for electrostatic resonators, employing a phase-locked loop (PLL) to stabilize the

oscillation frequency, and implementing a micro-oven close to the resonator, are frequently utilized to achieve sub-ppm resonant frequency stability. This approach may be improved by using input from the resonator as feedback and reacting appropriately to the observed trend.

The active methods can be categorized as follow:

1.3.2.1 Resonator DC Bias

Typically, considering structural silicon with negative TCF, the uncompensated oscillator has a negative TCF, indicating that as the temperature rises, the oscillation frequency lowers. In addition, depending on the structure and mode shape of the resonator, the DC polarisation voltage may either enhance or reduce the resonant frequency. This phenomenon has been used to regulate the frequency drift of a resonator and lessen its temperature dependence. This approach significantly improves the oscillator's long-term stability, making MEMS resonators ideal for industrial applications.

Figure 1.12 illustrates the SEM picture of an in-plane resonator equipped with a comb drive and a 2 μm air gap. At room temperature, the resonant frequency is 27.8 kHz when the DC bias is 20 V (Islam, Wei, Lee, Xie, Mandal & Feng (2018)). The manufactured resonator has a TCF of -34.9 ppm/°C, and its resonant frequency is proportional to the voltage provided to the DC bias pin. Due to the large variation in resonant frequency induced by temperature change, it may be impossible to properly compensate the resonator for temperature.
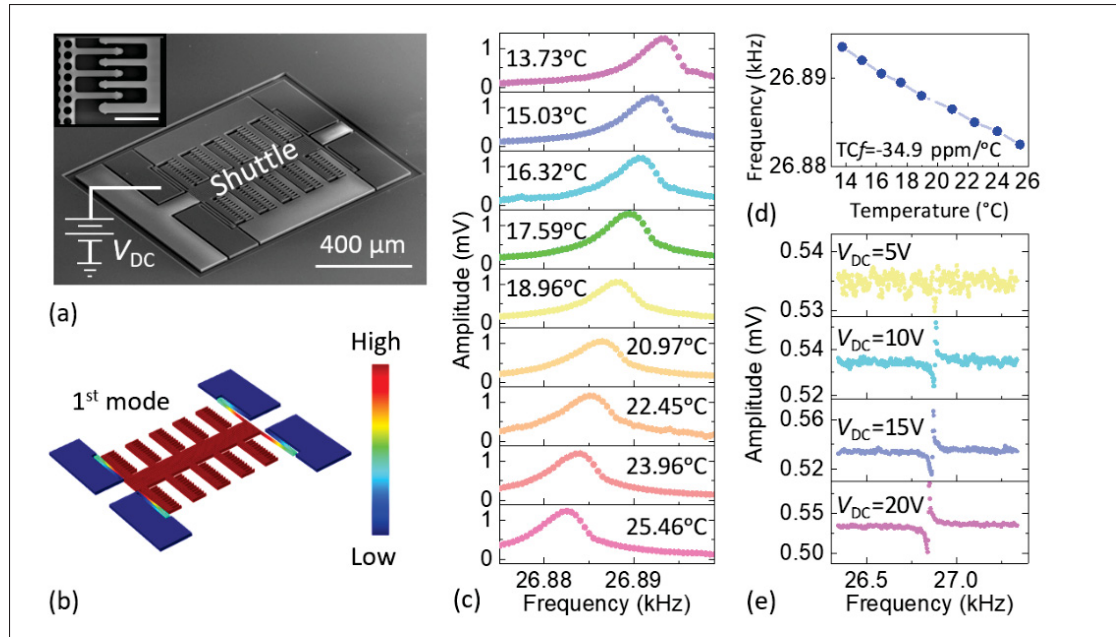
Figure 1.12   SiO$_2$ Single-crystal Si-on-insulator comb-drive MEMS resonator. (**a**) MEMS resonator captured through scanning electron microscopy. The inset depicts a zoomed-in perspective of the comb drive and fingers. (**b**) Simulation of the vibration pattern and form of the first mode. (**c**) optically calculated frequency response during the first resonant as temperature rises. (**d**) Temperature dependency of the open-loop resonant frequency for TCF derivation from the data in (**c**). (**e**) Electrical measurements of the shuttle's transmission and frequency response in response to different DC polarisation voltage applications. Since the measurement route consists of electrical and optical components, extracting the absolute calibration factors from the responses in (**c**,**e**) is challenging. Consequently, the responses have not been transformed into dimensionless transfer functions Taken from Islam *et al.* (2018)

1.3.2.2   Phase Locked Loop (PLL)

A phase-locked loop (PLL) is an electrical circuit that compares the phases of a reference signal (the resonator output clock) and an adjustable feedback signal coming from the circuit's output. Combining a high-Q resonator with a phase-locked loop may result in an oscillator with improved clock stability and temperature compensation by modifying the PLL divider and adequate noise performance due to the high-Q MEMS Voltage Controled Oscillator (VCO) in conjunction with the narrow bandwidth of the PLL (Chekurov, Grigoras, Sainiemi, Peltonen,

Tittonen & Franssila (2010)). A comprehensive temperature compensation system would have a temperature measuring block, digital logic to store frequency coefficients (i.e., calibration coefficients) and run the compensation algorithm, and a PLL to alter the output frequency in response to temperature fluctuations. As illustrated in figure 1.13, a PLL's output frequency is dependent on the divider N, and the reference frequency f_{ref} as follows:

$$f_{out} = f_{ref} \times N. \tag{1.18}$$

Typically, a temperature sensor close to the resonator is placed to measure the temperature and change the divider N appropriately. Gronicz, Aaltonen, Chekurov & Halonen (2016) has presented a strategy for using double-loop PLLs to improve noise performance and overcome the poor tunability of MEMS resonators. The bandwidths of the inner loop and the entire system have been chosen to be more than ten times to ensure that the dynamics of the PLL's inner loop and the bandwidth of the entire system are not significantly influenced by one another.
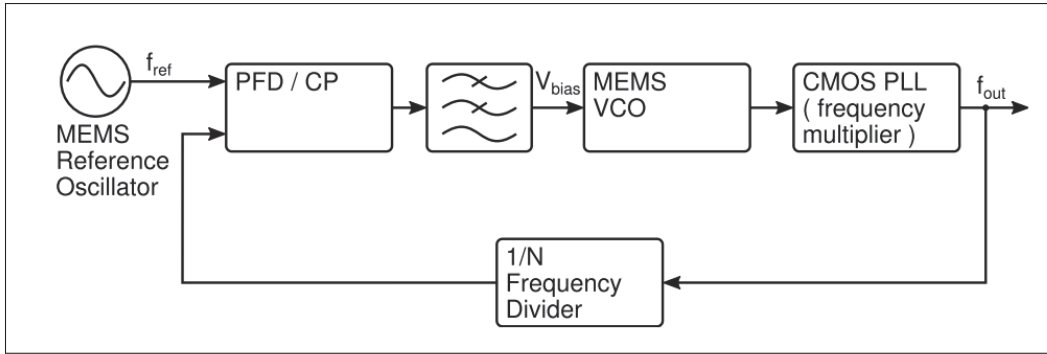
Figure 1.13   The architecture of a hybrid phase-lock loop (PLL) with
MEMS reference oscillator
Taken from Gronicz *et al.* (2016)

Notably, MEMS resonators and CMOS chips' production methods may be compatible with a conventional silicon-based fabrication process. This enables the development of wholly integrated frequency references using MEMS-based oscillators.

1.3.2.3   Ovenization

The use of a micro-oven to warm up the MEMS resonator structure is not a novel idea; it has previously been utilised in quartz crystal oscillators (OCXO - Oven Controlled Crystal Oscillator) to give temperature and frequency control to produce the highest accuracy acoustic resonator-based oscillators (Liu, Tabrizian & Ayazi (2018a)). Nevertheless, combining the heater with a quartz resonator on the same die has proven problematic; thus, decreasing the power consumption of the heater is complex since the heater and resonator cannot be stacked. Thanks to silicon and industrial MEMS manufacturing, the micro-oven and MEMS resonator may be combined onto the same substrate, resulting in a temperature-compensated resonator with a smaller footprint and lower power consumption.

Sundaresan, Ho, Pourkamali & Ayazi (2006) has created a 100MHz MEMS SiBARfactor oscillator in which the high-Q capacitive silicon bulk resonator was self-heated using the resistive body of a rectangular silicon beam resonator as a heater. According to this research, active compensation increased temperature stability by a ratio of 52 times. Lamé is positioned above the Lamé resonator and operates at 90 mW. In addition, a low-power consumption micro-oven is exhibited in "Comenencia Ortiz 2020 Low-Power Temperature, and the oven uses just 18 W to regulate the resonator frequency at temperatures as high as 100 C.

1.4   Fabrication Process

This work's resonators were manufactured using MEMSCAP's PiezoMUMPs bulk micromachining technology. The sequence of the manufacturing process is detailed in Cowen, Hames, Glukh & Hardy (2014). It begins with 150 mm double-sided polished n-type silicon on insulator (SOI) wafers. Phosphosilicate glass (PSG) is used to dope the top silicon surface to boost its conductivity. This top silicon layer (also know as the device layer) represents the primary structural layer utilized to create the device. Then, a 200 nm-thick silicon dioxide layer is grown and then patterned using reactive ion etching (RIE). In regions devoid of aluminum nitride, this thermal oxide helps to electrically insolate the signal pads and interconnects from the ground

36

plane. A 500 nm-thick layer of aluminum nitride is then deposited, patterned, and wet etched. A metal stack made of 20 nm-thick chrome and 1 μm-thick aluminum is then deposited and patterned using a lift-off technique to create the electrical interconnects and pads. To create the structural layer, the silicon device layer is lithographically patterned and etched using deep reactive ion etching (DRIE). Following this, a protective layer is applied to the front side of the wafer in order to allow for the following backside etching. The wafer backside silicon layer is subsequently patterned and etched using DRIE to create trenches that terminate at the buried oxide layer. The now-exposed buried oxide layer in the trenched sections is then removed using a wet oxide etch. Dry plasma etching ultimately removes the frontside protective layer, releasing the resonator structure and allowing it to move freely, while being supported at its four vertices through beams that are anchored by areas that do not have trenches below them.

1.5 Conclusion

The behavior of silicon as a material in MEMS fabrication is succinctly summarised in this chapter. The physics underlying silicon's elastic constants have been investigated, and the impact of temperature on these constants is discussed. It has been suggested to use both active and passive techniques to increase the temperature stability of MEMS silicon-based resonators. Therefore, active and passive compensation may be utilized to create highly stable resonators suitable for low-jitter timing references.

This dissertation seeks to study the known passive techniques to reduce the absolute TCF and provide a model that reliably predicts the resonator's behavior when each passive technique is applied. To further improve resonator performance, such as temperature stability and transmission, a novel Lamé resonator with chevron-shaped thermal actuators is developed to strengthen the active compensation technique and provide a path to lower the resonator's temperature dependence.

TEMPERATURE DEPENDENCE MODELING AND THERMAL SENSITIVITY REDUCTION OF BULK MICROMACHINED SILICON MEMS LAMÉ RESONATORS

Amir-Reza Kolahdouz-Moghaddam[1] , Seyedfakhreddin Nabavi[1] , Frederic Nabki[1]

[1] Département de Génie Électrique, École de Technologie Supérieure,
1100 Rue Notre-Dame Ouest, Montréal, Québec, H3C 1K3, Canada

Abstract: The elastic properties of structural materials considerably influence the resonant frequency of silicon MEMS resonators and their sensitivity to temperature variations. This work studies the effect of several methods on the temperature coefficient of frequency (TCF) of bulk micromachined silicon Lamé resonators. These include depositing a thin silicon oxide layer onto the resonating structure, including holes within the structure, and modifying the crystalline orientation of the structural layer. Devices variants are fabricated in a standard fabrication process (PiezoMUMPs by MEMSCAP) and are characterized with respect to their temperature dependence. An analytical model is proposed to predict the effects of each of the studied design variations on the resonant frequency and the temperature stability of the devices, and the results stemming from the model agree with the experimental measurements. It is found that a 45-degree rotated Lamé resonator with holes and a top oxide layer exhibits a 31.7% improvement in TCF in comparison to a simple Lamé resonator structure without rotation. This results in a 51.9% frequency drift reduction over a temperature range of 30°C to 100°C in comparison to a conventional structure.

2.1   Introduction

Over the past decades, microelectromechanical systems (MEMS) resonators have been widely utilized for numerous applications, such as accelerometers, gyroscopes, ultrasound transducers,

and oscillators. Silicon has been used in integrated circuits for many years, and MEMS structures have also been leveraging it (Abdolvand *et al.*, 2016). Indeed, silicon plays a crucial role in the microelectronics industry due to its outstanding features, including physical properties, low-cost processing, and reliable integration. Despite the advantages of using silicon, MEMS silicon-based resonators suffer from strong thermal frequency drifts (Wang, Bahr & Li, 2015b), meaning that any variation in the ambient temperatures will significantly alter the resonant frequency of MEMS resonators. This undesirable behavior has to be mitigated in order to allow for the highly-accurate frequency responses required by applications such as timing oscillators or electromechanical filters.

To address the stability of MEMS resonators, factors contributing to the silicon's behavior have to be identified through a mechanical parameters characterization study (Jaakkola, Prunnila & Pensala, 2012) and mechanical structure modeling (Ng, Hong, Yang, Ahn, Everhart & Kenny, 2015; Pensala, Prunnila & Jaakkola, 2012; Duwel, Candler, Kenny & Varghese, 2006; Melamud *et al.*, 2009). Thus far, many approaches have been proposed to reduce the effects of temperature on the resonant frequency of MEMS resonators and improve their stability over a wide range of temperatures. These methods include altering the silicon doping (Ng *et al.*, 2015; Jaakkola *et al.*, 2012, 2015, 2014b; Rajai, Ahmed, Straeten, Xereas & Ahamed, 2019) or heavy silicon doping (Samarao, Casinovi & Ayazi, 2010), changing the silicon crystalline orientation (Zhu & Lee, 2014; Jaakkola *et al.*, 2012), using an added layer onto the resonator surface such as silicon oxide (SiO_2) (Melamud *et al.*, 2009; D. M. Chen, Kuypers, Gaidarzhy & Zolfagharkhani, 2013), modifying the geometry of the resonator by considering an array of holes into the structure (Luschi *et al.*, 2017; Luschi & Pieri, 2016; Tu & Lee, 2012a), and altering the anchor shape (Chen, Wang, Jia, Yang, Yuan, Zhu & Yang, 2021). Moreover, active methods such as dynamically changing the resonator's bias voltage (Elsayed & Nabki, 2019, 2017b) or the use of micro-heaters near the resonator (Liu *et al.*, 2018a; Nabki, Cicek, Dusatko & El-Gamal, 2011) have been proposed. More sophisticated methods involving a phase-locked-loop (PLL) and temperature sensor to regulate the resonator's output frequency have also been proposed, while they require

complex circuit and significant power consumption in comparison to the aforementioned passive methods (Lee *et al.*, 2012).

The Lamé resonator's elevated quality factor (Chen *et al.*, 2021; Jaakkola, Gorelick, Prunnila, Dekker, Pensala & Pekko, 2014a), high resonant frequency (Bouchami, Elsayed & Nabki, 2018), small footprint (Lee, Zhu & Seshia, 2008) and ability to integrate with single-ended or differential circuits (Islam, Singh, Xereas, Chodavarapu & Mandal, 2019; Bouchami, Elsayed & Nabki, 2019) have made this structure prominent among other bulk mode resonators.

Accordingly, this work studies different passive methods to reduce the temperature sensitivity of bulk micromachined silicon Lamé resonators fabricated using the PiezoMUMPs micro-fabrication process by MEMSCAP. The paper investigates the impact of adding an oxide layer above the structure including holes within the structure, and varying the orientation of the crystalline structure. These proposed Lamé resonators are fabricated in four different design categories and four orientations, providing sixteen device variants. It is also shown that using a derived analytical model, the resonant frequency and frequency-temperature dependency of the devices can be predicted once elastic parameters are extracted from the measurements.

The remainder of this paper is organized as follows: Section II presents the theoretical background and analytical modeling of the resonator's temperature-sensitive properties. Section III presents the design of the proposed devices and the micro-fabrication process. The experimental results and analytical model predictions of the fabricated devices are presented in Section IV. Section V discusses the measurements of the different Lamé resonator variants, focusing on the impact of the studied techniques on temperature compensation, and it is followed by a conclusion.

2.2 Theoretical Background and Analytical Modeling

2.2.1 Lamé Mode Resonant Frequency

The elastic constants used in a lumped element model dictate the behavior of the resonator. Hence, the resonant frequency of a square Lamé resonator with a side dimension of L and a thickness of h can be represented as:

$$f = \frac{1}{2\pi}\sqrt{\frac{k_c}{m}} = \frac{1}{L_{eff}}\sqrt{\frac{c_{eq}}{\rho}} = \sqrt{\frac{h\,c_{eq}}{2m}}\,, \tag{2.1}$$

where k_c, m, L_{eff}, c_{eq}, ρ and h are the spring constant, resonator mass, characteristic resonator length (i.e., $\sqrt{2}L$), material stiffness, material density and resonator thickness, respectively.

Single crystal silicon can be considered to be a linear material; therefore, the relation between the stress and strain of the material within a continuous elastic material is similar to Hooke's Law for small strains ($\left|\frac{T-T_0}{T}\right| \ll 1$) (Sähn, 1972):

$$\sigma_{ij} = C_{ijkl}\left[\varepsilon_{kl} - \alpha_{kl}\left(T - T_0\right)\right], \qquad i, j, k, l = 1, 2, 3 \tag{2.2}$$

where σ_{ij} is the second-ranked stress tensor, C_{ijkl} is the fourth-ranked tensor stiffness (elasticity tensor), ε_{kl} is the second-ranked strain tensor, α_{kl} is the thermal expansion coefficient, T is the absolute temperature and T_0 is the ambient temperature when the structure is not deformed, respectively.

The stiffness matrix for a shear mode resonant such as present in a Lamé resonator can be presented as a fourth-order tensor given by:

$$C = \begin{bmatrix} c_{11} & c_{12} & c_{12} & 0 & 0 & 0 \\ c_{12} & c_{11} & c_{12} & 0 & 0 & 0 \\ c_{12} & c_{12} & c_{11} & 0 & 0 & 0 \\ 0 & 0 & 0 & c_{44} & 0 & 0 \\ 0 & 0 & 0 & 0 & c_{44} & 0 \\ 0 & 0 & 0 & 0 & 0 & c_{44} \end{bmatrix}. \tag{2.3}$$

The Christoffel equation for a cubic crystal is given in (2.4) (Zhang & Chen, 2013), where l_x, l_y and , l_z are the cosines of the propagation direction and ω is the resonant frequency in radians per second.

$$\begin{vmatrix} \left(\frac{k_c}{\omega}\right)^2 \{c_{11}l_x^2 + c_{44}(1 - l_x^2)\} - \rho & \left(\frac{k_c}{\omega}\right)^2 \{c_{12} + c_{44}\} l_x l_y & \left(\frac{k_c}{\omega}\right)^2 \{c_{12} + c_{44}\} l_x l_z \\ \left(\frac{k_c}{\omega}\right)^2 \{c_{12} + c_{44}\} l_y l_x & \left(\frac{k_c}{\omega}\right)^2 \{c_{11}l_y^2 + c_{44}\left(1 - l_y^2\right)\} - \rho & \left(\frac{k_c}{\omega}\right)^2 \{c_{12} + c_{44}\} l_y l_z \\ \left(\frac{k_c}{\omega}\right)^2 \{c_{12} + c_{44}\} l_z l_x & \left(\frac{k_c}{\omega}\right)^2 \{c_{12} + c_{44}\} l_z l_y & \left(\frac{k_c}{\omega}\right)^2 \{c_{11}l_z^2 + c_{44}\left(1 - l_z^2\right)\} - \rho \end{vmatrix} = 0 \tag{2.4}$$

In Fig. 2.1, a cubic crystal with its orientation planes is presented. In this work, a commercially available micro-fabrication process, namely PiezoMUMPs by MEMSCAP, is used to fabricate the resonators. In this fabrication process, a 150 mm diameter silicon-on-insulator (SOI) wafer with a (100) crystal orientation is used, and all resonators are designed in the same (100) plane. Therefore, the x-axis is orthogonal to the resonator plane, and in the Lamé mode, the resonance occurs in the (100) plane. As a result, I_x is zero and thus (2.4) can be rewritten as (2.5).

$$\begin{bmatrix} \left(\frac{k_c}{\omega}\right)^2 \{c_{44}\} - \rho & 0 & 0 \\ 0 & \left(\frac{k_c}{\omega}\right)^2 \{c_{11}l_y^2 + c_{44}\left(1 - l_y^2\right)\} - \rho & \left(\frac{k_c}{\omega}\right)^2 \{c_{12} + c_{44}\} l_y l_z \\ 0 & \left(\frac{k_c}{\omega}\right)^2 \{c_{12} + c_{44}\} l_z l_y & \left(\frac{k_c}{\omega}\right)^2 \{c_{11}l_z^2 + c_{44}\left(1 - l_z^2\right)\} - \rho \end{bmatrix} \begin{bmatrix} v_x \\ v_y \\ v_z \end{bmatrix} = 0 \tag{2.5}$$
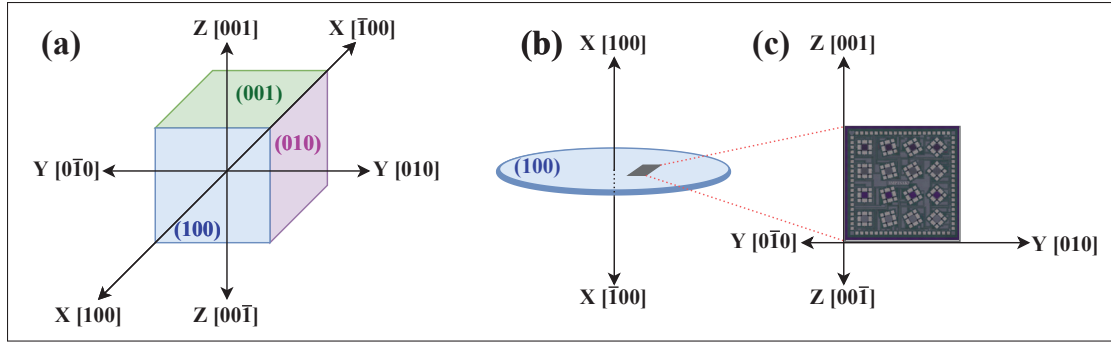
Figure 2.1   Silicon crystal planes and natural axes in a (100) wafer. (**a**) Face-centered cubic crystal structure, (**b**) axes and directions in a (100) wafer, and (**c**) proposed design orientation and axes

By solving (2.5), the wave propagation in the (100) face can be divided into a linear factor (pure shear) and two quadratic factors (quasi-shear, quasi-longitudinal) such that:

$$\frac{k}{\omega_1} = \sqrt{\frac{\rho}{c_{44}}} \, ,$$

$$\frac{k}{\omega_{2,3}} = \sqrt{\frac{2\rho}{c_{11} + c_{44} \pm \sqrt{(c_{11} - c_{44})^2 \cos^2 2\phi + (c_{12} + c_{44})^2 \sin^2 2\phi}}},$$

(2.6)

where ϕ is the angle between the Y-axis and the resonant vector. It can then be deduced that $\cos\phi = l_y$.

It can be seen that in shear modes along $< 110 >$ (Lamé mode along $< 100 >$) and shear modes along $< 100 >$ (Lamé mode along $< 110 >$), the numerical analysis converges to a deterministic analysis. By applying the conditions to the frequency of an acoustic resonator to (2.1), one can write the resonant frequency as:

$$f(c_{11}, c_{12}, c_{44}) = \begin{cases} \frac{1}{\sqrt{2}L}\sqrt{\frac{c_{44}}{\rho}} & for \quad \phi = 0 \\ \\ \frac{1}{\sqrt{2}L}\sqrt{\frac{c_{11} - c_{12}}{2\rho}} & for \quad \phi = 45 \end{cases}$$

(2.7)

2.2.2 Temperature Dependence of Lamé Resonators

Temperature variations significantly affect the elastic behavior of the silicon crystal; hence, the resonant frequency of a MEMS resonator is quite temperature-dependent. The frequency shift due to changes in temperature can be derived from (2.1) with a first derivative with respect to the temperature such that:

$$\frac{\partial f}{\partial T} = \frac{1}{\sqrt{2m}} \left(\frac{\partial \sqrt{h \, c_{eq}}}{\partial T} \right) = \frac{1}{\sqrt{8mh \, c_{eq}}} \left(c_{eq} \frac{\partial h}{\partial T} + h \frac{\partial c_{eq}}{\partial T} \right) \tag{2.8}$$

The temperature coefficient of frequency (TCF) is the rate of shift of frequency versus temperature from a reference frequency. Thus, by dividing the temperature-dependent frequency deviation by the reference frequency, the TCF is equal to:

$$\begin{aligned} TCF &= \frac{1}{f_0} \frac{\partial f}{\partial T} = \frac{1}{2hc_{eq}} \left(c_{eq} \frac{\partial h}{\partial T} + h \frac{\partial c_{eq}}{\partial T} \right) \\ &= \frac{\alpha}{2} + \frac{1}{2c_{eq}} \frac{\partial c_{eq}}{\partial T} \\ &= \frac{\alpha}{2} + \frac{1}{2} TC_{c_{eq}}, \end{aligned} \tag{2.9}$$

where α is the thermal expansion coefficient and $TC_{c_{eq}}$ is the temperature coefficient of equivalent stiffness. Accordingly, the TCF for a Lamé resonator is dependent on the elastic coefficient variation due to temperature change. In section 2.4, measurement results at different temperatures are presented.

2.2.3 SiO$_2$ Deposition on Lamé Resonators

An effective way to compensate for the silicon stiffness variations with temperature is adding a layer to the resonator structure that has an opposite stiffness variation with temperature. The deposited layer stiffness must be high enough to neutralize the total stiffness variation of the structure. Silicon dioxide (SiO$_2$) is a promising material for compensating the temperature

sensitivity of silicon resonators (Melamud *et al.*, 2009; D. M. Chen *et al.*, 2013), thanks to the positive TCF of SiO$_2$ (Abdolvand, Lavasani, Ho & Ayazi, 2008; Lakin, McCarron & McDonald, 2000) when compared to the substrate material (i.e., Si), as well as its ease of inclusion in silicon-based fabrication processes.

In a multi-layer material structure, the combined TCF depends on the TCF of each material layer and its thickness. The resulting resonant frequency for a double-layer material structure can be expressed as follows (Wang *et al.*, 2015b):

$$f_{total}^2 = \frac{m_{Si}}{m_{total}} f_{Si}^2 + \frac{m_{SiO_2}}{m_{total}} f_{SiO_2}^2 \tag{2.10}$$

where f_{Si} and f_{SiO_2} are the silicon and SiO$_2$ eigenfrequencies for the Lamé resonator, respectively, m indicates the mass for each material. By taking into account the dimensions of a square Lamé resonator, this equation can be rewritten as:

$$f_{total}^2 = \frac{\rho_{Si} h_{Si} f_{Si}^2 + \rho_{SiO_2} h_{SiO_2} f_{SiO_2}^2}{\rho_{Si} h_{Si} + \rho_{SiO_2} h_{SiO_2}}. \tag{2.11}$$

By taking the derivative of (2.10) with respect to the temperature and combining it with (2.1), the linear temperature coefficient for a Lamé resonator with the SiO$_2$ layer can be expressed as follows:

$$TCF_{total} = \frac{1}{f} \frac{\partial f}{\partial T} = \frac{m_{Si} f_{Si}^2 TCF_{Si} + m_{SiO_2} f_{SiO_2}^2 TCF_{SiO_2}}{m_{Si} f_{Si}^2 + m_{SiO_2} f_{SiO_2}^2}$$

$$= \frac{h_{Si} c_{Si} TCF_{Si} + h_{SiO_2} c_{SiO_2} TCF_{SiO_2}}{h_{Si} c_{Si} + h_{SiO_2} c_{SiO_2}}, \tag{2.12}$$

where c_{Si} and c_{SiO_2} are the silicon and SiO$_2$ stiffness, respectively.

As can be seen in (2.12), due to the different TCF sign between silicon and SiO_2, one can reduce the combined TCF of the structure that includes silicon and SiO_2 layers.

2.2.4   Lamé Resonators with an Array of Holes

In order to minimize Lamé resonators' susceptibility to temperature variation, an array of holes within the resonating structure can be used (Luschi *et al.*, 2017). However, the resonator quality factor decreases due to the thermo-elastic losses caused by the inclusion of holes within the structure(Luschi & Pieri, 2016). Advantageously, Lamé resonators have an inherently high quality factor (Elsayed & Nabki, 2019), and therefore, the reduction in quality factor due to the holes can potentially be tolerated.

The resonant frequency of the vibrating structure with holes will change according to the size and number of holes in the structure. In this regard, a metric, namely the filling factor, is introduced to determine the density of the holes as follows:

$$\beta = 1 - \frac{L_h}{e},\tag{2.13}$$

where e represents the hole pitch and L_h is the hole edge size. β is a number between 1 and 0, while $\beta = 1$ indicates a hole-free structure and $\beta = 0$ represents a completely hollow structure. The resonant frequency for a structure with holes can be estimated by (Luschi & Pieri, 2016):

$$f = \frac{1}{L}\sqrt{\frac{E\left[1+(1-\beta)\beta^{k-1}\right]}{4(2-\beta)\rho\left[1+\beta^{k-1}(1-\beta)^2+\beta\left(1+\beta^{k-1}(1-\beta)\right)\nu\right]}},\tag{2.14}$$

where E is Young's modulus, ν is Poisson's ratio, and k is a fitting parameter that can be obtained from a finite element methods (FEM) simulation(Luschi *et al.*, 2017).

Accordingly, the TCF for Lamé resonators with an array of holes within the structure can be calculated by taking the derivative of (2.14) with respect to the temperature such that (Luschi *et al.*, 2017):

$$TCF = \frac{1}{2L}\frac{\partial L}{\partial T} + \frac{1}{2E_p}\frac{\partial E_p}{\partial T}$$

$$- \frac{1}{2}\left[\frac{\beta + \beta^k(1-\beta)}{1 + \beta^{k-1}(1-\beta)^2 + \left[\beta + \beta^k(1-\beta)\right]\nu_p}\right]\frac{\partial \nu_p}{\partial T}. \tag{2.15}$$

As can be seen, by (2.15), depending on the filling factor, the TCF can be modified.

2.3 Design and Micro-Fabrication Process

2.3.1 Design
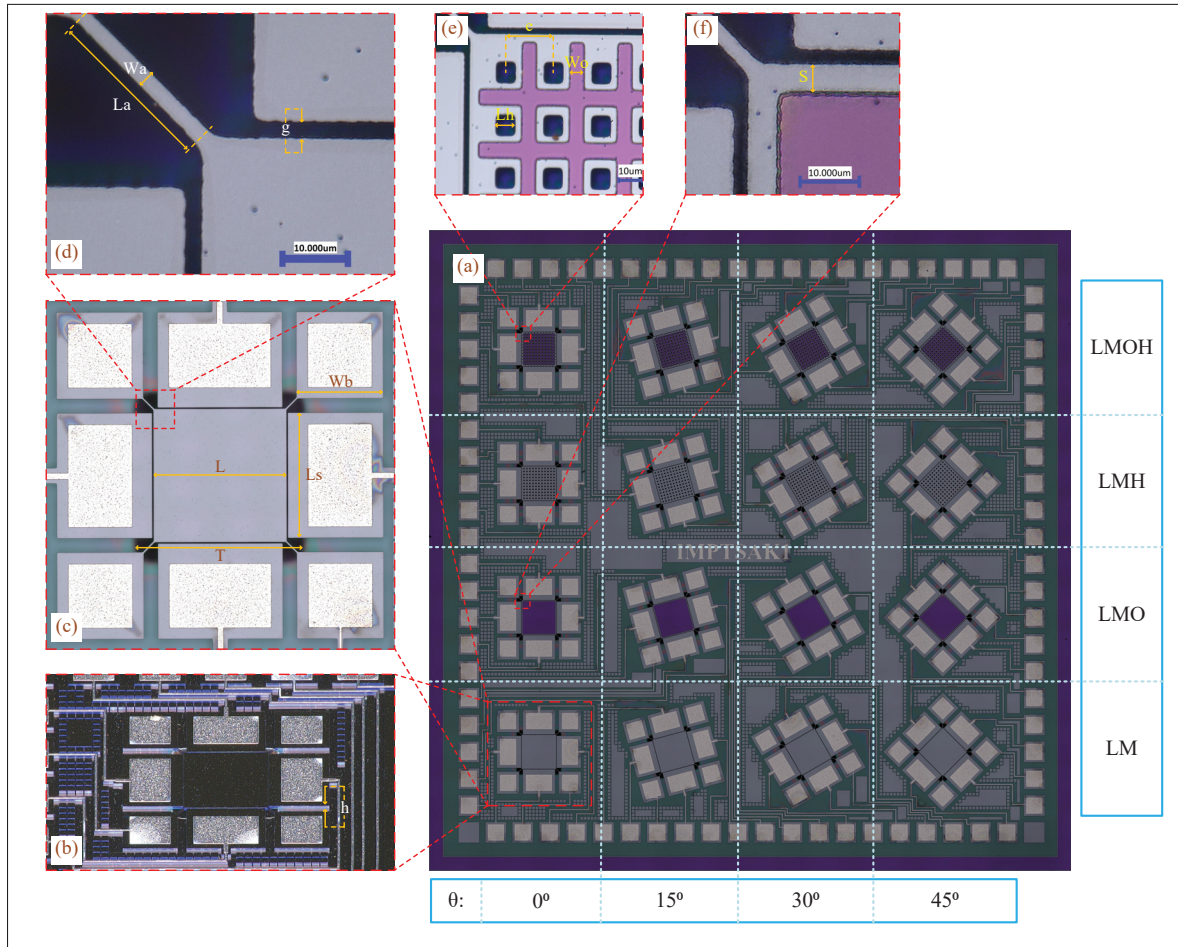
Figure 2.2 (**a**) The 4.3 mm by 4.3 mm die contains sixteen Lamé resonators composed of different types and rotational angles. (**b**) 45° tilted angle view of design LM_0. (**c**) LM_0 top view and dimensions, and (**d**) resonator electrostatic transducer gap. (**e**) LMOH_0 design hole structure and spacing with SiO_2 filling. (**f**) LMO_0 design SiO_2 layer with required edge clearance

In Figure 2.2, micrographs of the fabricated electrostatic Lamé resonators with different rotations and types are illustrated. The studied Lamé resonators are classified into four types:

1. Conventional Lamé resonators using a silicon structural layer (LM);

2. Lamé resonators with a layer of SiO$_2$ deposited onto the top of the structural layer (LMO);

3. Lamé resonators with an array of holes within the structural layer (LMH); and

4. Lamé resonators with an array of holes within the structural layer and SiO$_2$ deposited onto the structural layer (LMOH).

Each group has been fabricated in four rotation angles (0, 15, 30, and 45 degrees), the angle of which is indicated after the design type nomenclature for each design in this work. For instance, LMOH_45 denotes a Lamé resonator with holes, an SiO$_2$ layer on the resonator, and a rotation angle of 45 degrees.

Table 2.1   Geometric parameters of the proposed designs

Parameters	Symbol	Value (μm)
Resonator length	L	230
Sensing pad length	Ls	220
Trench width	T	278
Bias pad width	Wb	150
Anchor length	La	27
Anchor width	Wa	3
Gap	g	2
Holes pitch	e	20
Hole width	Lh	8
Oxide width	Wo	6
Oxide to SOI clearance	S	5
SOI Thickness	h	10

With reference to Figure 2.2, the suspended square structure has a 230 μm side length and is 10 μm-thick. It is anchored via four 27 μm-long corner-supports in each design. As is known,

the anchor topology plays a crucial role in the quality factor. As a result, the narrowest anchor size possible with the fabrication process is used, yielding a 3 μm width. Four rectangular pads around the suspended structure are used for both single and differential measurements. The effective pad width is 215 μm with a 2 μm air gap separation to the suspended square-shaped released structure.

The LMO and LMOH designs include a square of SiO_2 having a side length of 220 μm and 0.2 μm thickness (Pad Oxide layer). This thickness cannot be modified as it is imposed by the fabrication process. The holes in the LMH and LMOH designs have a width of 8 μm, and their pitch is 20 μm. The geometry details of all of the prototyped Lamé resonators are shown in Figure 2.2 and are summarized in Table 2.1.

2.3.2   Micro-fabrication process

The Lamé resonators were fabricated via MEMSCAP using the PiezoMUMPs process. Figure 2.3 illustrates the processing steps to fabricate a Lamé resonator with SiO_2 and holes.

In this fabrication process, a silicon-on-insulator (SOI) wafer with a 150 mm diameter with a (100) orientation 10 μm-thick doped silicon device layer is used (Figure 2.3a). Note that while this process provides a piezoelectric layer, it is not used in this work as the devices are electrostatically excited. A 0.2 μm-thick SiO_2 layer (Pad Oxide) is grown and patterned over the silicon (Figure 2.3b). The last layer is a 1 μm-thick aluminum film (Pad Metal) that can be utilized as the interconnect and for bond pads (Figure 2.3c). Then, the silicon device layer is lithographically patterned (Figure 2.3d). A polyimide coat is applied to the front side of the wafer, and the backside of the wafer is etched to form the suspended silicon structure (Figure 2.3e). The silicon substrate is etched from bottom to top, and the exposed buried oxide is removed to form trenches and release the silicon structure where appropriate (Figure 2.3f). The material details and their thicknesses are listed in Table 2.2. The critical dimension for the silicon device layer is 2 μm, which can be seen at the Lamé resonator electrostatic transducer gap in this work.

50
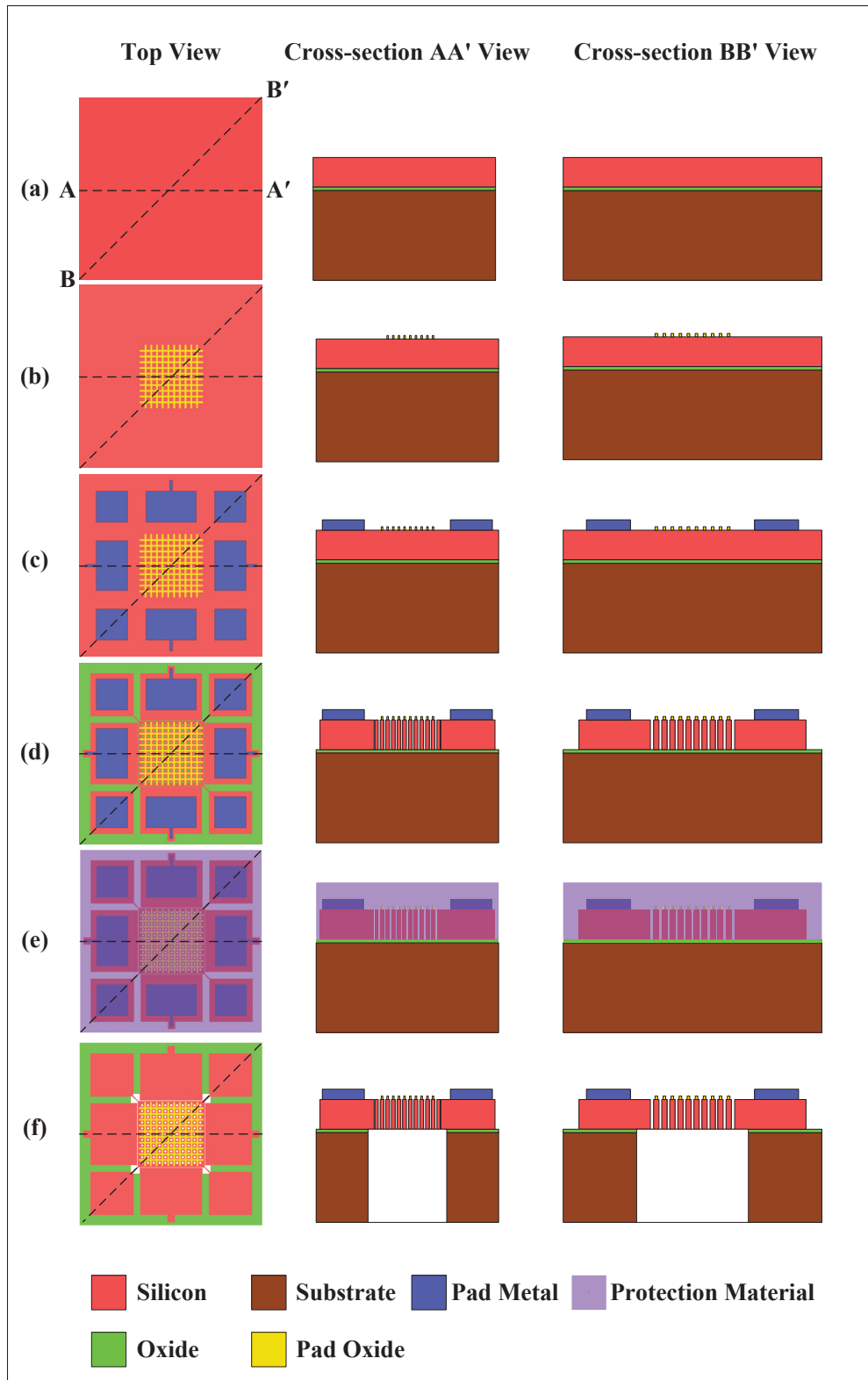
Figure 2.3   Summary of PiezoMUMPs manufacturing steps for a Lamé
resonator with holes and SiO$_2$

Table 2.2   PiezoMUMPs process layers characteristics

	Thickness (μm)	Error (μm)	Density ($\frac{kg}{m^3}$)	Layer Name
Substrate (Silicon)	400	±5	2320	Trench
Silicon device layer	10	±1	2320	SOI
SiO$_2$	0.2	±0.01	2200	Pad Oxide
Aluminium	1	±0.05	2710	Pad Metal

2.4   Experimental Results

2.4.1   Resonator Parameters Extraction Method

The transmission magnitude in the electrostatic Lamé resonator is proportional to the gap size. Therefore, the transmission peak in S-21 measurements is affected by the feedthrough capacitance due to the large transducer gap size imposed by the fabrication process (i.e., 2 μm). In general, the 3-dB bandwidth is used to measure the quality factor of resonators, while in large gap size Lamé resonators, such a measurement is not possible if the capacitance feedthrough is considerably high. In the large-scale measurement PCB presented in section 2.4.2, this is the case. By utilising a resonator electrical model, different parameters such as quality factor, resonator loss, feedthrough capacitor, etc. can be estimated nonetheless.

Generally, resonators are modeled based on the Butterworth-Van Dyke (BVD) model (Lee & Seshia, 2011). According to this model, the resonant behavior is estimated by a series RLC circuit, $R_s L_s C_s$, with a parallel capacitor, C_p. L_s and C_s fix the resonant frequency behavior, R_s models the resonator motional resistance (i.e., its loss), and C_p acts as feedthrough capacitor due to electrical parasitics. The resonant frequency, f_0, of the BVD model can be expressed as:

$$f_0 = \frac{1}{2\pi}\sqrt{\frac{1}{L_s C_s}}. \tag{2.16}$$

The quality factor for the series equivalent circuit can be expressed as:

$$Q_s = \frac{1}{R_s}\sqrt{\frac{L_s}{C_s}} = \frac{2\pi f L_s}{R_s}. \tag{2.17}$$

It can be assumed that it is feasible to measure the quality factor for a resonator even though the 3-dB bandwidth is not captured in the transmission curve. The BVD model is first determined by fitting the measured electrical transmission characteristic, then by using (2.17), the quality factor estimation can be done.

2.4.2   Test Setup

To characterize the resonators, a Vector Network Analyzer (VNA) (Keysight model E5061) is used to measure the frequency responses of the prototyped Lamé resonators. Two PCB versions have been designed. A PCB designed for an LCC package is shown in Figure 2.4(a) and named PCB1. It minimizes feedthrough capacitance in order to maximize the resonator transmission magnitude and validate device properties. Another design based on a CQFP package that can allow for the large-scale temperature testing of all of the devices on the same die without requiring repackaging is shown in Figure 2.4(b) and named PCB2.

The employed test setup with PCB2 is presented in Figure 2.5. As shown in this figure, both VNA ports were connected to DC blockers for short-circuit protection between the sensing electrodes and the DC bias. Since the single-ended signal must be converted to a differential signal with a 180-degree phase shift, a power divider (Minicircuits ZFSCJ-2-1-S+) was used on both VNA ports. A high voltage power supply (Keithley model 2260B) was used to create the DC polarization voltage, V_{bias}, for the electrostatic operation of the resonators. In order to limit the current flow in case of device failure, a 100 kΩ resistor was connected between the power supply and the DC bias pad. A PCB heater under the CQFP chip package is designed to heat the resonator structure in order to control the temperature. The die temperature is measured using a

thermal camera (ETS320, Flir). A Python script with a PID controller is developed to achieve and sustain each given temperature over the resonator structure.
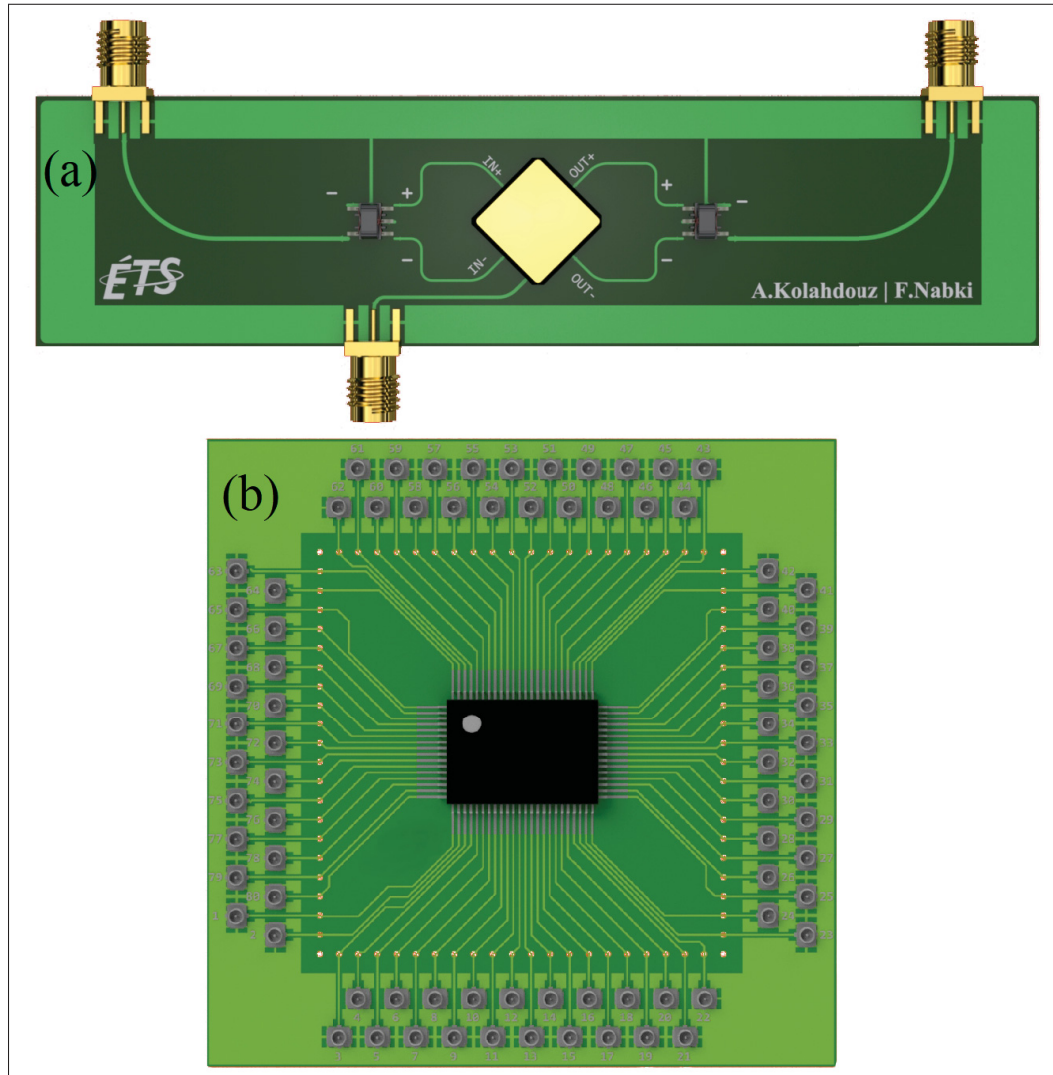
Figure 2.4   (**a**) Low feedthrough capacitance PCB with the LCC-28 package
, SMA connectors and integrated differential baluns (CX2074NL) (PCB1),
and (**b**) large-scale testing PCB with the CQFP-80 package and U.FL outputs
(PCB2)
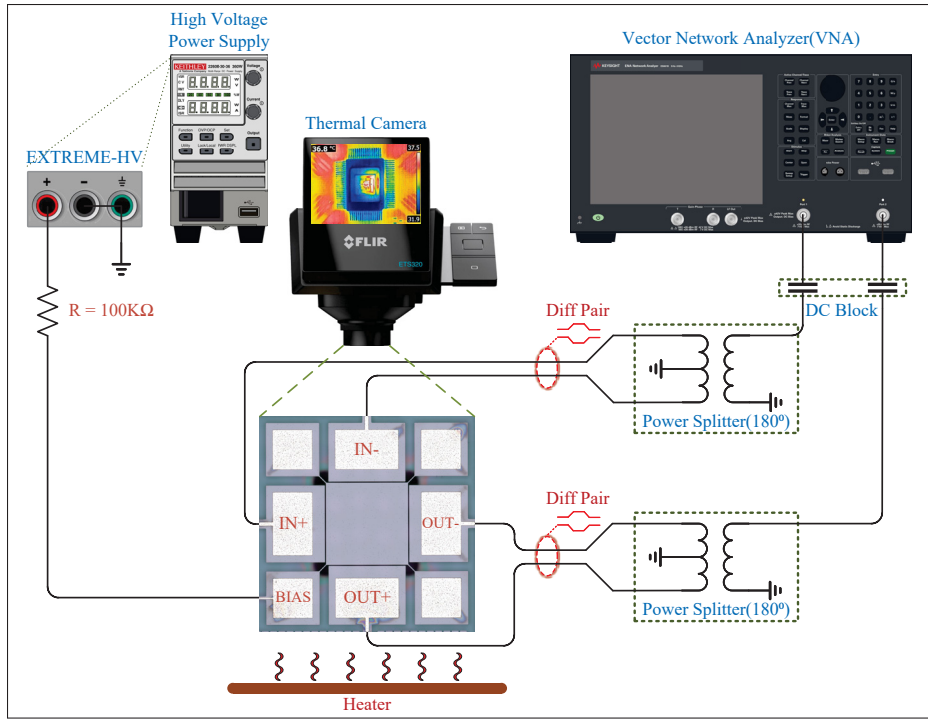
Figure 2.5 The differential test setup configuration used to measure resonant frequency temperature stability

PCB1 allows for a lower feedthrough capacitance and better insertion loss, as shown in Figure 2.6(a) by the transmission magnitude measured for a typical device. In this figure, the device is measured under 48 mTorr vacuum level and 200 V bias voltage. Alternatively, PCB2 facilitates the temperature testing of all of the resonators at the cost of higher feedthrough capacitance between inputs and outputs. This results in a reduced transmission magnitude, as shown in Figure 2.6(b). Nonetheless, PCB2 proves to be a practical method of monitoring the resonant frequency vs temperature of all of the resonators without having to reset the test setup or change the packaged die. It is thus used to characterize the devices vs temperature in this work. Figure 2.6 shows the resonant frequency of LM_0 in vacuum estimated using the BVD model. The equivalent circuit components are calculated using a curve fitting methodology across the center resonant frequency and are included in the figure, along with the measured Q-factor (when possible) and the calculated Q-factor.

It can be inferred that the quality factor is inherently dependent on the behavior of the resonator, while the measured 3-dB quality factor is highly susceptible to the PCB design. Thus, in the situation where the 3-dB quality factor cannot be measured due to the limitation of the test PCB, the BVD model can provide a reasonably accurate estimation for the quality factor. The measured Q-factor for devices LM_0 and LMOH_45 are 478,684 and 341,768, respectively. This matches well with the extracted values from the BVD model using the transmission characteristics from PCB1 or PCB2 for LM_0, as seen in Figure 2.6.
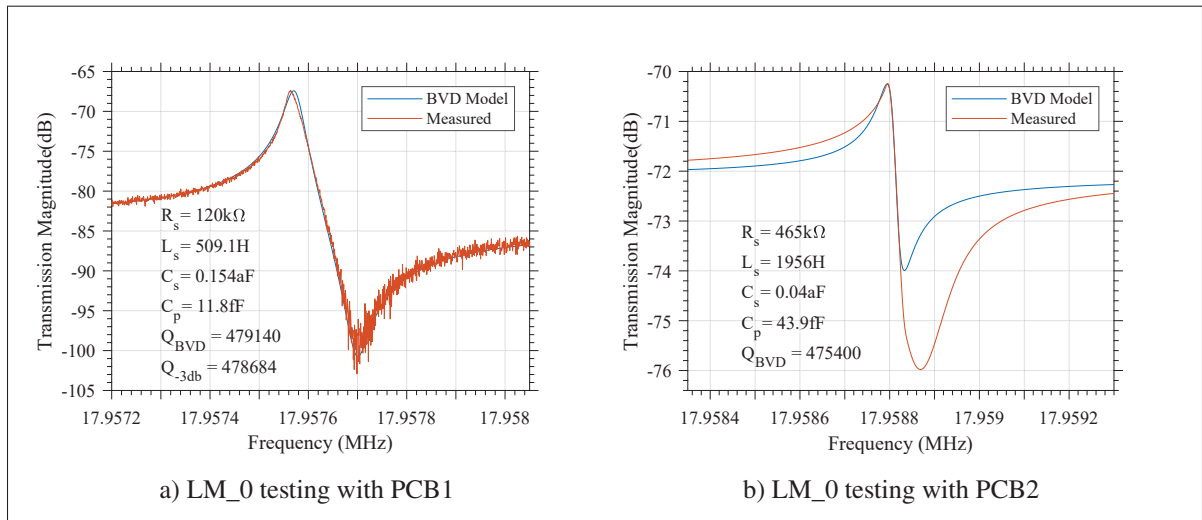
Figure 2.6 (**a**) LM_0 resonator transmission characteristic extracted using PCB1 under vacuum (48 mTorr) with a 200 V bias voltage, and (**b**) the LM_0 resonator transmission characteristic extracted with PCB2 under vacuum (48 mTorr) with a 200 V bias voltage

2.4.3 Resonator Characterization

The Lamé resonators described in Section 2.3 were characterized by measuring their frequency responses at different temperatures using PCB2.

To experimentally validate the analytical models presented in section 2.2, the sixteen fabricated Lamé resonators with the physical aspects listed in Table 2.1 were tested. The peripheral temperature of each resonator was swept at atmospheric pressure from 30°C to 100°C using

the integrated PCB heater. The resonant frequency at 30°C, frequency drift from 30° to 100°C, and TCF for each device are presented in Table 2.3. The resonant frequency for LM_0 is 17.96MHz at 30°C and atmospheric pressure. Figure 2.7 illustrates the resonant frequency of the Lamé resonator at 0-degree rotation vs temperature. Notably, it is seen that by increasing the temperature, the resonant frequency is reduced, as expected, due to the negative TCF of the silicon crystal. As formulated in (2.9), the TCF can be measured for all devices over the temperature variation. The TCF in this case for LM_0 is measured to be -55.42 ppm/°C.
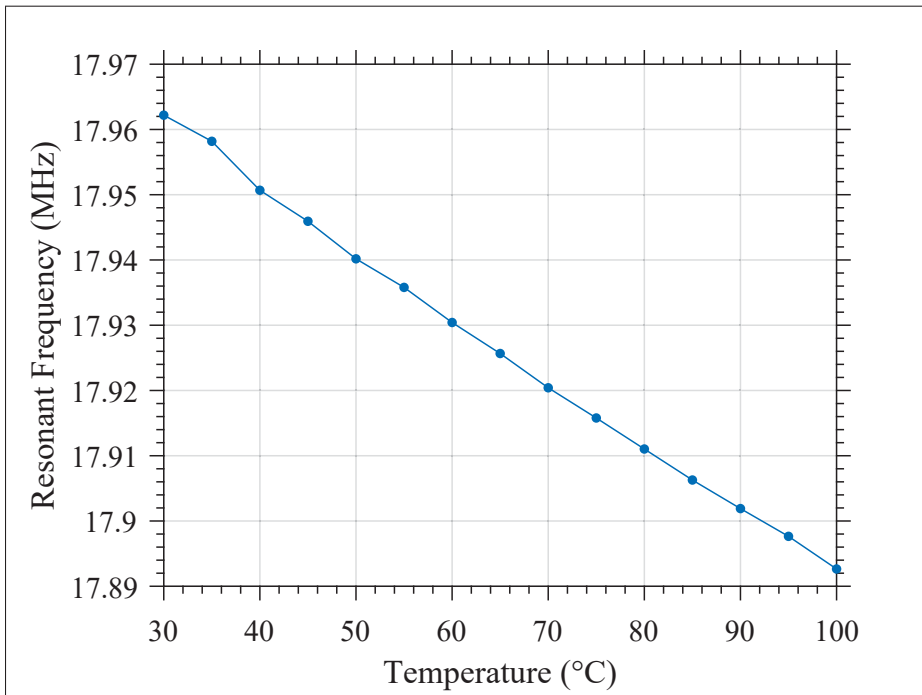
Figure 2.7 Resonant frequency behavior of the LM_0 structure at different temperatures

The impact of changing the resonator orientation from 0 to 15, 30, and 45 degrees can be seen in Table 2.3 for LM_0, LM_15, LM_30 and LM_45, respectively. The resonant frequency decreases from 17.96 MHz for LM_0 to 15.87 MHz for LM_45. The frequency drift over the 70°C range changes from 69.5 kHz for LM_0 to 48.15 kHz for LM_45. The orientation thus results in a 30% improvement in frequency drift for LM_45 over LM_0. Accordingly, the

resulting TCF can be improved by 22% by choosing a < 110 > orientation (LM_45) instead of < 100 > orientation (LM_0) in Lamé mode.

Table 2.3   Resonant frequency, frequency drift and TCF
for different resonator types and orientation

Type	Rotation											
	0°			15°			30°			45°		
	Resonant Frequency (MHz)	Drift (kHz)	TCF (ppm/°C)	Resonant Frequency (MHz)	Drift (kHz)	TCF (ppm/°C)	Resonant Frequency (MHz)	Drift (kHz)	TCF (ppm/°C)	Resonant Frequency (MHz)	Drift (kHz)	TCF (ppm/°C)
LM	17.962	69.5	-55.42	17.521	69.29	-56.40	16.656	63.54	-54.40	15.874	48.15	-43.27
LMO	17.769	64.26	-51.60	17.359	61.53	-50.55	16.329	53.85	-47.18	15.824	47.02	-42.39
LMH	15.463	60.78	-56.05	15.115	58.19	-54.16	13.110	45.22	-47.96	12.815	34.27	-38.15
LMOH	15.329	56.19	-52.02	14.975	51.66	-48.54	13.017	38.31	-42.10	12.615	33.41	-37.83

The SiO_2 deposition effect on the Lamé resonator can be observed for the LMO resonators in Table 2.3. In this design, as noted earlier, a thin layer of SiO_2 (i.e., 0.2 μm) was deposited onto the silicon layer to partially compensate for the resonator TCF. From (2.11), it can be observed that the added layer will reduce the resonant frequency, and the measurement shows a reduction from 17.96 MHz to 17.77 MHz for LM_0 and LMO_0, respectively. Moreover, the temperature behavior enhancement from LM_0 to LMO_0 can be seen to be approximately 8% for the frequency drift and 7% for the TCF. As expected, due to the relatively thin oxide layer deposited, the improvement in TCF is relatively small. This could be improved by using a thicker oxide layer using a custom fabrication process.

The LMH and LMOH resonators include an array of holes in the silicon layer. The experimental results confirm a frequency reduction of approximately 20% in each orientation. For the LMH resonators, the frequency drift changed from 60.78 kHz to 34.27 kHz depending on the angle of the structure, which indicates a 43% reduction. In contrast, the TCF did not change from the base design (LM_0) to LMH_0 since the center frequency reduction occurred by the holes. Nonetheless, the TCF can be improved by more than 11% and up to 51.9% by choosing a 30

or 45 degree rotation in LMH and LMOH devices, respectively. This is because, for larger rotations, the TCF is more significantly impacted when holes are included in the structure (2.15).

Overall, the device rotation can improve the frequency drift over the 70°C range by 0.3%, 8.57%, and 30.7% for the LM_15, LM_30, and LM_45 devices, respectively, compared to the 0-degree angle rotation device (LM_0). Moreover, The measurement results show a 22% improvement in TCF compared to the conventional Lamé resonator(LM_0) for the LM_45 device. The SiO_2 layer deposition method results in a 7.53% improvement in the center frequency drift over the 70°C temperature range and a 6.9% enhancement in TCF compared to the simple Lamé resonator (LM_0). The array of holes has a considerable effect on the resonator properties. A 45-degree rotated Lamé resonator with holes and a top oxide layer (LMOH_45) demonstrates a 31.7% improvement in TCF compared to a conventional Lamé resonator design(LM_0). The frequency drift is enhanced by 51.9% over the 70°C range for the LMOH_45 device compared to the conventional Lamé resonator (LM_0).

In addition, the DC bias voltage is essential for an electrostatic resonator to operate but can cause device breakdown due to arching within the transducer gap.

The resonant frequency of the Lamé resonator as a function of the DC bias voltage is derived in (Tanaka, Kihara, Sánchez-Amores, Montserrat & Esteve, 2007). Figure 2.8 shows the resonant frequency and insertion loss for LM_0 in vacuum (48 $mTorr$) as a function of the bias voltage. The breakdown voltage depends on Paschen's law; therefore, the bias voltage can increase considerably in a low-pressure environment. The use of the bias voltage to compensate for the resonator temperature sensitivity was studied in (Islam *et al.*, 2018). On the other hand, a high bias voltage can increase the transmission power of the resonators. As such, we are able to measure the 3-dB bandwidth and Q-factor from the transmission curve. The measured quality factor for LM_0 in vacuum and 200 V bias voltage is 478,684, as was previously discussed.
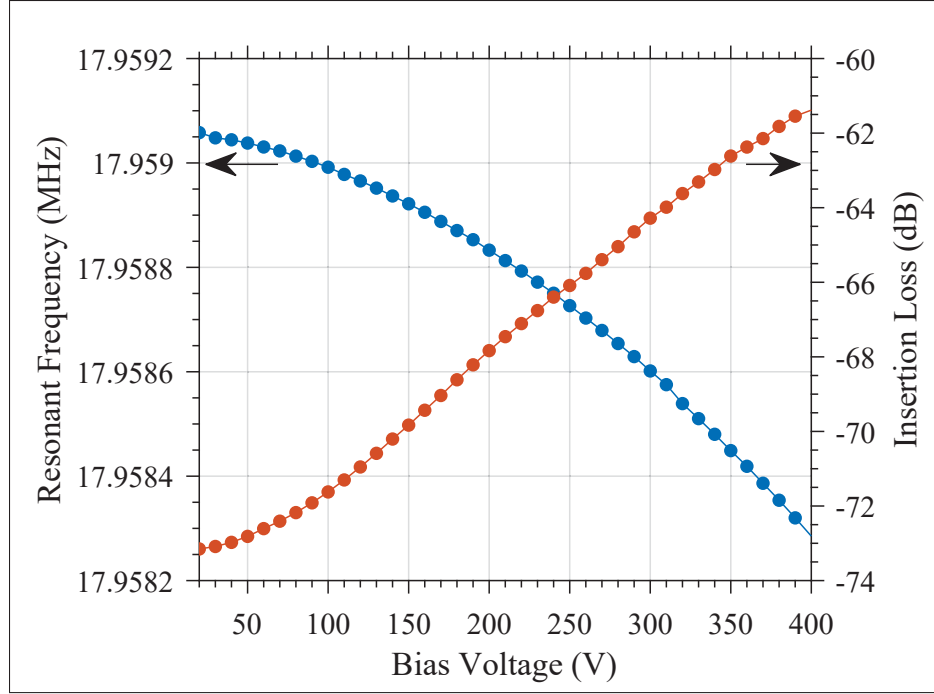
Figure 2.8   The bias voltage effect on the resonant frequency and insertion loss for the LM_0 resonator in vacuum(48 mTorr)

2.4.4   Numerical Modeling Validation

The TCF and resonant frequencies of the Lamé resonators were calculated by extracting material properties for each structure mentioned in section 2.2. The elastic coefficients c_{11}, c_{12}, c_{44}, and derivative of elastic constants over the temperature $\frac{\partial c_{11}}{\partial T}$, $\frac{\partial c_{12}}{\partial T}$, and $\frac{\partial c_{44}}{\partial T}$ for the employed fabrication technology process, i.e., PiezoMUMPs, can be determined by analysing the empirical data obtained in section 2.4.1, along with (2.7) and (2.15).
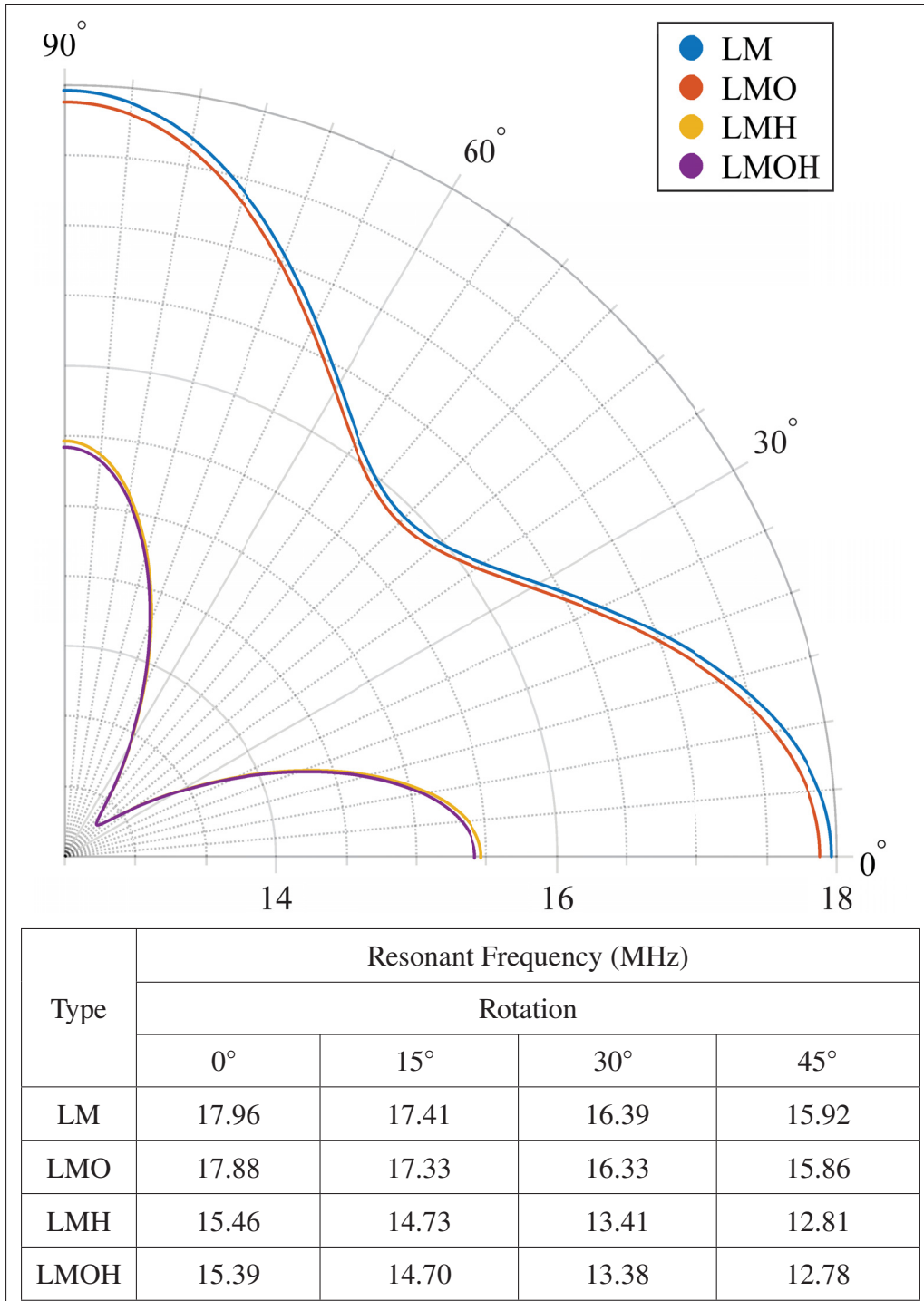
Figure 2.9 Calculated resonant frequency as a function of the resonator orientation, ϕ, for the different Lamé resonator types fabricated. The elastic constants ($c_{11} = 164GPa$, $c_{12} = 39.6GPa$, $c_{44} = 79.2GPa$) have been extracted from (2.6) and the experimental measurements.

	Resonant Frequency (MHz)			
Type	Rotation			
	0°	15°	30°	45°
LM	17.96	17.41	16.39	15.92
LMO	17.88	17.33	16.33	15.86
LMH	15.46	14.73	13.41	12.81
LMOH	15.39	14.70	13.38	12.78

Equation (2.11) determines the resonant frequency when an SiO_2 layer is deposited onto the Lamé resonator structural layer. The resonant frequency of the Lamé resonator with SiO_2 can be computed using the design features stated in section 2.3 and the material properties listed in Table 2.2. The resonant frequency of a single layer of SiO_2, $f^2_{SiO_2}$, mentioned in (2.11) can be calculated by finite element analysis using COMSOL Multiphysics. The simulation shows that the Lamé resonator eigenfrequency with a single layer of SiO_2 is approximately 12.84 MHz.

Moreover, the resonant frequency for the Lamé resonator with holes is given in (2.14), and the filling factor, β for the proposed design, is 0.6.

Figure 2.9 represents the resonant frequency of the different Lamé resonator variants by solving (2.6), (2.11) and (2.14) when ϕ is varied from 0 to $\pi/2$ (i.e., 90 degrees).

Figure 2.10 shows the calculated TCF of the proposed Lamé resonator types as a function of the orientation by using equation (2.15). The silicon stiffness deviation per temperature is assumed linear (Cho, Cha & Sung, 2016; Liu & Source, 2021) within a temperature range from 30°C to 100°C to calculate the TCF. Notably, Figure 2.10 indicates that a 45-degree rotation results in the lowest absolute TCF compared to the other orientations. The numerical analysis shows an absolute TCF increase from 0 to 15 degrees rotation, while the absolute TCF drops by increasing the rotation angle from 15 to 45 degrees.
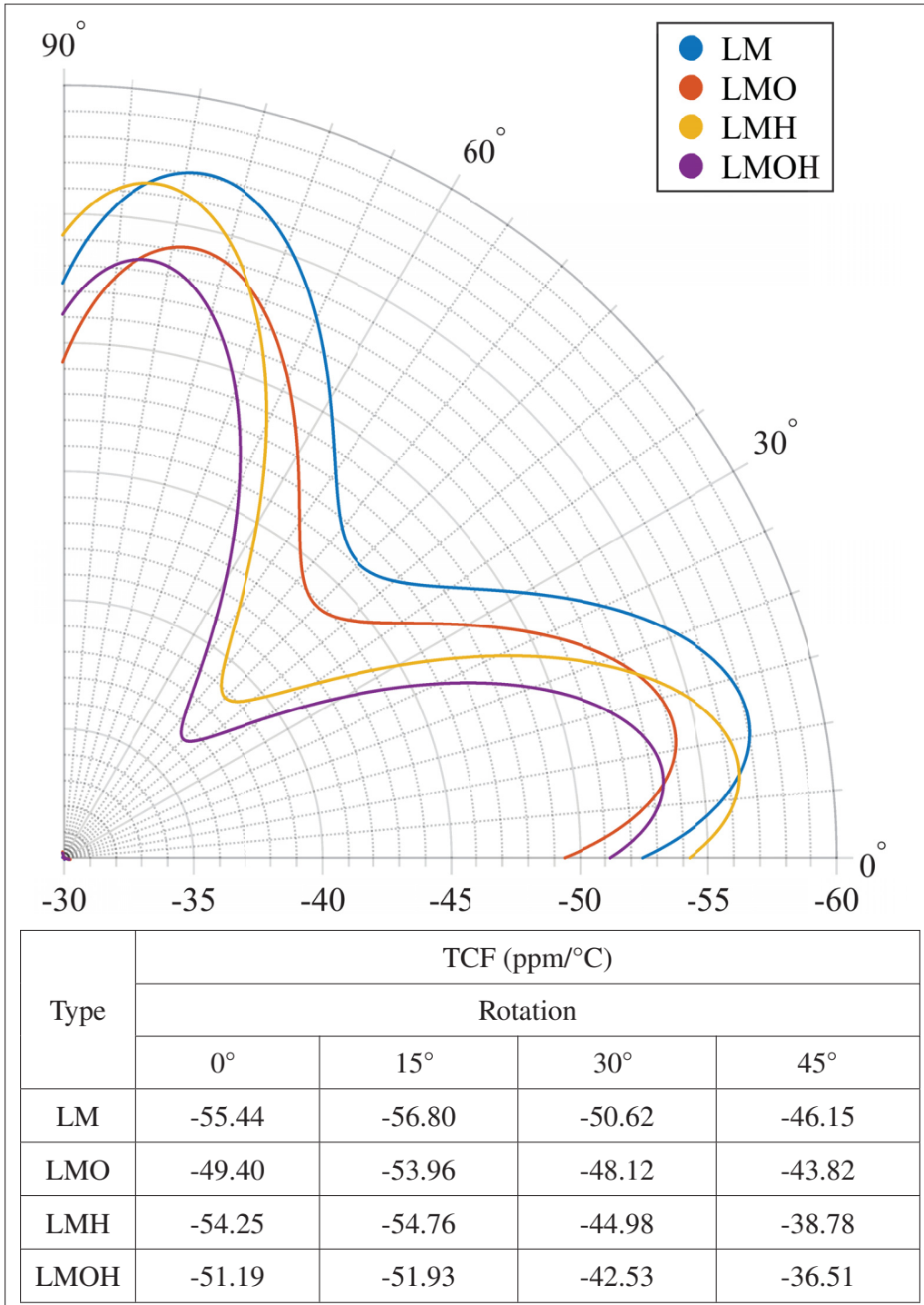
Figure 2.10   TCF as a function of the resonator orientation, ϕ, for the different Lamé resonator types fabricated. The derivatives of the elastic constants ($\frac{\partial c_{11}}{\partial T} = -1.68E7\frac{Pa}{°C}$, $\frac{\partial c_{12}}{\partial T} = -6.30E5\frac{Pa}{°C}$, $\frac{\partial c_{44}}{\partial T} = -6.97E5\frac{Pa}{°C}$) have been extracted from (2.15) and experimental measurements

	TCF (ppm/°C)			
Type	Rotation			
	0°	15°	30°	45°
LM	-55.44	-56.80	-50.62	-46.15
LMO	-49.40	-53.96	-48.12	-43.82
LMH	-54.25	-54.76	-44.98	-38.78
LMOH	-51.19	-51.93	-42.53	-36.51

As can be seen, the estimated resonant frequencies and TCFs by the presented analytical models match reasonably well with the results shown in Table 2.3, indicating that the model presented here is representative of the device behavior over temperature for the different variants studied here.

2.5   Discussion

In this work, an analytical model to predict the performance of the Lamé resonator at different rotation angles and with different structure types was proposed. The validity of this analytical model was experimentally validated. In order to comprehensively demonstrate the versatility of the proposed analytical model, frequency responses and temperature behavior of sixteen Lamé resonators manufactured using a commercial micro-fabrication process, i.e., PiezoMUMPS, were surveyed.

It is shown that the SiO_2 deposited onto the Lamé resonator can reduce the TCF. It can be analytically estimated using (2.12) that in order to achieve a zero TCF resonator, a 4 μm thick layer of SiO_2 is required. While such a thick layer of SiO_2 minimizes the frequency shift, its implementation would require modification of the PiezoMUMPS process. With the reduced thickness available in PiezoMUMPS (i.e., 0.2 μm), this method improves the TCF by 7% at a zero-degree device rotation.

It is also shown that using an array of holes within the structure can reduce the frequency shift caused by temperature. However, the thermoelastic losses diminish the resonator quality factor (Luschi *et al.*, 2017). The hole sizes and their distribution considerably contribute to TCF compensation, which can be seen from (2.15). This effect allows a reduction of the TCF when combined with device rotation. In the LMH_45 design, the filling factor specified in (2.13) is chosen as 0.6, resulting in a 31% improvement in TCF compared to a typical LM_0 device.

Indeed, the resonant behavior and transmission loss are important metrics. The designed Lamé resonators in this study have a high-quality factor and straightforward fabrication procedure.

However, a large gap size (i.e., 2 um) makes the transmission loss high due to the low electrostatic coupling achieved.

The PiezoMUMPS technology elastic coefficients, c_{11}, c_{12}, c_{44}, and derivatives of elastic constants over temperature $\frac{\partial c_{11}}{\partial T}$, $\frac{\partial c_{12}}{\partial T}$, and $\frac{\partial c_{44}}{\partial T}$ which are used in this study, are calculated by analysing the measured data. The proposed analytical model can accurately predict the resonant frequency and TCF with respect to design variant and silicon orientation. A comparison between the results obtained from the analytical model and experimental measurement shows an average error of 3%.

The resonant frequency is reduced by increasing the rotation angle from 0 to 45 degrees, and then increases at rotation angles above 45 degrees. As for the TCF, it increases at up to approximately 15 degrees of rotation, and then reduces for the larger rotation angles, showing an optimum at 45 degrees. Accordingly, it is demonstrated that the analytically estimated TCF can reach -36.5 ppm/C for the LMOH_45, where the oxide layer and holes have a considerable effect on the resonator performance over temperature. This compares well with the measurement of -37.83 ppm/C for this device.

2.6   Conclusion

This work provided a comprehensive overview of passive temperature compensation techniques for Lamé resonators fabricated in PiezoMUMPs technology. An analytical model to predict the resonant frequency and TCF for different structures of the Lamé resonators was proposed. The required elastic coefficients for the proposed analytic model were measured experimentally.

These results provide guidance on MEMS Lamé resonators with improved temperature stability and give modeling insight into the different temperature compensation mechanisms studied. The model presented can allow for predicting the resonant frequency and TCF behavior using the different compensation techniques presented.

Acknowledgement

Author Contributions

For this article, A. Kolahdouz and F. Nabki developed the idea. A. Kolahdouz performed the design, simulation, and layout preparation of the MEMS resonators. A. Kolahdouz performed the measurements of the prototypes. A. Kolahdouz and S. Nabavi analyzed the results. A. Kolahdouz prepared the manuscript, and S. Nabavi and F. Nabki edited it. This work was carried out under the supervision of F. Nabki.

CHAPTER 3

LAMÉ RESONATOR INTEGRATED WITH CHEVRON-SHAPED THERMAL ACTUATORS TO IMPROVE MOTIONAL RESISTANCE AND TEMPERATURE STABILITY

Amir-Reza Kolahdouz-Moghaddam[1] , Seyedfakhreddin Nabavi[1] , Frederic Nabki[1]

[1] Département de Génie Électrique, École de Technologie Supérieure,
1100 Rue Notre-Dame Ouest, Montréal, Québec, H3C 1K3, Canada

Abstract: This paper presents a capacitive bulk mode resonator operating in Lamé mode, where the motional resistance and temperature stability are enhanced by implementing a chevron-shaped thermal actuator to reduce its transducer gaps. The chevrons are heated using micro-heaters that are integrated on the actuator. The device is fabricated in the PiezoMUMPS standard microfabrication process by MEMSCAP. The measured resonant frequency for the fabricated device was observed to be 17.9 MHz. It has been experimentally shown that the transducer gap can be reduced from 2.5 μm to 0.5 μm by applying a heater voltage of 2.7 V at atmospheric pressure. In the proposed resonator, the transmission loss can be reduced by 8.54 dB when the actuators are biased at 1.8 V in vacuum, as opposed to when the actuator is off. Under these conditions, the thermal actuators each consume 39 mA. In addition, the implemented thermal actuators can function as integrated heaters that increase the temperature of the suspended square structure to compensate for ambient temperature variations. In this case, applying a voltage of 1.8 V in vacuum reduces the resonant frequency from 17.95 MHz to 17.91 MHz, while applying a voltage of 2.6 V at atmospheric pressure reduces the resonant frequency from 17.97 MHz to 17.86 MHz.

Keywords: MEMS resonators, bulk micromachining, gap closing, movable electrode, motional resistance, temperature-compensated resonator

3.1   Introduction

Microelectromechanical systems (MEMS) oscillators have been demonstrated to be a viable replacement for standard quartz crystals in timing and telecommunication applications (Abdolvand *et al.*, 2016; Marrison, 1948). Due to their excellent precision (Yang, Hamelin & Ayazi, 2020), compact size (Nabki, Ahmad, Allidina & El-Gamal, 2008), and ability to be integrated tightly with CMOS electronics (Kubena, Stratton, Nguyen, Kirby, Chang, Joyce, Yong, Garstecki, Cross & Seman, 2017), they have become a prominent alternative to quartz-based oscillators. Bulk mode resonators are widely used for timing applications thanks to their high quality factor (Q) (Elsayed & Nabki, 2019) ,and shock resistance (Arft, Lu & Parvereshi, 2016) as a result of their high structural stiffness (de Laat, Pérez Garza, Herder & Ghatkesar, 2016; Wu, Xu, Xiong & Wang, 2013). This characteristic enhances device performance at the expense of the increased actuation forces required and the small generated signals. The lateral transducer gap in the mechanical structure of MEMS resonators plays a critical role in both actuation and sensing behaviors of the resonators (Yuan Xie, Sheng-Shian Li, Yu-Wei Lin, Zeying Ren & Nguyen, 2008; Houri Johari & Farrokh Ayazi, 2007). It is worth pointing out that the transducer gap, in the majority of cases, cannot be readily minimized due to manufacturing constraints (Elsayed & Nabki, 2017c). This limits the transduction characteristics of these devices, and thus their motional resistance is relatively high.

Several approaches to increase the transduction of MEMS resonators, and reduce their motional resistance, have been explored, including coupling multiple resonators to increase the transduction between resonator ports (Shalaby, Abdelmoneum & Saitou, 2009). In (Elsayed & Nabki, 2017a; Xereas & Chodavarapu, 2015), it was demonstrated that increasing the resonator bias voltage is a viable method to improve the transduction while the resonator has to operate close to its electrostatic breakdown voltage. Comb-shaped anchors can improve signal transduction between resonator ports (Elsayed, Nabki & El-Gamal, 2013b,a), whereas the effective mass of the resonator is increased, resulting in an undesirable frequency reduction and a lower Q. Integrating piezoelectric materials into manufacturing techniques has created a new resonator signal transduction enhancement paradigm. Utilizing piezoelectric actuators and sensing electrodes in

bulk mode resonators has been demonstrated to be a practical approach for enhancing resonator performance (Beaulieu, 2019; Elsayed, Cicek, Nabki & El-Gamal, 2016). In (Hung & Nguyen, 2011), an electrostatic resonator was paired with a 50 MHz piezoelectric actuator to achieve a transduction of up to -40 dB. However, piezoelectric materials have a tendency to increase thermoelastic damping in the resonating structure and limit its maximum achievable Q.

It was demonstrated in (Jiang, Bao, Du & Deng, 2013) that the transducer gap can be reduced to 50 nm by employing fixed stoppers using a sophisticated anchor topology. It is worth mentioning that utilizing an electrostatic actuation mechanism to close the transducer gap is a highly effective technique to circumvent manufacturing constraints (Van Toan & Ono, 2014). For instance, the air gap in (Elsayed & Nabki, 2019) was reduced to 200 nm, the smallest possible fabrication grid, and an insertion loss of 33 dB was observed at a drive voltage of 55 V.

Another essential factor in commercializing MEMS resonators is the resonant frequency drift over the changes in ambient temperature (Pandit, Mustafazade, Sobreviela, Zhao, Zou & Seshia, 2021). Without compensation, the thermally-induced elastic properties variations of silicon limit its applicability for high-precision frequency timing applications, such as oscillators used in telecommunications and timing applications. Thus far, numerous active and passive strategies have been developed to address this issue. Passive compensatory approaches such as composite material addition with opposing temperature coefficient of frequency (TCF) (Melamud *et al.*, 2009; D. M. Chen *et al.*, 2013), heavy silicon doping Samarao *et al.* (2010), and shifting the silicon orientation (Zhu & Lee, 2014; Jaakkola *et al.*, 2012) have been utilized to minimize the silicon temperature dependency. As a matter of fact, these methods are unable to achieve zero-TCF in MEMS resonators and require custom fabrication processes that increase the resonator device implementation cost. As a result, active approaches that consume more power (Comenencia Ortiz, Kwon, Rodriguez, Chen, Vukasin, Heinz, Shin & Kenny, 2020b), and require complex control circuits (Mahmoud, Mukherjee & Piazza, 2020), and require a significant area have become prevalent (Kwon, Vukasin, Bousse & Kenny, 2020). These active methods, however, increase the power budget and overall cost of MEMS resonator-based oscillators.

It is worth mentioning that the integration of micro-ovens with silicon-based resonators has also been employed to raise the resonator's temperature above ambient and stabilize its frequency. In (Tazzoli, Rinaldi & Piazza, 2011), it is demonstrated that an aluminum nitride (AlN) based MEMS resonator with a bottom serpentine heater can have an increased temperature of 100°C, rendering it resilient to ambient temperature changes. However, it cannot be ignored that, generally, heaters consume a considerable amount of power. For example, in (Pei, Sun, Yang, Ye, Zhong, Yu & Li, 2020), a heater with a power consumption of 108 mW is implemented to fully compensate for the ambient temperature. This excessive power usage is used only to stabilize the resonator temperature without improving the resonator motional resistance mechanism.

Accordingly, this work proposes a capacitive bulk mode resonator operating in Lamé mode, where both the motional resistance and the temperature stability are improved. This is done by utilizing a thermal actuation mechanism to reduce the transducer gaps. Thermal actuation allows the actuator to operate at low voltages, unlike conventional electrostatic gap closers, at the expense of power consumption increment. The proximity of the heater to the resonator also enables to use of the dissipated heat to increase the resonator's temperature relative to the ambient temperature and provide temperature stability. Notably, the proposed resonator can be manufactured using standard MEMS fabrication techniques, such as PiezoMUMPs from MEMSCAP used in this work. Thus, the proposed device uses thermal power consumption to both reduce motional resistance and increase the device's temperature to provide a mechanism to enhance its temperature stability. This can simplify the oscillator circuit that can then be designed to operate with the resonator device, both with regards to the sustaining amplifier gain required and the temperature monitoring and frequency control circuitry.

The rest of the paper is organized as follows; Section 3.2 presents the micro-fabrication process and design parameters. Section 3.3 contains the experimental results for the proposed resonator, and Section 3.4 discusses the resonator performance and compares the proposed approach to existing designs. Section 3.5 summarises the contributions of this work.

3.2 Design and Micro-fabrication Process

3.2.1 Design

The micrograph of the Lamé resonator integrated with thermal actuators is depicted in figure 3.1, along with zoomed sections of the structure shown in four insets. As shown in this figure, the suspended square structure (i.e., the resonant mass) with 230 μm length and 10 μm thickness is connected to pads located at the edge of the device by four 27 μm anchors. The square resonator is surrounded by four chevron-shaped thermal actuators to reduce the transducer gap, whereas the surface of the actuators houses the electrical traces for electrostatically actuating the resonator. Each chevron-shaped thermal actuator contains an electrostatic transducer structure, a heater on the top metal layer (i.e., PADMETAL), and two anchors to pass the electrical connection and sustain mechanical stability on each side. As shown in figure 3.1b for one side of the device, each electrostatic transducer structure includes several parts. First, the structure includes mechanical stoppers intended to maintain mechanical isolation between the moving chevron and the suspended square to ensure a reliable resonator. These stoppers prevent the resonator from short-circuiting due to a complete closure of the transducer gap, which would short-circuit the device and potentially destroy it. These stoppers could be removed to further reduce the transducer gap, but in this work, reliability to vibrations post gap-closing was a design requirement preventing this removal. Second, transducer electrodes are present around the suspended square to drive the resonator electrostatically. Third, bond pads are present to connect the external circuitry with the transducer electrodes via the silicon structure. Finally, the heaters are fabricated on the PADMETAL layer and are electrically isolated from the structural silicon layer by a 200 nm thick oxide layer between the layers. In order to apply voltage to the heaters, two pads on each chevron are implemented.

The initial distance post-fabrication between the sensing electrode and the suspended square, namely the electrostatic transducer gap, is 2.5 μm. As will be discussed in more detail in the following sections, the stopper design results in an end gap minimal distance of about 0.5 μm when the thermal actuators are fully driven.

Figure 3.1c, d, and e, respectively, show the close-ups of the electrostatic gap and the resonator anchor, the chevron and bond pads, and the stoppers and transducer electrode.
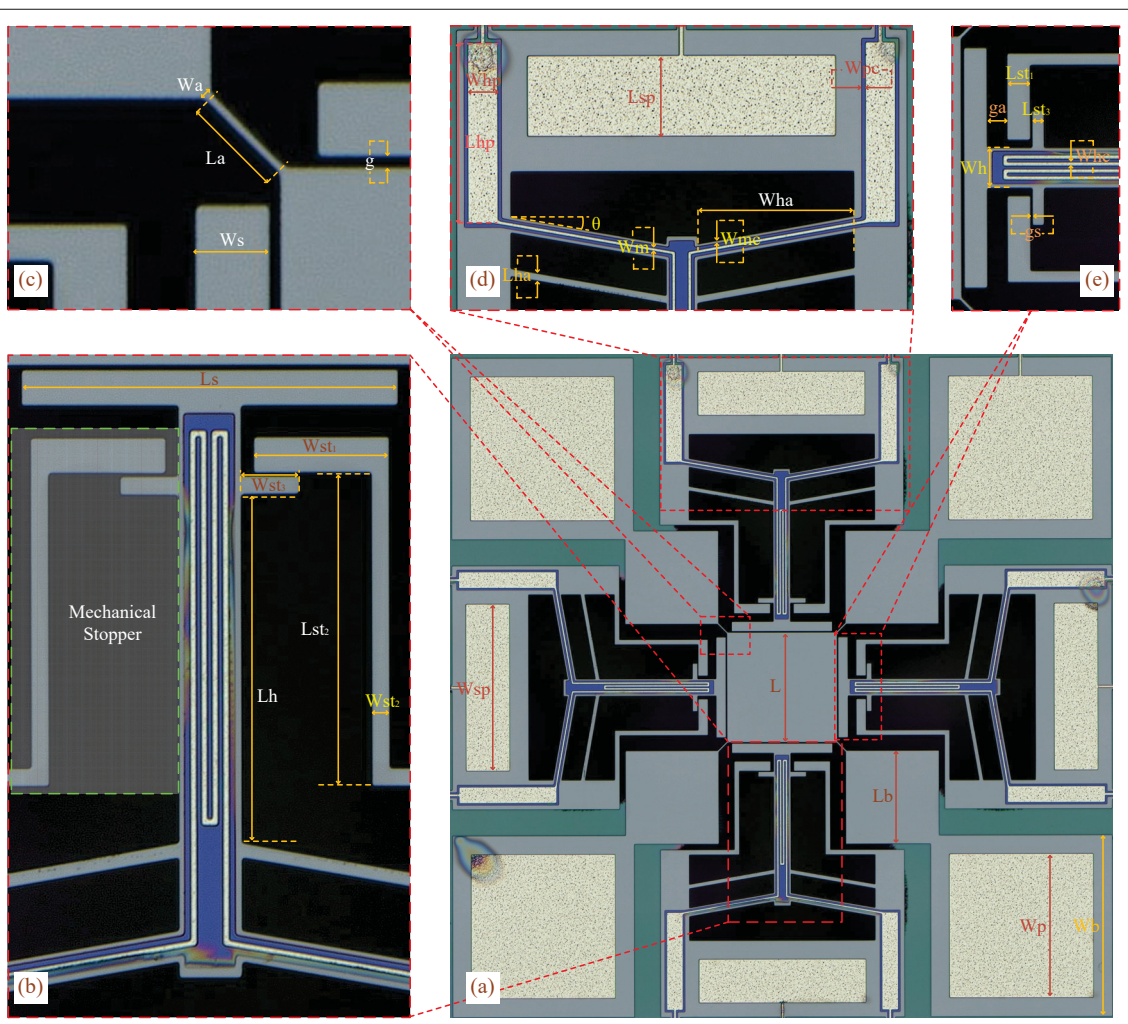
Figure 3.1   Micrograph of the proposed Lamé resonator fabricated with PiezoMUMPs microfabrication technology. (**a**) The Lamé resonator is comprised of a suspended square located at the center of the device with four anchors and four chevrons. Insets show: (**b**) a chevron, including the stopper, transducer electrode and the heater; (**c**) the electrostatic gap and the resonator anchor; (d) the chevron with anchors and the bond pads; and (**e**) the stoppers and transducer electrode structure

Table 3.1   Geometric parameters of the proposed design

Parameters	Symbol	Value (μm)
Resonator length	L	230
Transducer electrode length	Ls	210
Transducer electrode width	Ws	20
Transducer bond pad length	Lsp	90
Transducer bond pad width	Wsp	348
DC bias bond pad width	Wp	300
DC bias bond pad width	Wb	380
Anchor length	La	5
Anchor width	Wa	3
Gap width	g	2.5
Stopper to transducer electrode pad distance	ga	17.5
Stopper gap	gs	2
Anchor extension length	Lb	195
Heater length	Lh	195
Stopper length	$Lst1$	20
Stopper anchor length	$Lst2$	175
Transducer electrode stopper length	$Lst3$	12
Stopper width	$Wst1$	75.5
Stopper anchor width	$Wst2$	10
Transducer electrode stopper width	$Wst3$	32.5
Heater Width	Wh	35
Heater width	Whc	3
Heater anchor width	Wha	176.5
Heater bond pad width	Whp	33
Heater bond pad oxide clearance	Wpc	348
Heater anchor silicon to oxide clearance	Wmc	3
Heater anchor wire width	Wm	3
Heater bond pad length	Lhp	203
Transducer anchor support length	Lha	8
Heater anchor angle	θ	10

Table 3.1 summarises the geometric dimensions of the proposed Lamé resonator design represented in figure 3.1.

3.2.2   Micro-fabrication process

The Lamé resonator integrated with the thermal actuators was fabricated by the standard microfabrication process, PiezoMUMPs, provided via MEMSCAP. Figure 3.2 shows the fabrication process for the Lamé resonator integrated with the thermal actuators. In this fabrication process, a 150 mm diameter silicon-on-insulator wafer with a (100) orientation and 10 μm doped silicon is used. Over the doped silicon, a layer of oxide (PADOXIDE) with a thickness of 0.2 μm is deposited and patterned. The last layer is aluminum (PADMETAL) with a thickness of 1 μm, which can be used for both electrical connections and wire bonding purposes (Figure 3.2a). Notably, the PADOXIDE layer ensures the electrical isolation between the SOI and PADMETAL Layer (Figure 3.2b). The silicon device layer is then patterned lithographically using a mask illustrated in Fig. 3.2c (SOI). On the front side of the wafer, a polyimide film is deposited, which serves to protect the devices during the trench etching. This final etch occurs from the bottom of the substrate using the layer known as TRENCH (Figure 3.2d). The buried oxide is then removed, and the devices are released. Table 3.2 contains information about the materials and the layers' thicknesses utilized in the process. It should be noted that the minimum feature size for the silicon device layer is 2 μm, therefore, the minimum transducer gap cannot be reduced to be smaller than without additional post-fabrication actuation. In this work, it was designed to be 2.5 μm prior to the thermal actuation.
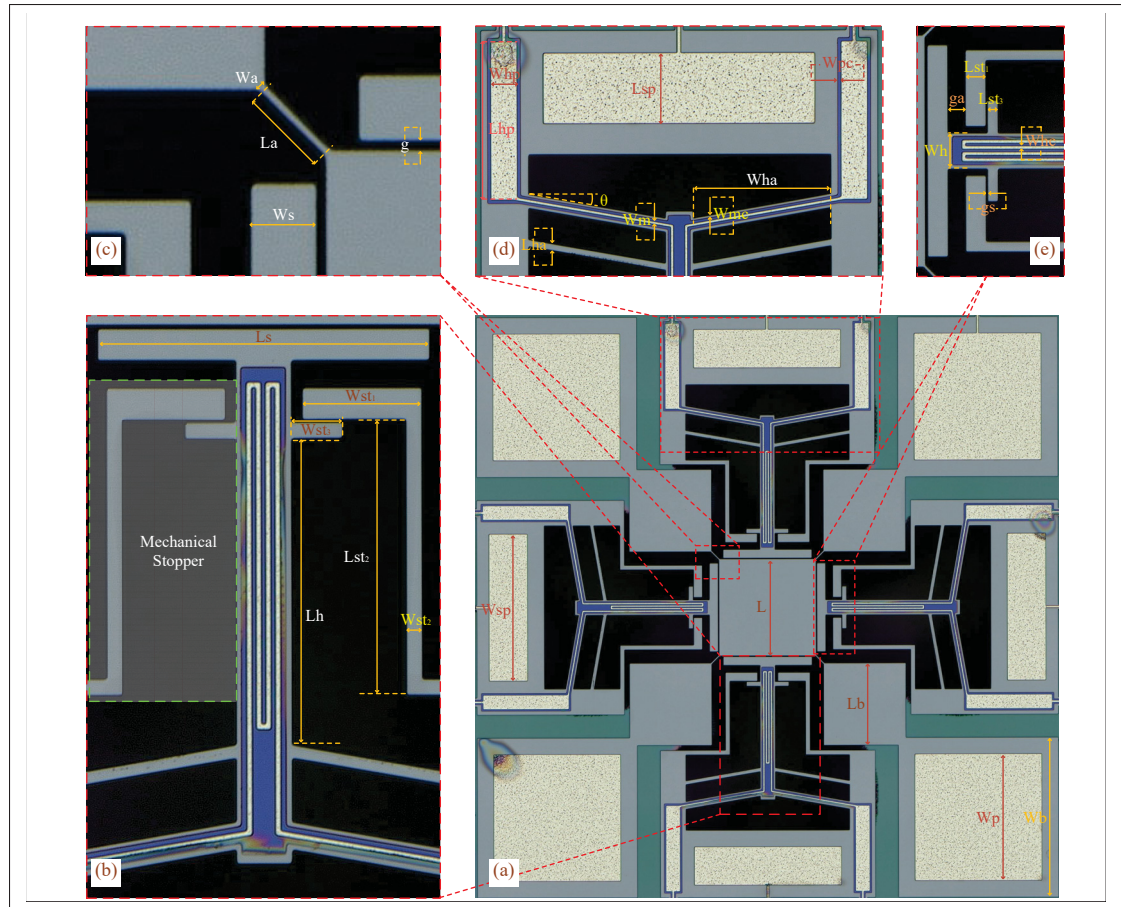
Figure 3.2   Simplified 3D and top views of the PiezoMUMPs process flow used
for prototyping the proposed Lamé resonator

Table 3.2   Characteristics of the PiezoMUMPs process
layers

	Thickness (μm)	Error (μm)	Density ($\frac{kg}{m^3}$)	Layer Name
Substrate	400	±5	2320	TRENCH
Silicon	10	±1	2320	SOI
SiO$_2$	0.2	±0.01	2200	PADOXIDE
Aluminium	1	±0.05	2710	PADMETAL

3.3 Experimental Results

3.3.1 Experimental Test Setup

The frequency response of the Lamé resonator described in Section 2.3 was measured when different voltages were applied to the heater across the chevron-shaped thermal actuators. In this regard, the frequency response of the prototyped Lamé resonator was measured using a Keysight model E5061 Vector Network Analyzer (VNA) shown in figure 3.3. The VNA ports were connected to a pair of DC blockers to prevent damage in the event of a short circuit between the transducer electrodes and DC bias, as well as the advent of electrical arcs due to the electrostatic breakdown in the vicinity of the gap. Both VNA ports were equipped with a balun (CX2074NL) since the single-ended signal has to be converted to a differential signal with a 180-degree phase shift to drive the resonator on two adjacent sides of the square structure. A Keithley model 2260B high voltage power supply was utilized to generate the DC bias voltage (V_{bias}) required for the electrostatic actuation of the resonator. A protection resistor was placed between the power supply and the DC bias port to reduce current flow in the event of device failure that would otherwise result in a large current draw. The heaters over the chevron-shaped thermal actuators were driven by applying a DC voltage (V_{heater}) using a power supply from Tektronix model PWS4323. The transducer gap was measured using the Olympus Lext5100 3D laser scanning microscope, and the heater temperature was determined using the FLIR thermal camera (ETS320).
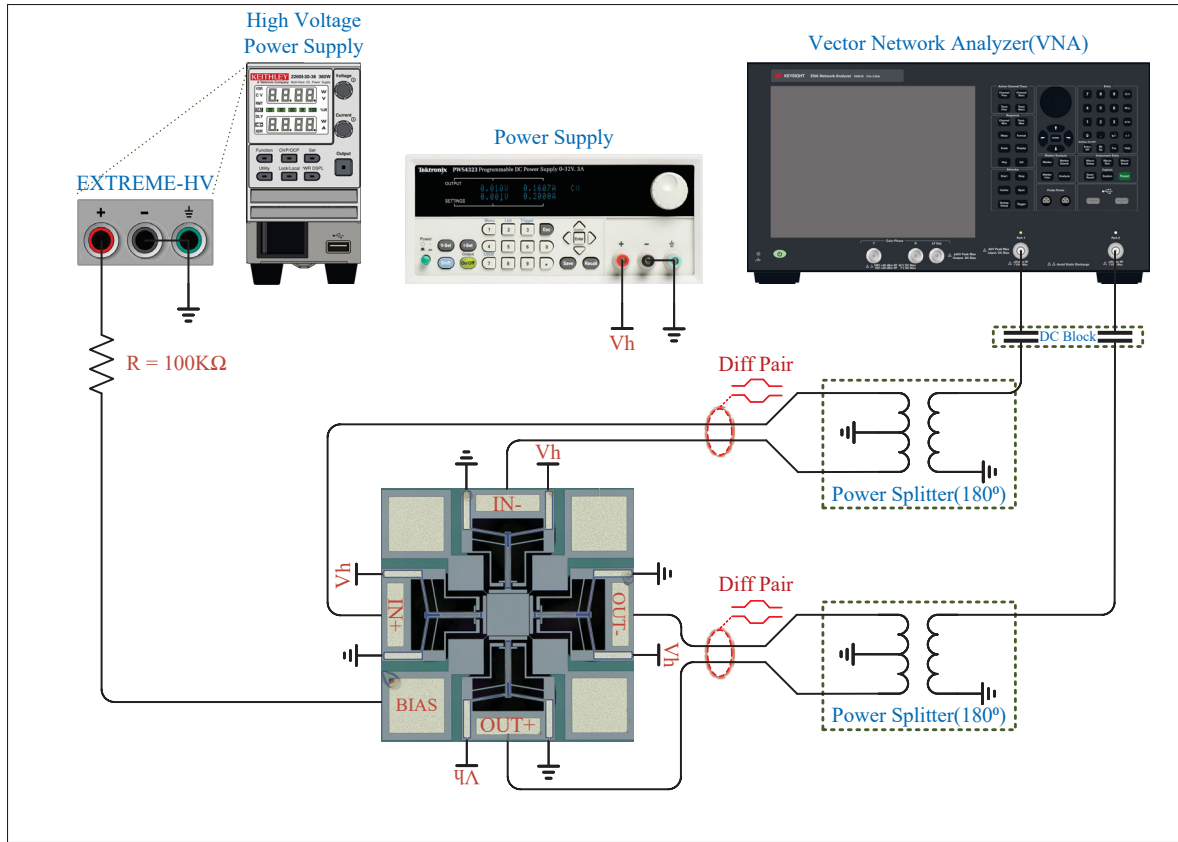
Figure 3.3   The differential test setup configuration used to measure the resonant frequency of the device and apply the heater voltage to the actuators

3.3.2   Characterization

The proposed resonator was tested with a differential setup using two power splitters with a 180-degree phase shift to improve performance and reduce the feedthrough effect caused by the wirebonding and PCB traces. The distance between the transducer electrode and the suspended square structure is reduced as the voltage applied to the heaters is increased.

A finite element modeling (FEM) software package (COMSOL Multiphysics Version 6.0) was used to predict the performance of the resonator and its actuators. The proposed resonator was modeled with isotropic silicon for the structural layer. The silicon elastic parameters c_{11}, c_{12}, and c_{44} were determined to be 164 GPa, 39.6 GPa, and 79.2 GPa, respectively, whereas

table 2.2 provides the material densities. An accurate model for the Lamé resonator, with its chevron-shaped thermal actuators, was developed by combining the *Solid Mechanics*, *Heat Transfer*, *Radiation*, and *Electric Currents* toolboxes.

The heater voltage allows current to flow through the PADMETAL heater laying on top of the chevron and increases its temperature through joule heating. The current flowing through the heaters is measured to calculate the heater power consumption and determine heater resistivity as a function of temperature. Figure 3.4 depicts the simulated and measured heater current produced by the power supply as a function of V_{heater} applied to the four chevron heaters connected in parallel. In addition, as the heater resistivity is a function of temperature, i.e., as the voltage applied to the heaters is increased, the heaters' resistance increases due to the increase of temperature in the PADMETAL layer, as illustrated in figure 3.5.
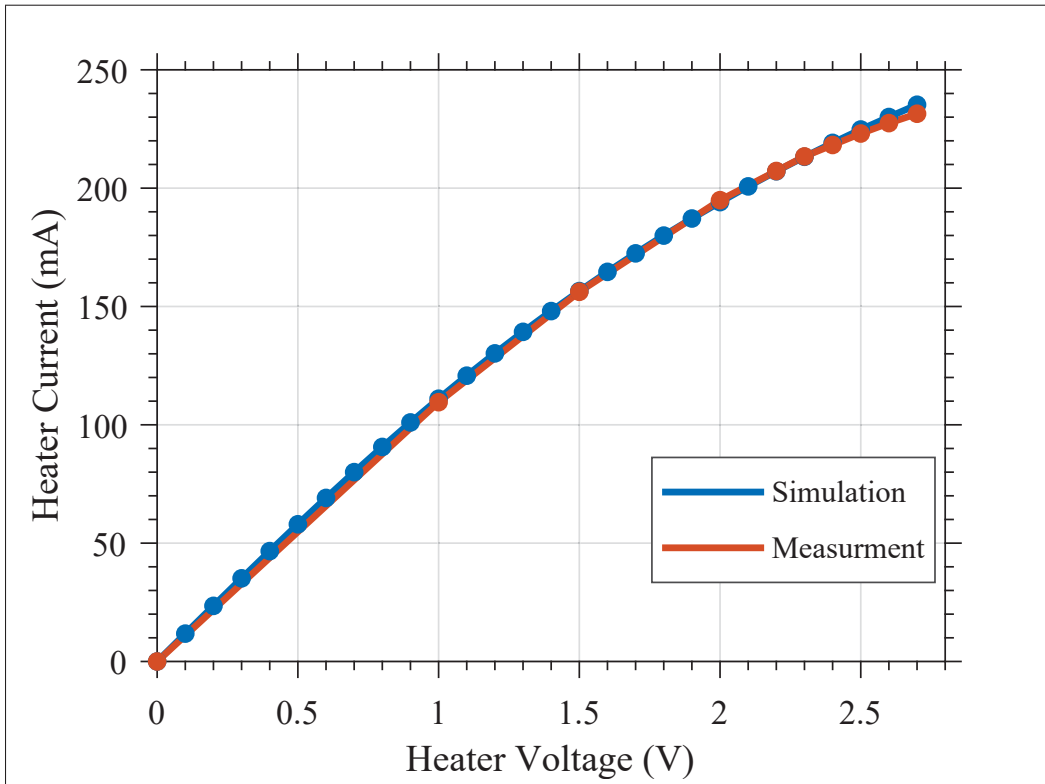
Figure 3.4   Simulated and measured current of the four parallel chevron heaters vs the applied heater voltage in atmospheric pressure
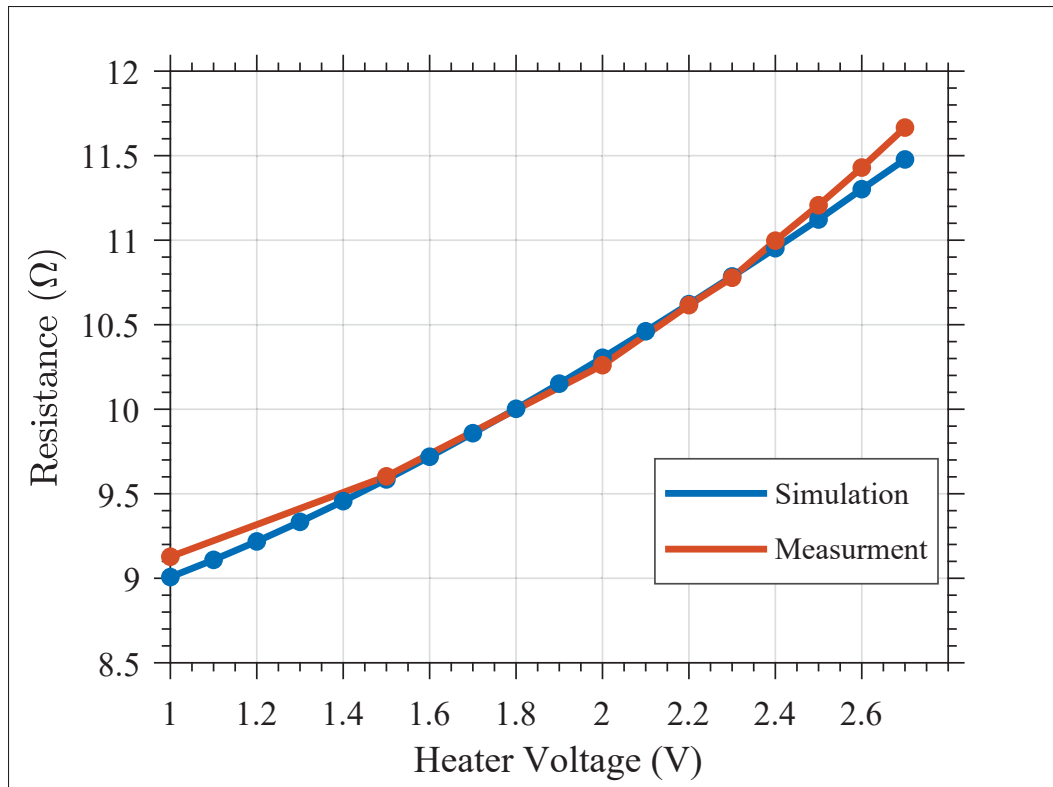
Figure 3.5   Simulated and measured resistance of the four parallel chevron
heaters vs the applied heater voltage in atmospheric pressure

The chevron actuator behaves like a multi-layer material; hence, the temperature increment in the PADMETAL layer is transferred to the silicon layer beneath the heater and raises the chevron's temperature. The simulated and measured temperature of the chevron heater is shown in figure 3.6. In figure 3.7, the simulated and measured effect of this temperature increase on the transducer gap size is demonstrated. With reference to this figure, the electrostatic gap reduces from 2.5 μm to 0.5 μm due to thermal expansion of the chevron when the heater heats up from room temperature, i.e., 25 °C to 610 °C.
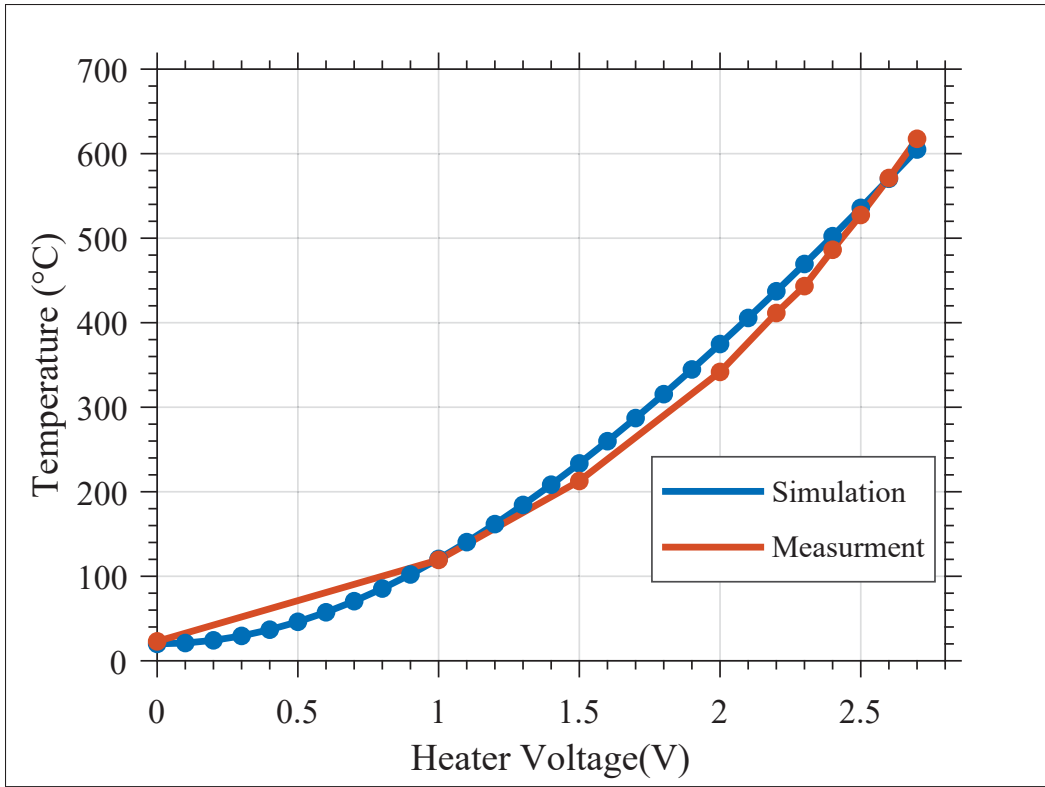
Figure 3.6   Simulated and measured resonator heater temperature vs the
applied heater voltage in atmospheric pressure

The Lamé resonator's resonant frequency is measured both in atmospheric pressure and vacuum (i.e., 40 mTorr) with the VNA. In figure 3.8, when the $V_{heater} = 0$ V, the resonant frequency in atmospheric pressure with $V_{bias} = 200$ V is 17.974 MHz. Due to the transfer of the generated heat by the heaters to the suspended square, the negative temperature coefficient of frequency (TCF) of silicon, and the increased spring softening due to the reduced transducer gap, the resonant frequency decreases as the heater voltage increases. When the heater voltage is varied from 0 V to 2.6 V, a total shift of 118.2 kHz is observed. The FLIR thermal camera shows an approximate suspended square temperature of 143 °C at a heater voltage of 2.6 V. In addition, FEM modeling revealed that the resonant frequency drift is linear as the resonator temperature increases, and the results indicated a frequency shift of around 1 kHz/°C. Notably, FEM modeling demonstrates that the resonant frequency drift caused by the increased spring softening resulting from the

lowered transducer gap is less than 2 kHz when the electrostatic gap is reduced to 0.5 μm, and findings in Elsayed & Nabki (2019) validate the FEM simulation results for the Lamé resonator.

At the 40 mTorr vacuum level, the resonator resonant frequency is 17.95 MHz when $V_{heater} = 0$ V, as shown in figure 3.8. Furthermore, due to the lack of air molecules, heat transfer will be limited to radiation, and free convection will be eliminated Logan (2022). As a result, the resonator temperature is lower in comparison to atmospheric pressure, and the resonator experiences a frequency shift of 38.7 kHz at $V_{bias} = 200$ V and $V_{heater} = 1.8$ V. The impact of the increased spring softening as the transducer gap reduces remains, however, and represents a larger portion of the drift observed in vacuum. The FEM simulation reveals that the resonator temperature is higher than the ambient (i.e., 23 °C) by 43 °C when $V_{heater} = 1.8$ V, yielding an extrapolated temperature of 66 °C. Unfortunately, since the device is an enclosed vacuum system, it is impossible to determine the resonator's absolute temperature using the FLIR thermal camera.
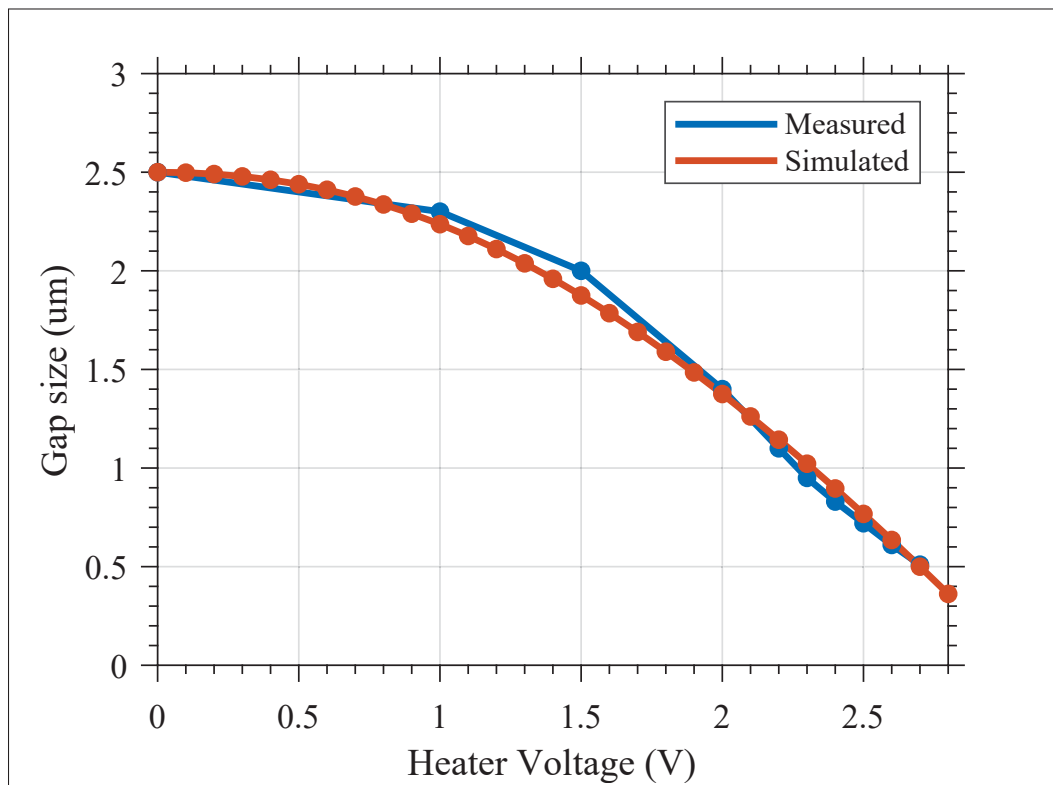
Figure 3.7   Simulated and measured resonator transducer gap size vs the applied heater voltage in atmospheric pressure
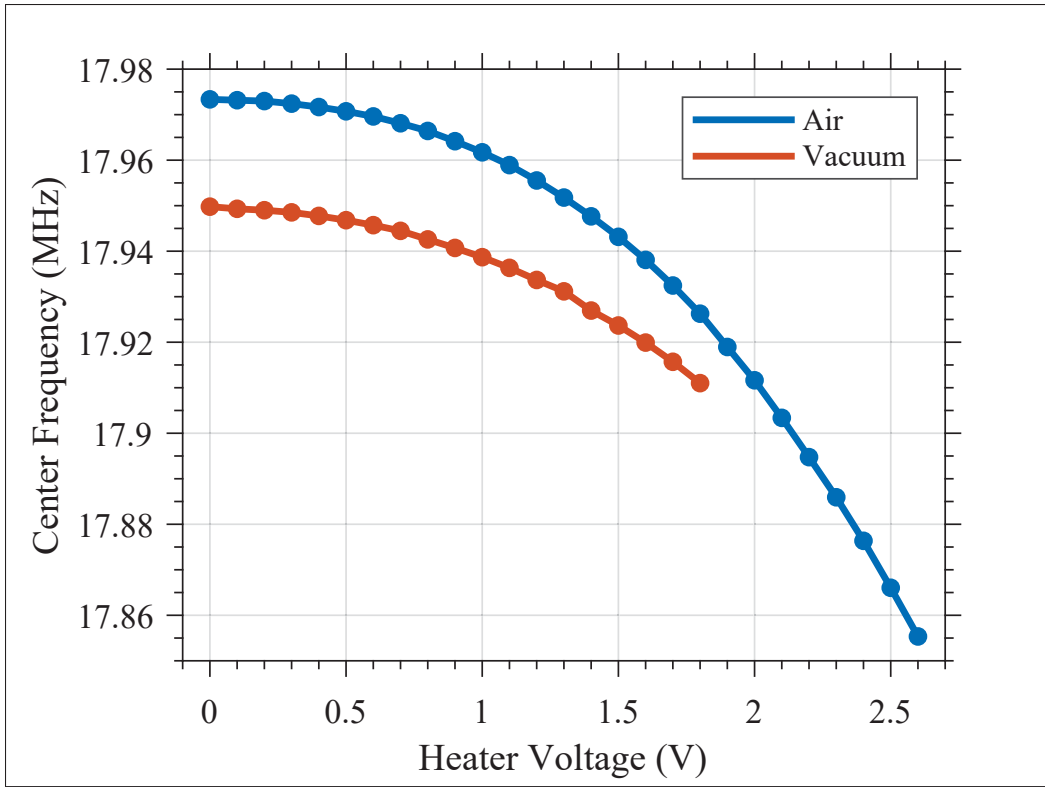
Figure 3.8   Measured device resonant frequency in atmospheric pressure
and vacuum vs the applied heater voltage

Figure 3.9 depicts the resonator transmission amplitude (i.e., S_{21}) when the heater voltage varies from 0 V to 2.6 V in atmospheric pressure. As a result of the effects previously discussed, the resonant frequency shifts to lower frequencies as the heater temperature rises and the transducer gap size reduces. Moreover, the reduced transducer gap causes the transmission peak-to-floor to increase. In atmospheric pressure, when V_{heater} = 2.6 V, the peak-to-floor ratio of the signal increases to 6 dB compared to 3 dB in the absence of heater, V_{heater} = 0. Moreover, the peak transmission magnitude increases by 1.9 dB (1.24×).
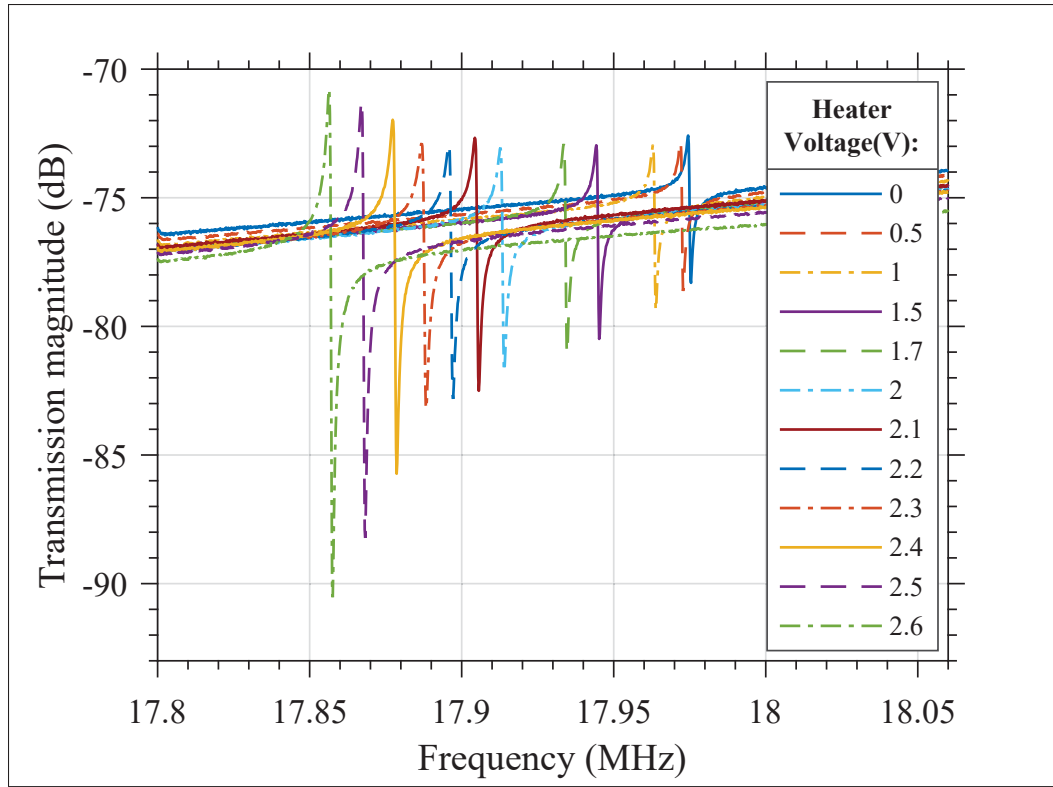
Figure 3.9   Measured resonator frequency response in atmospheric pressure
vs different applied heater voltages

Under vacuum level conditions (i.e., 40 mTorr) to eliminate air damping and improve its quality factor and transmission magnitude (i.e. motional resistance), the resonant behavior of the proposed Lamé resonator was measured and is shown in figure 3.10, as the heater voltage varies from 0 V to 1.8 V. According to this figure, the peak-to-floor increases significantly compared to the atmospheric pressure condition; however, due to the lack of free convection, the heater can partially heat up the suspended square structure, and thus the frequency shift due to temperature is reduced in comparison to the atmospheric pressure case. The Lamé resonator in vacuum expresses a 10 dB peak-to-floor transmission magnitude in the initial state, which is 7 dB higher than the resonator in atmospheric pressure with similar parameters. Furthermore, when V_{heater} = 1.8 V, the proposed Lamé resonator's peak-to-floor increases to 18 dB. The peak transmission magnitude increases by 8.54 dB (2.67×) when the heater is biased at 1.8 V,

indicating the impact of the thermal actuator-driven transducer gap reduction. This represents a significant reduction in the motional resistance of the device.
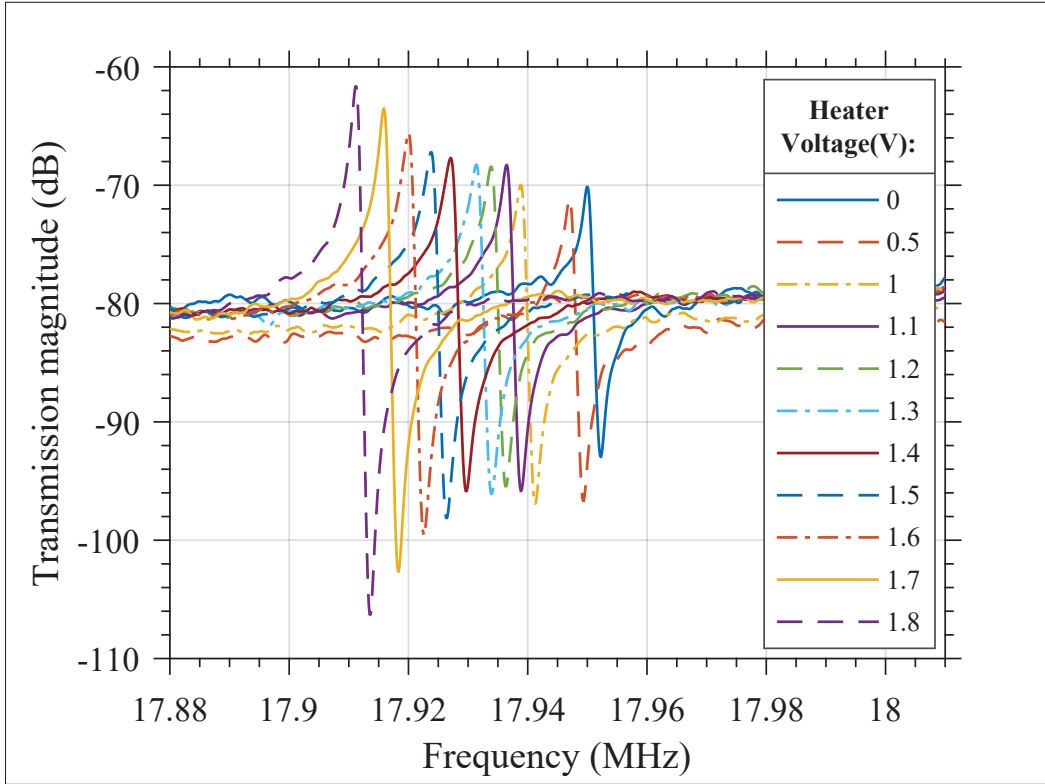
Figure 3.10   Measured resonator frequency response in vacuum vs different applied heater voltages

3.4   Discussion

In this work, chevron-shaped thermal actuators are proposed to reduce the air gap of bulk-mode Lamé resonators and simultaneously provide heating to improve their temperature stability. According to the experimental results presented in Section 2.4, the electrostatic gap can be reduced from 2.5 μm to 0.5 μm by applying 2.7 V to the heater in atmospheric pressure.

The thermal actuation allows the resonator to have a controlled analog displacement, as seen in Fig. 3.7, unlike electrostatic actuation, which is prone to unstable pull-in. Thus, the transducer gap will not experience an abrupt change when the heater voltage is adjusted; therefore, a

subsequent design could remove the stopper structure and use the thermal actuator to further reduce the transducer gap size and the motional resistance and lower the required bias voltage beyond what was presented in this work.

Measurements illustrate that each heater consumes approximately 155 mW when the gap is reduced to 0.5 μm in atmospheric pressure and about 39 mW in vacuum. This power can heat up the chevron structure to 610°C in atmospheric pressure and is in good agreement with the FEM simulation. This heat propagates to the resonator and increases the suspended square temperature. Consequently, the resonator center frequency changes from 17.97 MHz to 17.86 MHz when the heater voltage varies from 0 V to 2.7 V in atmospheric pressure and from 17.95 to 17.91 MHz when the heater voltage varies from 0 V to 1.8 V in vacuum. The resonator frequency response data in atmospheric pressure indicates that the center frequency drifts by 118.2 kHz, and the FLIR camera reveals a 120°C temperature rise over the suspended square when V_{heater} varies from 0 V to 2.6 V, resulting in a TCF of -55.16 ppm/°C in air. As temperature measurements of the suspended square were not possible in vacuum, the TCF could not be extracted in that environment.

Increasing the heater voltage above 2.7 V in atmospheric pressure and 1.8 V in vacuum remains possible but can eventually melt the PADMETAL layer over the chevron-shaped thermal actuator and destroy the actuator. It is worth noting that the maximum temperature of the suspended square in vacuum is lower than at atmospheric pressure due to the absence of free convection.

While this work provides gap closing to enhance motional resistance and the thermal actuator also heats the resonator to provide a path to increase its temperature stability simultaneously, other stat-of-the-art works presented in Table 3.3 do not attempt to simultaneously achieve these goals. Electrostatic force usage to reduce the gap to 200 nm is presented in Elsayed & Nabki (2019). Work in Wang, Bao, Ling & Li (2015a) reduces the electrostatic gap from 2.5 μm to 0.5 μm with a spring for each sensing actuator, but the design is not fabricated. In Jiang *et al.* (2013), a complex structure for an electrostatic gap closer is presented to reduce the original gap from 1.05 μm to 50 nm; however, no fabricated device is demonstrated. In differential bulk-mode

resonators, such as Li, Bao, Huang, Ling, Zheng & Du (2016a); Elsayed & Nabki (2017b), a firm spring with stoppers is utilized to reduce the gap from 2.5 μm to 0.5 μm. These designs, however, do not provide heating of the resonator structure to provide a path to temperature compensation. In this work, the proposed design uniquely presents a thermal actuator that is used for gap-closing, which does not require high voltages or suffer from pull-in effects, and that can be used for temperature compensation concurrently.

Although the micro-heater consumes relatively high power, it is a widely used method for temperature compensation due to its high stability. The distance between the micro-heater and resonator significantly impacts power consumption; therefore, the micro-heater implementation over the resonator can reduce the current draw from the power supply. In Mahmoud *et al.* (2020), the heater is placed above the Lamé resonator and works with 90 mW to reach a resonator temperature of 105°C. This is compared to 620 mW and 156 mW in atmospheric pressure and vacuum, respectively, in this work. Furthermore, a high-efficiency micro-oven is demonstrated in Comenencia Ortiz, Kwon, Rodriguez, Chen, Vukasin, Heinz, Shin & Kenny (2020a), and the oven consumes only 18 mW to stabilize the resonator frequency for temperatures up to 100°C. The power consumption of the proposed device may be decreased by removing the additional supporting anchors placed at the actuators to improve mechanical stability or increase the chevron length.

Table 3.3　Comparison between the proposed resonator and the state-of-the-art

Reference	Mode shape	Frequency (MHz)	Gap closer			Micro-oven	Feedback	Fabrication
			Gap closer type	Initial Gap (nm)	Final gap (nm)	Power Consumption (mW)		
Pei et al. (2020)	Length extensional	10.5	N/A	N/A	N/A	108	Yes	Yes
Kwon et al. (2020)	Dual-mode (Lamé/Plate Bending)	1/13.5	N/A	N/A	N/A	-	No	Yes
Comenencia Ortiz et al. (2020b)	Dual-mode (Lamé/DETF)	20.16/0.98	N/A	N/A	N/A	30	No	Yes
Elsayed & Nabki (2019)	Lamé	18	Capacitive	2500	200	N/A	N/A	Yes
Kwon, Ortiz, Vukasin, Chen, Shin & Kenny (2019)	Dual-mode (Lamé/DETF)	20.2/1.17	N/A	N/A	N/A	10	Yes	Yes
Islam et al. (2019)	Lamé	0.4-15	N/A	N/A	N/A	10.8	Yes	Yes
Liu, Tabrizian & Ayazi (2018b)	Lamé	77.7	N/A	N/A	N/A	383(@-25°C ambient)	Yes	Yes
Pei, Zhong, Sun, Yang & Li (2018)	Length extensional	10.4	N/A	N/A	N/A	-	No	Yes
Zhao, Yuan, Sun, Yang & Sun (2018)	Wine glass	150.5	N/A	N/A	N/A	15(@100°C)	No	Yes
Elsayed & Nabki (2017b)	Lamé	18	Capacitive	2500	500	N/A	N/A	Yes
You, Yang, Sun, Pei & Li (2017)	Length extensional	10.5	N/A	N/A	N/A	-	No	Yes
Li, Bao, Huang, Ling, Zheng & Du (2016b)	Wine glass	9.45	Capacitive	2500	500	N/A	N/A	Yes
Liu, Li, Chen & Li (2016)	DETF	1.4	N/A	N/A	N/A	0.9(@110°C)	No	Yes
Li, Chen, Li, Chin & Li (2015)	DETF	1.2	N/A	N/A	N/A	1.8	Yes	Yes
Wang et al. (2015a)	Lamé	10	Capacitive	2500	500	N/A	N/A	Yes
Wu & Rais-Zadeh (2015)	Length extensional	80	N/A	N/A	N/A	8	Yes	Yes
Xu, Segovia-Fernandez & Piazza (2015)	Bulk mode/ Length Extensional	70-1160	N/A	N/A	N/A	0.4	No	Yes
Chen, Chin, Li & Li (2015)	DETF	1.19	N/A	N/A	N/A	0.5(@150°C)	No	Yes
Toan, Toda, Kawai & Ono (2014)	Width extensional	9.65	Capacitive	400	100	N/A	N/A	Yes
Van Toan & Ono (2014)	Width extensional	9.65	Capacitive	400	100	N/A	N/A	Yes
Ng, Yang, Hong, Ahn, Christensen, Gibson, Qalandar, Turner & Kenny (2014)	Width extensional	50	Capacitive	900	200	N/A	N/A	Yes
Jiang et al. (2013)	Lamé	70	Capacitive	1050	50	N/A	N/A	No
Tazzoli et al. (2011)	Contour-extensional	1100	N/A	N/A	N/A	N/A	No	Yes
Salvia, Melamud, Chandorkar, Lord & Kenny (2010)	DETF	1.2	N/A	N/A	N/A	15-20	Yes	Yes
Jha, Hopcroft, Chandorkar, Salvia, Agarwal, Candler, Melamud, Bongsang Kim & Kenny (2008)	DETF	1.3	N/A	N/A	N/A	12(@125°C)	Yes	Yes
Shao, Palaniapan, Khine & Tan (2007)	Lamé	6.35	Capacitive	2500	640	N/A	N/A	Yes
This work	Lamé	17.9	Thermal	2500	500	620 (air) / 156 (vacuum)	No	Yes

3.5   Conclusion

This paper presented a novel Lamé mode electrostatic resonator that employs a thermal transducer gap reduction mechanism to reduce the motional resistance and overcome the microfabrication process limitation related to the minimum spacing of the structural silicon layer. This method allows for the reduction of the transducer gap from 2.5 μm to 0.5 μm, resulting in lower motional resistance (2.67× lower in vacuum) and consequently reduced insertion loss. The resonant frequency for the fabricated resonator is measured at about 17.9 MHz, which is in agreement with the simulations. In order to reach a 0.5 μm transducer gap in atmospheric pressure, the four heaters consume 620 mW from a 2.7 V power supply and 156 mW from a 1.8 V power supply in vacuum. Integrating the heaters and the resonator in a minimal area can lead to frequency stability over temperature by employing the ovenization concept used in oscillators. Furthermore, the FEM simulations using COMSOL are in good agreement with the measurement data, and it is possible to estimate the temperature of the suspended square in vacuum without access to monitor the temperature directly.

Author Contributions

For this article, A.Kolahdouz and F.Nabki developed the idea. A.Kolahdouz performed the design, simulation, and layout preparation of the MEMS resonators. A.Kolahdouz performed the measurements of the prototypes. A.Kolahdouz and S.Nabavi analyzed the results. A.Kolahdouz prepared the manuscript, and S.Nabavi and F.Nabki edited it. This work was carried out under the supervision of F.Nabki.

CONCLUSION AND RECOMMENDATIONS

Research Summary

This thesis aimed to study, design, and characterize bulk micromachined silicon MEMS Lamé resonators in order to increase frequency stability over temperature and signal transmission. This dissertation's first achievement is an analytical model to predict the resonant frequency behavior of silicon MEMS Lamé resonators. The proposed model can be modified when passive temperature compensation methods are employed. Consequently, this model accurately depicts the resonator's behavior response before fabrication, resulting in a clearer vision of the constructed resonator output and savings in manufacturing costs. Moreover, it is demonstrated that the devices' resonant frequency and frequency-temperature dependency can be predicted using a derived analytical model once elastic parameters have been retrieved from the measurements.

In the mechanical design of MEMS resonators, the lateral transducer gap is a critical component that affects the resonators' sensing and actuation capabilities. It is important to note that the transducer gap cannot be decreased in the majority of cases due to manufacturing constraints. This restricts the transduction characteristics of these devices, resulting in relatively high motional resistance. This thesis offers a novel capacitive bulk mode resonator functioning in Lamé mode, where the transduction and temperature stability are enhanced by employing a thermal actuation technique to decrease the transducer gaps. Thermal actuation allows for the actuator to operate at low voltages at the expense of an increase in power consumption. Additionally, the proximity of the heater to the resonator permits the use of the dissipated heat to increase the resonator's temperature relative to the ambient temperature and thus allow ovenization to enhance temperature stability.

Future Work and Recommendations

There are still numerous parts of this research that can be enhanced. The focus of this thesis was primarily on the bulk mode Lamé resonator and its temperature stability; nevertheless, the prospect of adapting these ideas to any resonator can strengthen the presented methodologies. Several suggestions for improving this dissertation are as follows:

- **Expand the model to compatible with any MEMS resonator:**

    The purpose of the suggested model was to investigate the resonant frequency and temperature dependence behavior of bulk micromachined silicon MEMS Lamé resonators when various passive temperature compensation methods are implemented. This model can be used for any resonator whose structural layer is composed of silicon. A general model would enhance the resonator's frequency and behavior prediction regardless of mode shape and actuation mechanism. In addition, the model may incorporate some active approaches for temperature compensation (e.g., resonator DC bias) to further improve it.

- **Further optimization in the fabricated temperature-compensated resonators:**

    The purpose of the manufactured Lamé resonators was to validate the model empirically. Regarding the model's accuracy, it is feasible to further improve the resonator by rearranging the holes and adjusting their diameters.

- **Design the signal pads to be compatible with GSG probes:**

    The transmission can be considerably enhanced by probing the resonator using GSG probes. The excessive feedthrough caused by the additional PADMETAL wires, which deliver the

signal to the pads, the wire bonds, and PCB traces, can be eliminated by employing over-die testing with GSG probes instead of PCB-level testing.

- **Integrate the proposed resonators with the CMOS circuit:**

  Combining the resonator with a transimpedance amplifier (TIA) can result in a fully integrated CMOS-MEMS oscillator. This circuit will be used to sustain oscillation in a closed loop with the MEMS resonator. This amplifier can interface with the resonator in either single-ended or differential mode, though the differential mode is recommended since it can improve transmission and reduce resonator feedthrough.

- **Improve chevron-shaped thermal actuators in order to reduce power consumption:**

  The prototype chevron-shaped thermal actuators were created with maximum mechanical stability in consideration, as opposed to optimal power consumption. Through measurement and mechanical shock testing, it has been demonstrated that the chevrons can withstand more significant mechanical stress than anticipated. Extending the heater length and removing the support anchor from the chevron would reduce power usage. Longer heater lengths will result in more significant thermal expansion at lower actuation voltages and powers.

- **Implement two separate heaters on each chevron:**

  Chapter 3 investigated the resonator temperature variation for the suggested design with chevron-shaped thermal actuators. It has been observed that the resonator temperature can be adjusted in proportion to the heater temperature; however, in a vacuum, the resonator

temperature cannot exceed 70 degrees Celsius due to the absence of air molecules, which eliminates free convection.

It is a good idea to install two heaters on each chevron: one to heat up the chevron and close the electrostatic gap, as stated, and another to boost the temperature of the resonator transducer electrodes. This concept would further reduce the resonator's heater power consumption and grant the capacity to regulate the resonator's temperature regardless of the actuator's status.

- **Implement a feedback loop to control the proposed Lamé resonator:**

As it is depicted in Chapter 3, the heaters determine the resonator's temperature over the chevron; as there is no feedback in this design, the resonator temperature is an unknown parameter. It would be conceivable to include a temperature sensor in the proposed resonator and measure its temperature to achieve complete temperature control at any applied temperature.

Academic Achievements

During this master's degree, numerous academic accomplishments were attained. These achievements have been divided into two categories: peer-reviewed journal publications and academic awards.

Submitted journal articles with peer review:
Item: "Temperature Dependence Modeling and Thermal Sensitivity Reduction of Bulk Micromachined Silicon MEMS Lamé Resonators." by A. Kolahdouz, S.Nabavi, and F.Nabki, submitted to the IEEE Journal of Microelectromechanical Systems (JMEMS), on 2022/10/7.
Item: "Lamé Resonator Integrated with Chevron-shaped Thermal Actuators to Improve Motional Resistance and Temperature Stability." by A. Kolahdouz, S.Nabavi, and F.Nabki, submitted to the IEEE Journal of Microelectromechanical Systems (JMEMS), on 2022/11/8.

The academic achievement:

• Awarded with "Exemption des Frais Majorés à la Maîtrise" for three consecutive semesters

Closing remarks

The results of the thesis provide recommendations for MEMS Lamé resonators with enhanced temperature stability and modeling insight into the investigated temperature compensation mechanisms. The provided model enables the prediction of the resonant frequency and TCF behavior, utilizing the various compensating approaches. In addition, the proposed Lamé mode electrostatic resonator is augmented with a thermal transducer gas closer mechanism in order to overcome fabrication limits in the minimum spacing of the structural silicon layer and decrease the motional resistance. Moreover, the FEM simulations for the proposed resonator are in remarkable agreement with the measurement results, and it is possible to estimate the temperature of the suspended square in vacuum without direct access to temperature measurement.

Moreover, the proposed Lamé resonator shows potential to be incorporated into an oscillator loop in order to provide a high-performance MEMS-based timing solution.

APPENDIX I

ETS320 FLIR THERMAL CAMERA CALIBRATION PROCEDURE

Temperature measuring using a thermal camera necessitates calibration. This calibration establishes the relation between the input signal and the physical quantity the user wishes to measure, in this case temperature. A non-calibrated infrared camera is incapable of measuring absolute brightness or temperature. Whether FLIR Systems or the user does the calibration, the information is recorded in calibration curves, which are mathematical functions. As the strength of the radiation varies with both temperature and the object's distance from the camera, distinct curves are created for various temperature ranges and interchangeable lenses.

A proper and accurate measurement needs the material emissivity, the reflection temperature and the camera distance as the measurement parameters. Figure I-1 shows the FLIR menu regarding the measurement parameters. The silicon emissivity is know to be of around 0.65 at room temperature for the visible light spectrum (i.e., 380 nm to 750 nm) (Ravindra, Sopori, Gokce, Cheng, Shenoy, Jin, Abedrabbo, Chen & Zhang (2001)). For FR-4 material, the emissivity is around 0.95 at room temperature in the visible light spectrum. This parameter adjustment leads to proper absolute temperature values, as reported in this thesis.

Figure-A I-1   ETS320 FLIR
thermal camera measurement
parameters menu

Moreover, to guarantee the reliability of the measured temperature, a temperature sensor
(MCP9700) is placed on the PCB heater, as depicted in figure I-2. The measured temperature
from the temperature sensor and FLIR camera can be compared to ensure the accuracy of the
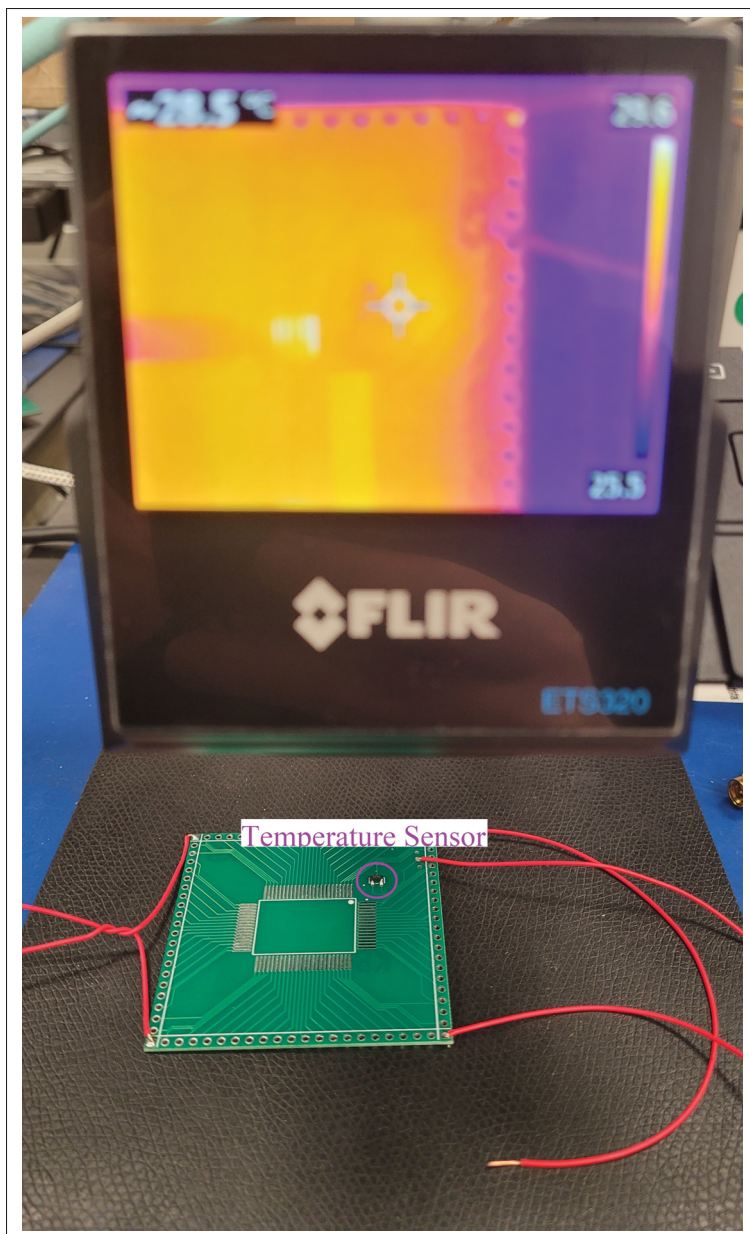camera parameter adjustment.

Figure-A I-2   ETS320 FLIR thermal camera and
heater PCB enhanced with temperature sensor

BIBLIOGRAPHY

Scopus analyze search. Retrieved www.scopus.com.

Abdolvand, R., Lavasani, H., Ho, G. & Ayazi, F. (2008). Thin-film piezoelectric-on-silicon resonators for high-frequency reference oscillator applications. *IEEE Transactions on Ultrasonics, Ferroelectrics and Frequency Control*, 55(12), 2596–2606. doi: 10.1109/TUFFC.2008.976.

Abdolvand, R., Bahreyni, B., Lee, J. & Nabki, F. (2016). Micromachined Resonators: A Review. *Micromachines*, 7(9), 160. doi: 10.3390/mi7090160.

Ansari, A. & Rais-Zadeh, M. (2014). A temperature-compensated Gallium nitride micromechanical resonator. *IEEE Electron Device Letters*, 35(11), 1127–1129. doi: 10.1109/LED.2014.2358577.

Arft, C., Lu, Y.-C. & Parvereshi, J. (2016). MEMS Oscillators with Improved Resilience for Harsh Automotive Environments. *SAE International Journal of Passenger Cars - Electronic and Electrical Systems*, 9(1), 2016–01. doi: 10.4271/2016-01-0101.

Beaulieu, P.-O. (2019). *Conception et intégration de circuits CMOS et de microsystèmes électromécaniques (MEMS) pour la synthèse d ' un oscillateur à haute performance par*. (Ph.D. thesis, 'École de technologie supérieure IL). Retrieved https://espace.etsmtl.ca/id/eprint/2329/.

Bouchami, A., Elsayed, M. Y. & Nabki, F. (2018). A 1.4-mW 14-MHz MEMS Oscillator Based on a Differential Adjustable-Bandwidth Transimpedance Amplifier and Piezoelectric Disk Resonator. *IEEE Transactions on Circuits and Systems I: Regular Papers*, 65(10), 3414–3423. doi: 10.1109/TCSI.2018.2835419.

Bouchami, A., Elsayed, M. Y. & Nabki, F. (2019). A Sub-mW 18-MHz MEMS Oscillator Based on a 98-dBΩ Adjustable Bandwidth Transimpedance Amplifier and a Lamé-Mode Resonator. *Sensors*, 19(12), 2680. doi: 10.3390/s19122680.

Brantley, W. A. (1973). Calculated elastic constants for stress problems associated with semiconductor devices. *Journal of Applied Physics*, 44(1), 534–535. doi: 10.1063/1.1661935.

Chadwick, A., Sievers, L. & Perry, B. (2022). *SiTime Reports First Quarter 2022 Financial Results*. SiTime. Retrieved https://investor.sitime.com/news-releases/news-release-details/sitime-reports-first-quarter-2022-financial-results.

Chekurov, N., Grigoras, K., Sainiemi, L., Peltonen, A., Tittonen, I. & Franssila, S. (2010). Dry fabrication of microdevices by the combination of focused ion beam and cryogenic deep reactive ion etching. *Journal of Micromechanics and Microengineering*, 20(8), 085009. doi: 10.1088/0960-1317/20/8/085009.

Chen, C.-Y., Chin, C.-H., Li, M.-H. & Li, S.-S. (2015, 6). Statistical characterizaton of a CMOS-MEMS resonator for monolithic ovenized oscillator applications. *2015 Transducers - 2015 18th International Conference on Solid-State Sensors, Actuators and Microsystems (TRANSDUCERS)*, pp. 1965–1968. doi: 10.1109/TRANSDUCERS.2015.7181338.

Chen, Z., Wang, T., Jia, Q., Yang, J., Yuan, Q., Zhu, Y. & Yang, F. (2021). A Novel Lamé Mode RF-MEMS resonator with high quality factor. *International Journal of Mechanical Sciences*, 204(April), 106484. doi: 10.1016/j.ijmecsci.2021.106484.

Cho, C.-H., Cha, H.-Y. & Sung, H.-K. (2016). Characterization of Stiffness Coefficients of Silicon Versus Temperature using "Poisson's Rati" Measurements. *JSTS:Journal of Semiconductor Technology and Science*, 16(2), 153–158. doi: 10.5573/JSTS.2016.16.2.153.

Civet, Y., Casset, F., Carpentier, J., Icard, B., Bustos, J., Leverd, F., Mercier, D. & Basrour, S. (2011). Holed MEM Resonators with High Aspect Ratio, for High Accuracy Frequency Trimming. *Procedia Engineering*, 25(1), 531–534. doi: 10.1016/j.proeng.2011.12.132.

Comenencia Ortiz, L., Kwon, H.-K., Rodriguez, J., Chen, Y., Vukasin, G. D., Heinz, D. B., Shin, D. D. & Kenny, T. W. (2020a). Low-Power Dual Mode MEMS Resonators With PPB Stability Over Temperature. *Journal of Microelectromechanical Systems*, 29(2), 190–201. doi: 10.1109/JMEMS.2020.2970609.

Comenencia Ortiz, L., Kwon, H.-K., Rodriguez, J., Chen, Y., Vukasin, G. D., Heinz, D. B., Shin, D. D. & Kenny, T. W. (2020b). Low-Power Dual Mode MEMS Resonators With PPB Stability Over Temperature. *Journal of Microelectromechanical Systems*, 29(2), 190–201. doi: 10.1109/JMEMS.2020.2970609.

Cowen, A., Hames, G., Glukh, K. & Hardy, B. (2014). PiezoMUMPs Design Handbook a MUMPs ® process. *MEMSCAP Inc*, 1.

D. M. Chen, Kuypers, J. H., Gaidarzhy, A. & Zolfagharkhani, G. (2013). Mechanical resonating structures including a temperature compensation structure. Retrieved https://patents.google.com/patent/EP2377176A1/en.

de Laat, M. L. C., Pérez Garza, H. H., Herder, J. L. & Ghatkesar, M. K. (2016). A review on in situ stiffness adjustment methods in MEMS. *Journal of Micromechanics and Microengineering*, 26(6), 063001. doi: 10.1088/0960-1317/26/6/063001.

Duwel, A., Candler, R. N., Kenny, T. W. & Varghese, M. (2006). Engineering MEMS Resonators With Low Thermoelastic Damping. *Journal of Microelectromechanical Systems*, 15(6), 1437–1445. doi: 10.1109/JMEMS.2006.883573.

Electronic Products. (2017). *MEMS-based TCXOs improve telecom and networking equipment*. Electronic Products. Retrieved https://www.electronicproducts.com/mems-based-tcxos-improve-telecom-and-networking-equipment/.

Elsayed, M. Y., Nabki, F. & El-Gamal, M. N. (2013a, 1). A combined comb / bulk mode gyroscope structure for enhanced sensitivity. *2013 IEEE 26th International Conference on Micro Electro Mechanical Systems (MEMS)*, (1), 649–652. doi: 10.1109/MEM-SYS.2013.6474325.

Elsayed, M. Y. & Nabki, F. (2017a). 18-MHz Silicon Lamé Mode Resonators With Corner and Central Anchor Architectures in a Dual-Wafer SOI Technology. *Journal of Microelectromechanical Systems*, 26(1), 67–74. doi: 10.1109/JMEMS.2016.2607118.

Elsayed, M. Y. & Nabki, F. (2017b, 7). Capacitive Lamé mode resonator with gap closing mechanism for motional resistance reduction. *2017 Joint Conference of the European Frequency and Time Forum and IEEE International Frequency Control Symposium (EFTF/IFC)*, pp. 203–205. doi: 10.1109/FCS.2017.8088846.

Elsayed, M. Y. & Nabki, F. (2017c). Piezoelectric Bulk Mode Disk Resonator Post-Processed for Enhanced Quality Factor Performance. *Journal of Microelectromechanical Systems*, 26(1), 75–83. doi: 10.1109/JMEMS.2016.2633385.

Elsayed, M. Y. & Nabki, F. (2019). 870000 Q-Factor Capacitive Lamé Mode Resonator With Gap Closing Electrodes Enabling 4.4 kΩ Equivalent Resistance at 50 V. *IEEE Transactions on Ultrasonics, Ferroelectrics, and Frequency Control*, 66(4), 717–726. doi: 10.1109/TUFFC.2019.2892227.

Elsayed, M. Y., Nabki, F. & El-Gamal, M. N. (2013b). A novel comb architecture for enhancing the sensitivity of bulk mode gyroscopes. *Sensors (Switzerland)*, 13(12), 16641–16656. doi: 10.3390/s131216641.

Elsayed, M. Y., Cicek, P.-V., Nabki, F. & El-Gamal, M. N. (2016). Bulk Mode Disk Resonator With Transverse Piezoelectric Actuation and Electrostatic Tuning. *Journal of Microelectromechanical Systems*, 25(2), 252–261. doi: 10.1109/JMEMS.2016.2514267.

Green, B., Chu, K., Chumbes, E., Smart, J., Shealy, J. & Eastman, L. (2000). The effect of surface passivation on the microwave characteristics of undoped AlGaN/GaN HEMTs. *IEEE Electron Device Letters*, 21(6), 268–270. doi: 10.1109/55.843146.

Gronicz, J., Aaltonen, L., Chekurov, N. & Halonen, K. (2016). Electro-mechanical hybrid PLL for MEMS oscillator temperature compensation system. *Analog Integrated Circuits and Signal Processing*, 86(3), 385–391. doi: 10.1007/s10470-015-0685-x.

Hajjam, A., Rahafrooz, A. & Pourkamali, S. (2010). Sub-100ppb/°C temperature stability in thermally actuated high frequency silicon resonators via degenerate phosphorous doping and bias current optimization. *Technical Digest - International Electron Devices Meeting, IEDM*, (303), 170–173. doi: 10.1109/IEDM.2010.5703317.

Hall, J. J. (1967). Electronic Effects in the Elastic Constants of n-Type Silicon. *Physical Review*, 161(3), 756–761. doi: 10.1103/PhysRev.161.756.

Hopcroft, M. (2010). What is the Young's Modulus of Silicon? What is the Crystal Orientation in a Silicon Wafer? *Physical Acoustics*, 19(2), 229–238.

Houri Johari & Farrokh Ayazi. (2007, 1). High-frequency capacitive disk gyroscopes in (100) and (111) silicon. *2007 IEEE 20th International Conference on Micro Electro Mechanical Systems (MEMS)*, (January), 47–50. doi: 10.1109/MEMSYS.2007.4433009.

Hung, L.-W. & Nguyen, C. T. (2011, 1). Capacitive-piezoelectric AlN resonators with Q. *2011 IEEE 24th International Conference on Micro Electro Mechanical Systems*, pp. 173–176. doi: 10.1109/MEMSYS.2011.5734389.

Islam, M., Wei, R., Lee, J., Xie, Y., Mandal, S. & Feng, P. (2018). A Temperature-Compensated Single-Crystal Silicon-on-Insulator (SOI) MEMS Oscillator with a CMOS Amplifier Chip. *Micromachines*, 9(11), 559. doi: 10.3390/mi9110559.

Islam, M. S., Singh, S. K., Xereas, G., Chodavarapu, V. P. & Mandal, S. (2019). A Digitally Programmable CMOS Feedback ASIC for Highly Stable MEMS-Referenced Oscillators. *IEEE Transactions on Circuits and Systems I: Regular Papers*, 66(11), 4158–4171. doi: 10.1109/TCSI.2019.2926383.

Jaakkola, A., Prunnila, M. & Pensala, T. (2012, 5). Temperature compensated resonance modes of degenerately n-doped silicon MEMS resonators. *2012 IEEE International Frequency Control Symposium Proceedings*, (1), 1–5. doi: 10.1109/FCS.2012.6243712.

Jaakkola, A., Gorelick, S., Prunnila, M., Dekker, J., Pensala, T. & Pekko, P. (2014a, 5). Long term stability and quality factors of degenerately n-type doped silicon resonators. *2014 IEEE International Frequency Control Symposium (FCS)*, 4, 1–5. doi: 10.1109/FCS.2014.6859866.

Jaakkola, A., Prunnila, M., Pensala, T., Dekker, J. & Pekko, P. (2014b). Determination of doping and temperature-dependent elastic constants of degenerately doped silicon from MEMS resonators. *IEEE Transactions on Ultrasonics, Ferroelectrics, and Frequency Control*, 61(7), 1063–1074. doi: 10.1109/TUFFC.2014.3007.

Jaakkola, A., Prunnila, M., Pensala, T., Dekker, J. & Pekko, P. (2015). Design Rules for Temperature Compensated Degenerately n-Type-Doped Silicon MEMS Resonators. *Journal of Microelectromechanical Systems*, 24(6), 1832–1839. doi: 10.1109/JMEMS.2015.2443379.

Jha, C., Hopcroft, M., Chandorkar, S., Salvia, J., Agarwal, M., Candler, R., Melamud, R., Bongsang Kim & Kenny, T. (2008). Thermal Isolation of Encapsulated MEMS Resonators. *Journal of Microelectromechanical Systems*, 17(1), 175–184. doi: 10.1109/JMEMS.2007.904332.

Jiang, J. W., Bao, J. F., Du, Y. J. & Deng, C. (2013). A novel movable electrode for realizing deep sub-micrometer gap in SOI-based MEMS square resonator. *Microsystem Technologies*, 19(5), 763–772. doi: 10.1007/s00542-012-1683-x.

Keyes, R. W. (2010). The Electronic Contribution to the Elastic Properties of Germanium. *IBM Journal of Research and Development*, 5(4), 266–278. doi: 10.1147/rd.54.0266.

Kubena, R. L., Stratton, F. P., Nguyen, H. D., Kirby, D. J., Chang, D. T., Joyce, R. J., Yong, Y. K., Garstecki, J. F., Cross, M. D. & Seman, S. E. (2017, 7). A fully integrated quartz MEMS VHF TCXO. *2017 Joint Conference of the European Frequency and Time Forum and IEEE International Frequency Control Symposium (EFTF/IFC)*, 65(6), 68–71. doi: 10.1109/FCS.2017.8088803.

Kwon, H.-k., Ortiz, L. C., Vukasin, G. D., Chen, Y., Shin, D. D. & Kenny, T. W. (2019, 6). An Oven-Controlled MEMS Oscillator (OCMO) With Sub 10mw, ± 1.5 PPB Stability Over Temperature. *2019 20th International Conference on Solid-State Sensors, Actuators and Microsystems & Eurosensors XXXIII (TRANSDUCERS & EUROSENSORS XXXIII)*, (June), 2072–2075. doi: 10.1109/TRANSDUCERS.2019.8808255.

Kwon, H.-k., Vukasin, G. D., Bousse, N. E. & Kenny, T. W. (2020). Crystal Orientation Dependent Dual Frequency Ovenized MEMS Resonator With Temperature Stability and Shock Robustness. *Journal of Microelectromechanical Systems*, 29(5), 1130–1131. doi: 10.1109/JMEMS.2020.3012109.

Lakin, K. M., McCarron, K. T. & McDonald, J. F. (2000). Temperature compensated bulk acoustic thin film resonators. *Proceedings of the IEEE Ultrasonics Symposium*, 1, 855–858. doi: 10.1109/ULTSYM.2000.922677.

Lam, C. S. (2008). A review of the recent development of mems and crystal oscillators and their impacts on the frequency control products industry. *Proceedings - IEEE Ultrasonics Symposium*, 694–704. doi: 10.1109/ULTSYM.2008.0167.

Lee, H., Partridge, A. & Assaderaghi, F. (2012, 5). Low jitter and temperature stable MEMS oscillators. *2012 IEEE International Frequency Control Symposium Proceedings*, pp. 1–5. doi: 10.1109/FCS.2012.6243704.

Lee, J. E., Zhu, Y. & Seshia, A. A. (2008). A bulk acoustic mode single-crystal silicon microresonator with a high-quality factor. *Journal of Micromechanics and Microengineering*, 18(6), 064001. doi: 10.1088/0960-1317/18/6/064001.

Lee, J. E. & Seshia, A. A. (2011). Direct parameter extraction in feedthrough-embedded capacitive MEMS resonators. *Sensors and Actuators A: Physical*, 167(2), 237–244. doi: 10.1016/j.sna.2011.02.016.

Li, M.-H., Chen, C.-Y., Li, C.-S., Chin, C.-H. & Li, S.-S. (2015). A Monolithic CMOS-MEMS Oscillator Based on an Ultra-Low-Power Ovenized Micromechanical Resonator. *Journal of Microelectromechanical Systems*, 24(2), 360–372. doi: 10.1109/JMEMS.2014.2331497.

Li, X., Bao, J., Huang, Y., Ling, Y., Zheng, Y. & Du, Y. (2016a). A 9.45 MHz micromechanical disk resonator with movable electrodes for gap reduction. *Sensors and Actuators, A: Physical*, 243, 66–70. doi: 10.1016/j.sna.2016.03.010.

Li, X., Bao, J., Huang, Y., Ling, Y., Zheng, Y. & Du, Y. (2016b). A 9.45MHz micromechanical disk resonator with movable electrodes for gap reduction. *Sensors and Actuators A: Physical*, 243, 66–70. doi: 10.1016/j.sna.2016.03.010.

Liu, C.-S., Tabrizian, R. & Ayazi, F. (2018a). A ±0.3 ppm Oven-Controlled MEMS Oscillator Using Structural Resistance-Based Temperature Sensing. *IEEE Transactions on Ultrasonics, Ferroelectrics, and Frequency Control*, 65(8), 1492–1499. doi: 10.1109/TUFFC.2018.2843781.

Liu, C.-S., Tabrizian, R. & Ayazi, F. (2018b). A ±0.3 ppm Oven-Controlled MEMS Oscillator Using Structural Resistance-Based Temperature Sensing. *IEEE Transactions on Ultrasonics, Ferroelectrics, and Frequency Control*, 65(8), 1492–1499. doi: 10.1109/TUFFC.2018.2843781.

Liu, C.-Y., Li, M.-H., Chen, C.-Y. & Li, S.-S. (2016, 5). An ovenized CMOS-MEMS oscillator with isothermal resonator and sub-mW heating power. *2016 IEEE International Frequency Control Symposium (IFCS)*, pp. 1–3. doi: 10.1109/FCS.2016.7546792.

Liu, Z. & Source, A. P. (2021). Temperature-Dependent Elastic Constants and Young's Modulus fo Silicon Single Crystal. *Proceedings of MEDSI2020*, 324–326. doi: 10.18429/JACoW-MEDSI2020-WEPC09.

Logan, D. L. (2022). *A First Course in the Finite Element Method, enhanced edition* (ed. 6). USA: Cengage Learning. Retrieved https://www.cengage.ca/c/a-first-course-in-the-finite-element-method-enhanced-edition-6e-logan/9780357676424/.

Luschi, L. & Pieri, F. (2016). An analytical model for the resonance frequency of square perforated Lamé-mode resonators. *Sensors and Actuators, B: Chemical*, 222, 1233–1239. doi: 10.1016/j.snb.2015.07.085.

Luschi, L., Iannaccone, G. & Pieri, F. (2017). Temperature Compensation of Silicon Lamé Resonators Using Etch Holes: Theory and Design Methodology. *IEEE transactions on ultrasonics, ferroelectrics, and frequency control*, 64(5), 879–887. doi: 10.1109/TUFFC.2017.2667501.

Mahmoud, A., Mukherjee, T. & Piazza, G. (2020, 1). Investigating Long-Term Stability of Wide Bandwidth Surface Acoustic Waves Gyroscopes Using a Monolithically Integrated Micro-Oven. *2020 IEEE 33rd International Conference on Micro Electro Mechanical Systems (MEMS)*, 2020-Janua, 252–254. doi: 10.1109/MEMS46641.2020.9056180.

Marrison, W. A. (1948). The Evolution of the Quartz Crystal Clock. *Bell System Technical Journal*, 27(3), 510–588. doi: 10.1002/j.1538-7305.1948.tb01343.x.

Melamud, R., Kim, B., Chandorkar, S. A., Hopcroft, M. A., Agarwal, M., Jha, C. M. & Kenny, T. W. (2007). Temperature-compensated high-stability silicon resonators. *Applied Physics Letters*, 90(24), 244107. doi: 10.1063/1.2748092.

Melamud, R., Chandorkar, S., Bongsang Kim, Hyung Kyu Lee, Salvia, J., Bahl, G., Hopcroft, M. & Kenny, T. (2009). Temperature-Insensitive Composite Micromechanical Resonators. *Journal of Microelectromechanical Systems*, 18(6), 1409–1419. doi: 10.1109/JMEMS.2009.2030074.

Nabki, F., Ahmad, F., Allidina, K. & El-Gamal, M. N. (2008, 9). A compact and programmable high-frequency oscillator based on a MEMS resonator. *2008 IEEE Custom Integrated Circuits Conference*, (CICC), 337–340. doi: 10.1109/CICC.2008.4672090.

Nabki, F., Cicek, P.-V., Dusatko, T. A. & El-Gamal, M. N. (2011). Low-Stress CMOS-Compatible Silicon Carbide Surface-Micromachining Technology—Part II: Beam Resonators for MEMS Above IC. *Journal of Microelectromechanical Systems*, 20(3), 730–744. doi: 10.1109/JMEMS.2011.2115130.

Nathanson, H., Newell, W., Wickstrom, R. & Davis, J. (1967). The resonant gate transistor. *IEEE Transactions on Electron Devices*, 14(3), 117–133. doi: 10.1109/T-ED.1967.15912.

Ng, E. J., Yang, Y., Hong, V. A., Ahn, C. H., Christensen, D. L., Gibson, B. A., Qalandar, K. R., Turner, K. L. & Kenny, T. W. (2014, 1). Stable pull-in electrodes for narrow gap actuation. *2014 IEEE 27th International Conference on Micro Electro Mechanical Systems (MEMS)*, pp. 1281–1284. doi: 10.1109/MEMSYS.2014.6765883.

Ng, E. J., Hong, V. A., Yang, Y., Ahn, C. H., Everhart, C. L. & Kenny, T. W. (2015). Temperature dependence of the elastic constants of doped silicon. *Journal of Microelectromechanical Systems*, 24(3), 730–741. doi: 10.1109/JMEMS.2014.2347205.

Nicolson, A. M. (1940). *Generating and transmitting electric currents*. U.S. Patent 2,212,845. Retrieved https://patents.google.com/patent/US2212845A/en.

NYE, J. F. (1987). Physical properties of crystals. *Journal of Magnetism and Magnetic Materials*, 63-64(C), 40–42. doi: 10.1016/0304-8853(87)90515-4.

O'connor, J. J. (1960). A 400-CPS Tuning Fork Filter. *Proceedings of the IRE*, 48(11), 1857–1865. doi: 10.1109/JRPROC.1960.287420.

Pandit, M., Mustafazade, A., Sobreviela, G., Zhao, C., Zou, X. & Seshia, A. A. (2021). Experimental Observation of Temperature and Pressure Induced Frequency Fluctuations in Silicon MEMS Resonators. *Journal of Microelectromechanical Systems*, 30(4), 500–505. doi: 10.1109/JMEMS.2021.3077633.

Pei, B., Zhong, P., Sun, K., Yang, H. & Li, X. (2018, 1). Micro-oven-controlled MEMS oscillator with electrostatic tuning for frequency trimming. *2018 IEEE Micro Electro Mechanical Systems (MEMS)*, 2018-Janua(January), 731–734. doi: 10.1109/MEMSYS.2018.8346659.

Pei, B., Sun, K., Yang, H., Ye, C., Zhong, P., Yu, T. & Li, X. (2020). Oven-Controlled MEMS Oscillator with Integrated Micro-Evaporation Trimming. *Sensors*, 20(8), 2373. doi: 10.3390/s20082373.

Pensala, T., Prunnila, M. & Jaakkola, A. (2012, 5). Bulk acoustic wave propagation characteristics in degenerately n-doped Si. *2012 IEEE International Frequency Control Symposium Proceedings*, pp. 1–4. doi: 10.1109/FCS.2012.6243713.

Petersen, K. E. (1997). Silicon as a mechanical material. *Micromechanics and MEMS: Classic and Seminal Papers to 1990*, 70(5), 58–95. doi: 10.1109/9780470545263.sect1.

Rajai, P., Ahmed, H., Straeten, M., Xereas, G. & Ahamed, M. J. (2019). Analytical modeling of n-type doped silicon elastic constants and frequency-compensation of Lamé mode microresonators. *Sensors and Actuators, A: Physical*, 297, 111508. doi: 10.1016/j.sna.2019.07.032.

Ravindra, N. M., Sopori, B., Gokce, O. H., Cheng, S. X., Shenoy, A., Jin, L., Abedrabbo, S., Chen, W. & Zhang, Y. (2001). Emissivity measurements and modeling of silicon-related materials: An overview. *International Journal of Thermophysics*, 22(5), 1593–1611. doi: 10.1023/A:1012869710173.

Sähn, S. (1972). Ed. W. K. Nowacki, Progress in Thermoelasticity. (VIIIth European Mechanics Colloquium, Warszawa 1967). 235 S. m. Abb. Warszawa 1969. Państwowe Wydawnictwo Naukowe. Preis geb. zlS 69,—. *ZAMM - Zeitschrift für Angewandte Mathematik und Mechanik*, 52(8), 500–500. doi: 10.1002/zamm.19720520817.

Salvia, J. C., Melamud, R., Chandorkar, S. A., Lord, S. F. & Kenny, T. W. (2010). Real-Time Temperature Compensation of MEMS Oscillators Using an Integrated Micro-Oven and a Phase-Locked Loop. *Journal of Microelectromechanical Systems*, 19(1), 192–201. doi: 10.1109/JMEMS.2009.2035932.

Samarao, A., Casinovi, G. & Ayazi, F. (2010, 1). Passive TCF compensation in high Q silicon micromechanical resonators. *2010 IEEE 23rd International Conference on Micro Electro Mechanical Systems (MEMS)*, pp. 116–119. doi: 10.1109/MEMSYS.2010.5442553.

Samarao, A. K. & Ayazi, F. (2012). Temperature Compensation of Silicon Resonators via Degenerate Doping. *IEEE Transactions on Electron Devices*, 59(1), 87–93. doi: 10.1109/TED.2011.2172613.

Sandberg, R., Svendsen, W., Mølhave, K. & Boisen, A. (2005). Temperature and pressure dependence of resonance in multi-layer microcantilevers. *Journal of Micromechanics and Microengineering*, 15(8), 1454–1458. doi: 10.1088/0960-1317/15/8/011.

Shalaby, M., Abdelmoneum, M. & Saitou, K. (2009). Design of Spring Coupling for High-Q High-Frequency MEMS Filters for Wireless Applications. *IEEE Transactions on Industrial Electronics*, 56(4), 1022–1030. doi: 10.1109/TIE.2009.2014671.

Shao, L., Palaniapan, M., Khine, L. & Tan, W. (2007). Micromechanical resonators with sub-micron capacitive gaps in 2μm process. *Electronics Letters*, 43(25), 1427. doi: 10.1049/el:20072841.

Smith, J. H., Montague, S., Sniegowski, J. J., Murray, J. R. & McWhorter, P. J. (1995). Embedded micromechanical devices for the monolithic integration of MEMS with CMOS. *Technical Digest - International Electron Devices Meeting*, 609–612. doi: 10.1109/iedm.1995.499295.

Sundaresan, K., Ho, G. K., Pourkamali, S. & Ayazi, F. (2006, 9). A Low Phase Noise 100MHz Silicon BAW Reference Oscillator. *IEEE Custom Integrated Circuits Conference 2006*, (CICC), 841–844. doi: 10.1109/CICC.2006.320843.

Tabrizian, R., Casinovi, G. & Ayazi, F. (2010). Temperature-stable high-Q AlN-on-silicon resonators with embedded array of oxide pillars. *Technical Digest - Solid-State Sensors, Actuators, and Microsystems Workshop*, (December), 100–101. doi: 10.31438/trf.hh2010.28.

Tabrizian, R., Casinovi, G. & Ayazi, F. (2013). Temperature-stable silicon oxide (SilOx) micromechanical resonators. *IEEE Transactions on Electron Devices*, 60(8), 2656–2663. doi: 10.1109/TED.2013.2270434.

Tanaka, K., Kihara, R., Sánchez-Amores, A., Montserrat, J. & Esteve, J. (2007). Parasitic effect on silicon MEMS resonator model parameters. *Microelectronic Engineering*, 84(5-8), 1363–1368. doi: 10.1016/j.mee.2007.01.209.

Tazzoli, A., Rinaldi, M. & Piazza, G. (2011, 12). Ovenized high frequency oscillators based on aluminum nitride contour-mode MEMS resonators. *2011 International Electron Devices Meeting*, (c), 1–20. doi: 10.1109/IEDM.2011.6131589.

Thakar, V. A., Wu, Z., Figueroa, C. & Rais-Zadeh, M. (2014, 5). A temperature-stable clock using multiple temperature-compensated micro-resonators. *2014 IEEE International Frequency Control Symposium (FCS)*, pp. 1–4. doi: 10.1109/FCS.2014.6860013.

TheExpressWire. (2022). *MEMS Oscillators Market Size is Expected to Reach Around USD 6510 Million by 2028*. digitaljournal. Retrieved https://www.digitaljournal.com/pr/mems-oscillators-market-size-is-expected-to-reach-around-usd-6510-million-by-2028-cagr-9-7#:~:text=TheMEMSOscillatorsmarketwas,9.7%25duringtheforecastperiod.

Toan, N. V., Toda, M., Kawai, Y. & Ono, T. (2014). A capacitive silicon resonator with a movable electrode structure for gap width reduction. *Journal of Micromechanics and Microengineering*, 24(2), 025006. doi: 10.1088/0960-1317/24/2/025006.

Tu, C. & Lee, J. E. (2012a). Thermoelastic Dissipation in Etch-Hole Filled Lamé Bulk-Mode Silicon Microresonators. *IEEE Electron Device Letters*, 33(3), 450–452. doi: 10.1109/LED.2011.2179973.

Tu, C. & Lee, J. E. (2012b, 3). Study on thermoelastic dissipation in bulk mode resonators with etch holes. *2012 7th IEEE International Conference on Nano/Micro Engineered and Molecular Systems (NEMS)*, pp. 478–482. doi: 10.1109/NEMS.2012.6196821.

Van Toan, N. & Ono, T. (2014, 1). Capacitive silicon resonator structure with movable electrodes to reduce capacitive gap widths based on electrostatic parallel plate actuation. *2014 IEEE 27th International Conference on Micro Electro Mechanical Systems (MEMS)*, 1, 1245–1248. doi: 10.1109/MEMSYS.2014.6765874.

Wang, Q. P., Bao, J. F., Ling, Y. & Li, X. Y. (2015a). Design of a novel RF MEMS square resonator. *Microsystem Technologies*, 21(8), 1805–1810. doi: 10.1007/s00542-014-2295-4.

Wang, S., Bahr, B. & Li, S.-S. (2015b). Temperature coefficient of frequency modeling for CMOS-MEMS bulk mode composite resonators. *IEEE Transactions on Ultrasonics, Ferroelectrics, and Frequency Control*, 62(6), 1166–1178. doi: 10.1109/TUFFC.2014.006724.

Wu, G., Xu, D., Xiong, B. & Wang, Y. (2013). Effect of air damping on quality factor of bulk mode microresonators. *Microelectronic Engineering*, 103, 86–91. doi: 10.1016/j.mee.2012.10.004.

Wu, Z. & Rais-Zadeh, M. (2015). A Temperature-Stable Piezoelectric MEMS Oscillator Using a CMOS PLL Circuit for Temperature Sensing and Oven Control. *Journal of Microelectromechanical Systems*, 24(6), 1747–1758. doi: 10.1109/JMEMS.2015.2434832.

Xereas, G. & Chodavarapu, V. P. (2015). Wafer-Level Vacuum-Encapsulated Lamé Mode Resonator With f-Q Product of 2.23 × 10^13 Hz. *IEEE Electron Device Letters*, 36(10), 1079–1081. doi: 10.1109/LED.2015.2464713.

Xu, C., Segovia-Fernandez, J. & Piazza, G. (2015, 6). Sub-milliwatt integrated oven for temperature stable laterally vibrating piezoelectric MEMS resonators. *2015 Transducers - 2015 18th International Conference on Solid-State Sensors, Actuators and Microsystems, TRANSDUCERS 2015*, pp. 977–980. doi: 10.1109/TRANSDUCERS.2015.7181088.

Yang, J., Hamelin, B. & Ayazi, F. (2020). Investigating Elastic Anisotropy of 4H-SiC Using Ultra-High Q Bulk Acoustic Wave Resonators. *Journal of Microelectromechanical Systems*, 29(6), 1473–1482. doi: 10.1109/JMEMS.2020.3022765.

You, W., Yang, H., Sun, K., Pei, B. & Li, X. (2017, 1). Phase noise suppression effect at the turnover temperature in oven controlled mems oscillator. *2017 IEEE 30th International Conference on Micro Electro Mechanical Systems (MEMS)*, pp. 920–923. doi: 10.1109/MEMSYS.2017.7863559.

Yuan Xie, Sheng-Shian Li, Yu-Wei Lin, Zeying Ren & Nguyen, C.-C. (2008). 1.52-GHz micromechanical extensional wine-glass mode ring resonators. *IEEE Transactions on Ultrasonics, Ferroelectrics and Frequency Control*, 55(4), 890–907. doi: 10.1109/TUFFC.2008.725.

Zhang, Y. & Chen, D. (2013). *Multilayer Integrated Film Bulk Acoustic Resonators*. Berlin, Heidelberg: Springer Berlin Heidelberg. doi: 10.1007/978-3-642-31776-7.

Zhao, J., Yuan, Q., Sun, H., Yang, J. & Sun, L. (2018). Stability characterization of vacuum encapsulated MEMS resonators with Au–Sn solder bonding. *Microsystem Technologies*, 24(9), 3885–3892. doi: 10.1007/s00542-018-3888-0.

Zhu, H. & Lee, J. E. (2014, 5). Orientation dependence of nonlinearity and TCf in high-Q shear-modes of silicon MEMS resonators. *2014 IEEE International Frequency Control Symposium (FCS)*, (1), 1–4. doi: 10.1109/FCS.2014.6859981.